THE UNIVERSITY OF CHICAGO

QUANTITATIVE IMAGE ANALYSIS OF PIAL COLLATERALS IN ACUTE ISCHEMIC STROKE

A DISSERTATION SUBMITTED TO
THE FACULTY OF THE DIVISION OF THE BIOLOGICAL SCIENCES
AND THE PRITZKER SCHOOL OF MEDICINE
IN CANDIDACY FOR THE DEGREE OF
DOCTOR OF PHILOSOPHY

COMMITTEE ON MEDICAL PHYSICS

BY
CHRISTOPHER WILLIAM HADDAD

CHICAGO, ILLINOIS
AUGUST 2017

This thesis is dedicated to my family, and friends, lab-mates, and professors for their constant support and encouragement.

Oh, and this thesis is dedicated to Craig, Vivak, and Samer, too!

The Road goes ever on and on,

Down from the door where it began.

Now far ahead the Road has gone,

And I must follow, if I can,

Pursuing it with eager feet,

Until it joins some larger way

Where many paths and errands meet.

And whither then? I cannot say.

–J.R.R. Tolkien, *The Lord of the Rings*

TABLE OF CONTENTS

LIST OF FIGURES

LIST OF TABLES

ACKNOWLEDGMENTS

This dissertation would not have been possible without the contributions of many distinguished individuals. First and foremost, and I would like to express my deepest appreciation to my thesis advisor, Dr. Maryellen L. Giger, and my thesis mentor, Dr. Timothy J. Carroll, for their unparalleled patience, support, and encouragement during my graduate school career. I thank Dr. Giger for introducing me to the field and principles of quantitative image analysis in medicine and for her advice and supervision on my dissertation research. I thank Dr. Carroll for his mentorship in quantitative braining imaging and for his advice on managing a research project with multiple fronts. Dr. Carroll also taught me topics on MRI stroke imaging, which was very helpful in understanding the current state of quantitative imaging of stroke. I am especially grateful for their emphasis on the clinical utility of research results and for their mentorship in effectively communicating research to a wide audience. I am also grateful for their help in writing papers and making clear presentations.

I thank my dissertation committee members, Dr. Gregory A. Christoforidis, Dr. Timothy J. Carroll, and Dr. Xiaochuan Pan, for reviewing my dissertation and sharing their perspectives with me. I want to extend a special thanks to Dr. Christoforidis for collecting the x-ray angiographic database at the heart of this research and for his emphasis on a comprehensive clinical understanding of stroke imaging. I am grateful for Dr. Pan's quick and insightful review of my dissertation, which helped me ensure that ideas were conveyed in a contextual manner.

I am deeply indebted to many people in our program whose technical and administrative assistance was instrumental to this dissertation. The computer wizardry of Chun-Wai Chan, the SIRAF staff, Lorenzo Pesce, and the Beagle2 staff allowed for progress and creative approaches to be made on this research, for this I am deeply grateful. I want to extend my gratitude to the Dr. Samuel Armato, Jonathan Marino, Dr. Nicholas Gruszauskas, Dr. Michael Torno, Adam Starkey, Susan Fruth, and Roger Engelmann at the Human Imaging Research Office for the time and effort they put into anonymizing and providing the image

data for analysis. I am also thankful for the helpful suggestions from and engaging discussions with Roger and Dr. Kiego Kawaji. I would like to gratefully acknowledge Ruth Magaa, Julie Hlavaty, Gloria Frazier, and Joann Summers for their administrative and grant-writing support.

Deep appreciation goes out to the current and former members of Dr. Giger's lab for their help and supporting this endeavor. I want to give special thanks to Dr. Karen Drukker and Rebecca Gullett for their exceptional help, collaboration, and insightful suggestions after hearing my volleys of questions (and occasionally wacky) ideas. I would like to thank Dr. Hui Li, Li Lan, John Papioannou, Sasha Edwards, Dr. Will Wiess, Adam Sibley, Natasha Andropova, Kayla Mendel, and Dr. Andrew Jamieson for providing helpful comments and a welcoming environment in the lab. I want to thank Yong Ik Jeong, Dr. Grady Cantrell, and Kevin Carroll in Dr. Carroll's lab for their creative suggestions and helpful discussions.

I thank everyone at the University of Chicago and the Graduate Program in Medical Physics for their incredible efforts in providing an unparalleled environment to live, learn, and grow. I am honored to have worked with the many grateful and brilliant students and faculty at this institution. I have cherished my time here and it will be missed.

This dissertation would not have been possible without support from the following grants: the National Institutes of Health Training and Research Project Grants (5T32EB002103-25 and R01NS093908), the Paul C. Hodges Research Award for 2014, and the American Heart Association's Predoctoral Fellowship (AHA 15PRE24470173). The Scientific Image Reconstruction and Analysis Facility (SIRAF) and the Beagle2 supercomputer made this research possible, and I am incredibly grateful for their availability.

Last but certainly not least, I owe a loving thanks to my mother, father, and brother. My parents, who immigrated to the United States before they finished learning English, gave me unwavering support and encouragement as I pursued higher education and conducted this dissertation research. I owe my family eternal thanks and dedicate this research to them.

Thank you all.

ABSTRACT

Because of its human and economic cost, there is a need to reduce the disability resulting from a stroke. Though emergency reperfusion treatment can reduce disability, complications resulting from it, such as intracerebral hemorrhage, can be lethal. Many patients suffering from ischemic stroke develop varying degrees of pial-collateral arterial supply (PAS), which can affect patient response to reperfusion therapy and the risk of developing intracerebral hemorrhage. Observation of good PAS predicts a more favorable outcome (reduced disability) when performing reperfusion treatment.

Current methods for assessing pial collaterals use either (a) physically-installed pial windows, or (b) manual scoring of the extent of PAS on X-ray digital subtraction angiography (DSA) image series. Though pial windows provide microscopic visualization of pial collaterals, during a stroke, this method is clinically infeasible. Manual scoring off of X-ray DSA series is far more preferable because of X-ray DSA's availability during intervention, its resolution and scan time, and because manual scoring techniques can be reproducible and quantitative. However, these techniques' ultimate performances are coarse and dependent on viewer experience. Therefore, the objective of this dissertation is to investigate and develop a computational method to quantitatively assess PAS—imaged using X-ray DSA—in the setting of acute ischemic stroke. It is hypothesized that computerized and quantitative angiographic image analysis of pial arterial supply can be used to identify patients' suitability for reperfusion treatment.

Digitally-subtracted angiograms were retrospectively collected under an institutional review board-approved, protocol compliant with the Health Insurance Portability and Accountability Act of 1996 (HIPAA). Occlusion sites included the M1 segment of the Middle Cerebral Artery for 15 patients, the proximal M2 segment for 1 patient, and the Internal Carotid Artery for 8 patients. Eleven of the patients were imaged at 6 Frames/second, while the remainder were imaged under an X-ray dose-sparing protocol.

The research in this dissertation covers 3 major topics. First, a Fuzzy C-Means (FCM)

based approach for automatically segmenting PAS-affected vessels from capillary blush and background in X-ray DSA series during acute ischemic stroke was developed. With an area under the ROC curve of up to 0.89 across multiple frame-rates for the task of segmenting vessels from non-vessels, this method was shown to have robust performance and could identify vessels almost as well as an expert observer. Next, a quantitative method for extracting 10 features from kinetic contrast curves in X-ray DSA series and validating these features was developed. These features' abilities to distinguish between patients with favorable PAS from those with poorer PAS was evaluated. For the task of identifying patients with particularly poor PAS, many of these features had areas under the Receiver Operating Characteristic (ROC) curves of approximately 0.99, indicating a substantial capability for contra-indicating reperfusion treatment. Finally, a Fuzzy C-Means based approach for automatically segmenting arteries from non-arteries was developed and evaluated. Kinetic features were subsequently extracted from curves generated from segmented arteries and segmented parenchymal blush due to capillaries, and their performances in the task of distinguishing between patients with favorable PAS from those with poorer PAS was evaluated. The results suggested that FCM could segment arteries from non-arteries. Features extracted from pixel segmented arterial and capillary curves were comparable to features extracted without any segmentation; however, a mild improvement in performance for 2 features suggest that extracting features from arterial or capillary filling could provide real-time quantitative markers for a patient's condition during intervention.

The results support the hypothesis that during acute ischemic stroke, computerized and quantitative angiographic analysis of PAS can identify patients' suitability for reperfusion treatment. Therefore, this method can potentially serve as a fast "second-check" to an interventionalist's treatment decisions, leading to better outcomes and reduced disability. Limitations that must be overcome prior to clinical adoption include the small size of the database (24 cases total), the vascular overlap caused by projecting a 3D spatial volume to a 2D spatial image, and the uncontrolled environment of clinical exams. These limitations can

be addressed by including more cases, adapting the methods discussed in this dissertation to 4D (3D plus time) DSA series of acute ischemic stroke, and complementing the clinical studies presented in this thesis with simulation and preclinical canine studies, respectively.

This dissertation serves as the first step in achieving a fully computerized and quantitative means for personalizing patient management in intervention for acute ischemic stroke. Moreover, the techniques presented in this thesis may find application in quantifying imaging of other neurovascular disease.

CHAPTER 1

INTRODUCTION

Given its human and economic cost there is a need to reduce the disability that results from a stroke. Emergency reperfusion treatment can restore perfusion to the affected area and possibly reduce disability. However, complications resulting from emergency reperfusion treatment can be lethal. Therefore, there is an urgent and unmet clinical necessity to efficiently identify patients most likely to benefit from reperfusion treatment.

Many patients with ischemic stroke (i.e., stroke caused by a blockage) develop varying degrees of collateral arterial supply that can supply affected brain tissue. Pial collaterals have the potential to serve as a temporary blood supply (i.e., to reconstitute occluded arteries), allowing perfusion downstream of the blockage in the first hours after a stroke; this reconstitution can significantly benefit patients. Observation of good pial collateral arterial supply (PAS) using X-ray digital subtraction angiography (DSA) predicts more favorable outcome (reduced disability) when performing emergency reperfusion treatment.

Current methods assessing collaterals use either (a) physically-installed pial windows or (b) manual scoring pial collateral extent from X-ray DSA images. Although pial windows can provide microscopic visualization of pial collaterals, they are too invasive and, during a stroke, clinically infeasible. Scoring in the clinic is done manually using angiographic images and can be reproducible, but the ultimate performance is coarse and dependent on viewer experience.

A computerized and quantitative assessment of pial collateral supply during interventional imaging can allow for a more objective understanding of a patient's suitability for reperfusion treatment. Furthermore, such an assessment can be used to dynamically monitor the change in the brain tissue at risk, which may affect treatment decisions.

Therefore, the objective of this thesis is to investigate and develop a computational method to quantitatively assess pial collaterals—imaged using X-ray DSA—in the setting of acute ischemic stroke. It is hypothesized that computerized and quantitative angiographic

analysis of PAS can be used to identify patients' suitability for reperfusion treatment. Specifically, it is hypothesized that (1) with limited operator input, an efficient computerized segmentation technique for identifying large vessels from parenchymal blush due to capillaries is comparable to manual identification by a radiologist; (2) kinetic features extracted from the ischemic region in X-ray DSA can quantitate PAS; and (3) kinetic features extracted from specific vessel classes better quantitate PAS than features extracted from all vascular filling in the ischemic region.

1.1 Clinical Management of Acute Ischemic Stroke

1.1.1 Overview of Ischemic Stroke

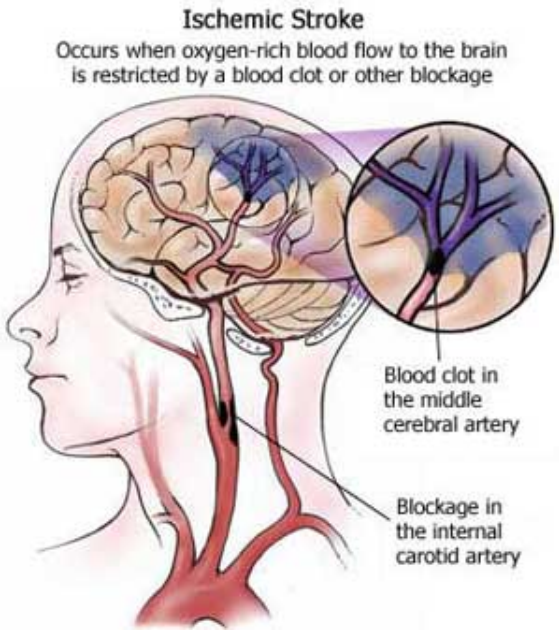

Figure 1.1: Common sites for treatable ischemic stroke include the internal carotid and middle cerebral arteries. Image courtesy of Christian Elliot [17].

In the USA, an estimated 700,000 people per year experience ischemic stroke. Ischemic stroke—which accounts for 87% of all strokes—occurs when the normal flow of blood in a major cerebral artery (Figures 1.2 and 1.1) is occluded (i.e., blocked) by blood clots, fat or cholesterol masses, or tissue fragments. The occluding object is referred to as an embolus

[31]. Common occlusions sites are the internal carotid and the middle cerebral arteries (Figure 1.1). When oxygen is significantly reduced, neurons, glial cells, and vessel epithelial cells begin to die, with the resulting dead tissue volume referred to as an infarct volume [16]. Cell death is often unavoidable a few hours hours after occlusion, but a significant portion of brain tissue is salvageable if treatment is administered with the first 3 hours [16, 21].

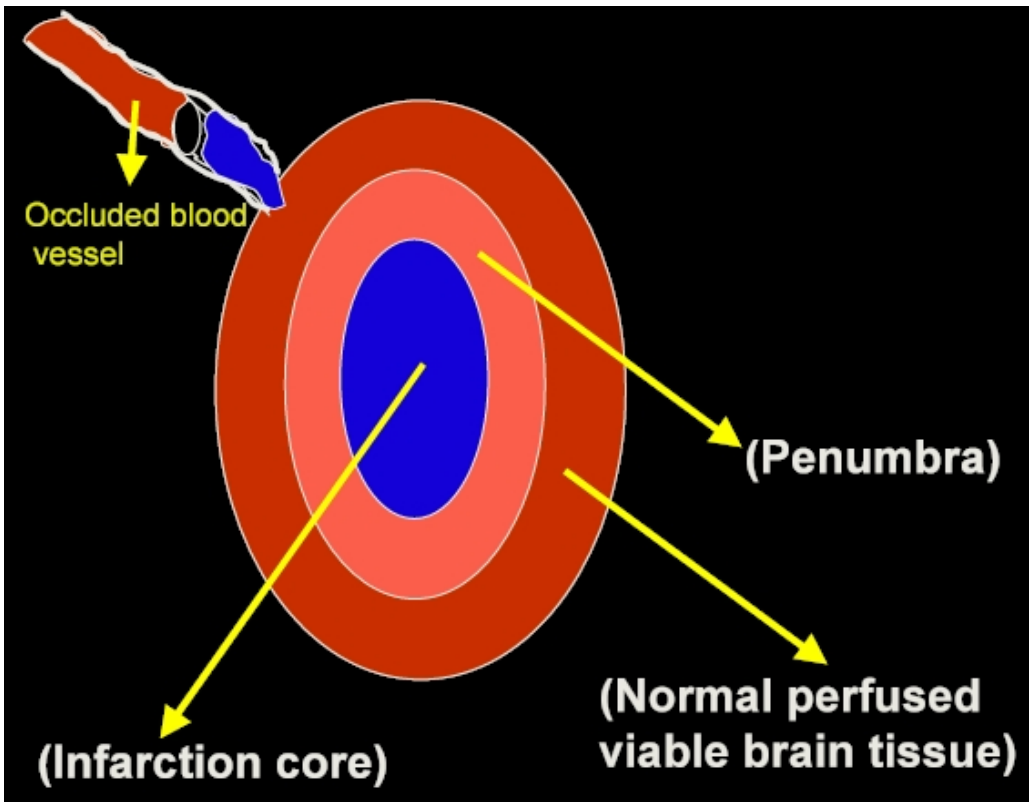

Figure 1.2: Distribution of underperfused and infarct (dead) tissue during an acute ischemic stroke. The infarct volume is closest to the occluded, or blocked, vessel, while underperfused but still-viable tissue surrounds the infarct in a penumbra [43].

1.1.2 Clinical Procedure and Treatment Options

After a patient suffering from stroke is brought to the emergency room and given an initial assessment, a non-contrast CT scan is performed to rule out intracranial hemorrhaging [47]. If no hemorrhaging is present, a CT angiography (CTA) scan is performed to locate the occlusion and map out the affected and surrounding arterial territories. If the embolus is a

blood clot and the time from onset is less than 4.5 hours, tissue plasmogen activase (tPA) may be given to dissolve it [21, 19].

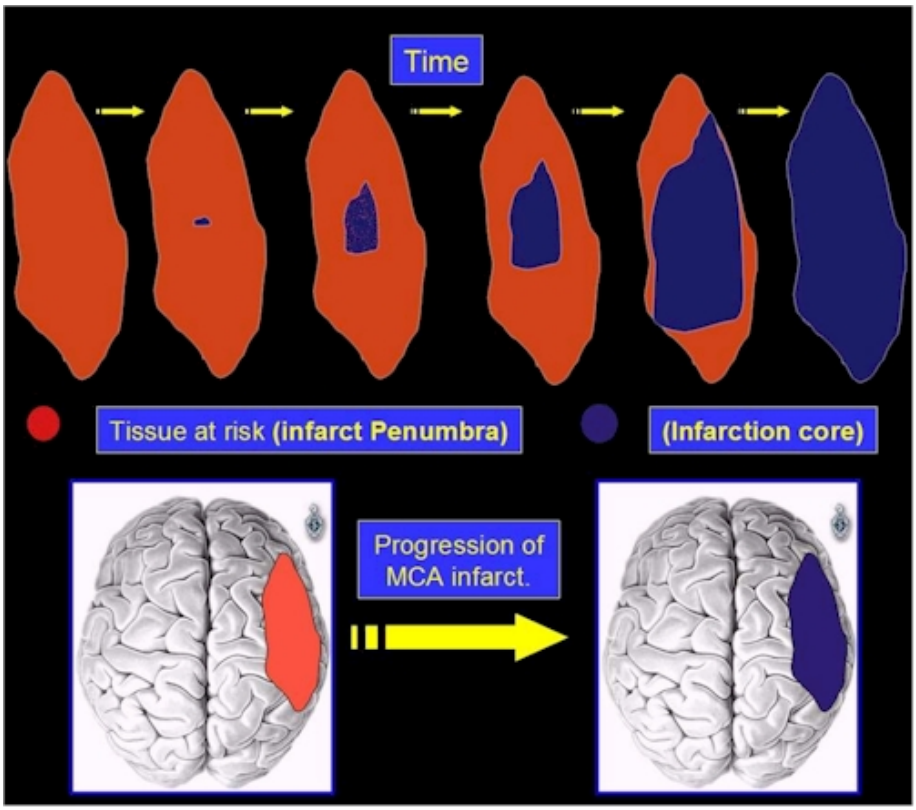

Figure 1.3: Progression of cell death in acute ischemic stroke for an MCA occlusion. As time passes, a greater portion the underperfused but still-viable tissue in the penumbra infarcts (i.e., dies off) until there is no salvageable tissue left [43].

If suitable and the time from onset is less than 8 hours [25, 19], the patient will then be moved to an interventional radiology suite for embolectomy [47]. Using planar X-ray digital subtraction angiography (DSA), catheters are guided from punctures to the femoral artery or a leg vein to the internal carotid artery. The neurointerventional radiologist will assess the flow of contrast in the timed angiographic image series and, if the patient can tolerate it, proceed with the reperfusion treatment.

Emergency reperfusion treatment using either clot-dissolving drugs (such as tPA) or embolectomy, (i.e, removal of the embolus) via an intra-vessel catheter restores perfusion and can reduce long-term disability in some patients [9], but must be administered within

4.5 hours . However, over 98% of stroke sufferers arrive outside the optimal treatment time window. Furthermore, these treatments can often have devastating side effects (intra-cerebral bleeding, reperfusion injury, complications and their associated disability), which reduce their risk/benefit profile [11, 9]. This underscores the urgent and unmet clinical necessity for efficient identification of patients most likely to benefit from reperfusion treatment.

1.1.3 Role of Pial Collaterals

Many patients with ischemic stroke develop varying degrees of arterial blood supply through collateral routes, such as pial arteries [48]. We refer to the filling of blood from these arteries as Pial Arterial Supply (PAS). During Middle Cerebral Artery Occlusion (MCAO), PAS serves as a temporary backroad supply, providing oxygen and nutrients to ischemic tissue [11, 9]. This reconstitution can significantly benefit patients. In a clinical studies and animal experiments, it was shown that observation of good pial collateralization using planar X-ray DSA predicts more favorable outcome in terms of reduced disability when treating a stroke and a reduced infarct volume [11, 9, 12]. Furthermore, the extent of collateralization plays an important role (independent of other factors including age, time to treatment, and recanalization) in determining the efficacy of reperfusion treatment and reducing the likelihood of inter-cerebral hemorrhage [11, 9, 5, 26, 29, 28, 2].

1.1.4 Available Clinical Imaging Modalities

Clinical imaging paradigms for assessing the presence of pial collaterals have been developed to improve outcome in ischemic stroke using CT Angiography (CTA), MR Angiography (MRA), or planar X-ray Digital Subtraction Angiography (DSA). CTA and MRA are used for initial assessment for collateral presence. Planar x-ray DSA is used during embolectomy to verify the existence and location of the embolus prior to removal. However, there is a trade-off between the value of identifying tissue at risk by MRI or CT and the time needed to acquire this information: setting for and performing the imaging exam will only increase

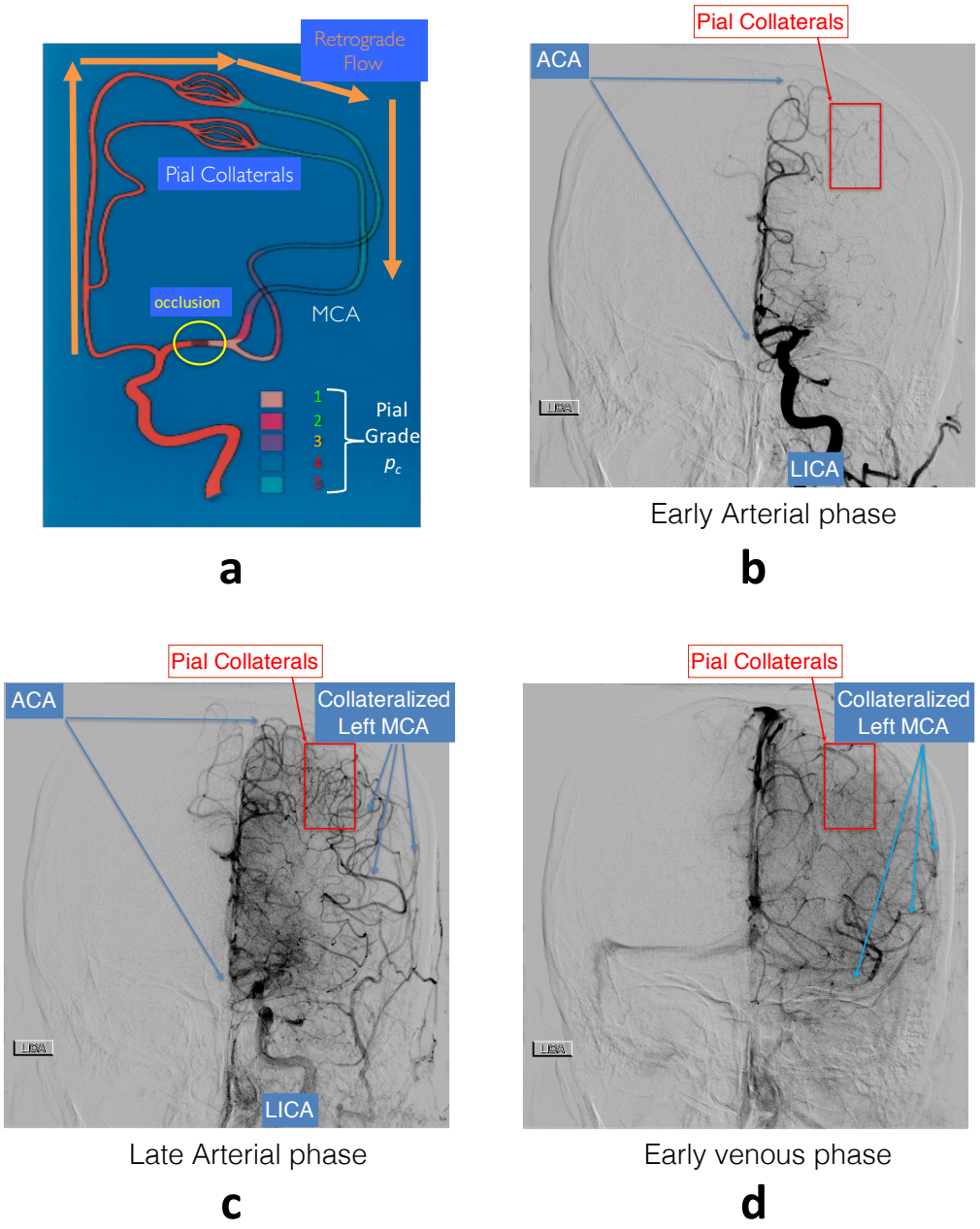

Figure 1.4: (a) Schematic representation of pial arterial supply (PAS) and the Christoforidis grading scale used to assess the degree of PAS [11]. (b-d) Pial arterial reconstitution of MCA territory at various stages as seen in X-ray DSA.

the between stroke onset and potential treatment. By contrast, planar X-ray DSA has superior resolution, an interventional setup for prompt treatment, and scan time to both CT Angiography and MR Angiography. Even though no parenchymal tissue is displayed on X-ray DSA images, measuring the extent of pial collateral reconstitution of an occluded territory may assess the ischemic penumbra. This makes planar X-ray DSA a useful choice if contrast-enhanced CT is unavailable or additional time must be saved. In a position statement, the American Heart Association stressed that additional imaging studies should not unduly delay treatment in appropriate patients [9]. Therefore, to assess the degree of PAS during stroke in an interventional setting, X-ray DSA would be the clear choice.

1.1.5 Current Clinical Assessment Methods and Their Limitations

Currently, methods for assessing pial collaterals include (a) a manual invasive experimental technique, (b) a technique for measuring cerebrovascular reactivity (CVR) on MRI, and (c) a subjective visual technique using x-ray DSA.

Manual invasive measurement of pial collateral size and number density is an approach that utilizes a Plexiglas window to replace a section of the calvarium enabling measurements of pial collateral number density and size. This pial window allows for the direct microscopic visualization of vessels on the brains surface [27, 24, 13], and thus, a direct evaluation of the potential magnitude of PAS. However, pial windows are only appropriate in animal studies.

Pial collaterals may also be assessed via measurements of the cerebrovascular reactivity (CVR). It has been shown that the measurement of CVR on blood oxygen level-dependent MRI (BOLD-MRI) can be correlated with the presence of pial collaterals as observed on x-ray DSA [23]. However, the time needed to prepare and perform BOLD-MRI ($>$ 10 minutes) would increase the time interval between symptom onset and potential treatment by a non-trivial amount.

Visually, radiologists may assess reconstitution of the occluded MCA by pial collaterals on X-ray DSA images. Currently, such assessments of the effect of pial collaterals use scoring

systems. In [11, 9, 12], reproducible manual scoring was based on the level of angiographically visible retrograde reconstitution of occluded MCA segments. This scoring system can be used to verify if the interventionist is to proceed with treatment. Transit time at affected areas in *Christoforidis et al, 2011* was assessed against the early venous phase [12]. Using the AMIRA software demonstrated a more quantitative determination of transit time from the contralateral, unoccluded MCA to the reconstituted M3/M4 junction of the occluded MCA. These scoring systems have been shown to reliably predict the outcome of treatment and were able to show that better pial collateral formation is associated with likelihood and severity of inter-cerebral hemorrhage following treatment. However, these scoring systems require a certain level of experience by the radiologist, whose assessment of pial collaterals is relatively coarse and subjective.

A second effect to consider is dispersion [36, 37]. As a contrast agent bolus moves through the vascular tree, it disperses through the individual branches. It has been suggested in Mouannes-Srour et al 2012 [37] that the scale (i.e., width) of a contrast-time curve measured on MRI may predict infarct volume. Dispersion of contrast agent concentration curves leads to underestimation of blood flow. This can cause tissue no longer in danger of infarct to be misdiagnosed, leading to mistreatment. In thrombolysis, this means an increased risk of hemorrhage.

1.1.6 Significance of Computerized and Automated Assessment

In addition to their particular limitations, the current methods of assessing pial collaterals are not objective. A quantitative and computerized assessment of PAS has the potential to reduce errors associated with inter-reader variability, leading to a more standardized and objective understanding of a patients condition.

Computerized and quantitative methods for assessing ischemic stroke on MRI have been developed [41]. Potreck et al. have proposed an automated scoring system based on T_{max} measurements from Dynamic Susceptibility Contrast Magnetic Resonance Imaging (DSC-

MRI) [41]. They present their methods as a complement to conventional penumbra imaging. McKinley et al. have developed a fully automated system that uses random forest classifiers and multimodal MRI to measure the penumbra volume and predict the final infarct volume [34]. They acknowledged, however, that collateral flow led a residual overestimation of the final infarct volume size. In addition, between the conclusion of an MRI exam and reperfusion treatment in the interventional suite, PAS may decrease because of failing pial collaterals; in that situation, an automatic assessment using MR images would present a patient as more suitable for reperfusion treatment than they actually are in the interventional suite, and, hence endanger the patients life.

A computational quantitative assessment of pial collaterals available to clinicians during interventional imaging is expected to allow for dynamic assessment of brain tissue at risk with the potential to detect subtle changes in the degree of PAS during the procedure; this may affect decision making during endovascular rescue. Using such an algorithm clinicians could potentially personalize treatments towards each patient, help manage risk, and more quickly deliver these treatments. As a result, this assessment can lead to a more efficient means to render effective treatment decisions, and an improved outcome for long-term recovery.

1.2 Objectives and Hypotheses

The goal of this research is to investigate and develop a computational method to quantitatively assess pial collaterals—imaged using X-ray DSA—in the setting of acute ischemic stroke. Therefore, for occlusion sits at Middle Cerebral Artery (MCA) or Internal Carotid Artery (ICA), we hypothesize that, during ischemic stroke, computerized and quantitative angiographic analysis of these collaterals can identify patients' suitability for reperfusion treatment.

1.3 Thesis Outline

The thesis is organized as follows. The first part, Chapter 2, is an overview of the clinical DSA database. The next three chapters deal with the development, validation, and analysis of the assessment method. Chapter 3 describes a Fuzzy C-Means-based approach that uses kinetic contrast curves to segment major vessels from parenchymal (capillary) uptake of contrast. Chapter 4 presents methods for extracting 10 features from kinetic contrast curves and validating those features' ability to discriminate between patients with favorable PAS from those with poorer PAS. Chapter 5 looks to merge the findings and development in Chapters 3 and 4 discusses Fuzzy C-Means-based segmentation of arteries from non-arteries, and the performance of features extracted from these arterial and capillary curves to automatically separate patients with favorable PAS from those with poorer PAS. The thesis closes with a summary of its contributions and discussion of limitations and future directions in Chapter 6.

CHAPTER 2

CLINICAL DATABASE AND ANGIOGRAPHIC ACQUISITION

		6 Fr/s	Mixed Frame-rate
Number of Cases		11	13
Number of Cases with Repeat Acquisitions		6	1
General Anesthesia		11	10
Iohexol Injection technique		hand	
tPA Treatment		3	7
Mechanical thrombolectomy		7	8
Occlusion Type	**MCA**	8	8
	ICA	3	5
Time from Onset (hours)		2-8	
Number of Females		12	

Table 2.1: Summary of Clinical Angiographic Database

Digitally subtracted angiograms were collected retrospectively under an institutional review board-approved, HIPAA-compliant protocol. Angiograms were acquired using Philips Alura Xper interventional suites from 24 patients undergoing treatment for stroke at the University of Chicago Medical Center. Occlusion sites included the M1 segment of the Middle Cerebral Artery for 15 patients, the proximal M2 segment for 1 patient, and the Internal Carotid Artery terminus for 8 patients. There were a total of 12 females and 12 males with and age range y_{low} to y_{high}.[Dr. Christoforidis must provide the patient and procedure details because I do not have patient reports for Cases 21-39]. General anesthesia was given to 21 patients to reduce motion during imaging; the remaining 3 were determined to have minimal motion.

All angiograms were acquired at 75.0-103.6 kVp and exposures of 11-49 mAs. Image matrix size was 1024 $\times$ 1024 pixels with pixel resolution ranging from 0.1526 mm $\times$ 0.1526 mm to 0.215 mm $\times$ 0.215 mm. Iohexol was injected by hand to provide contrast in the vessels. Angiograms from 11 cases were acquired at 6 Frames/second; the remainder were acquired

under an X-ray dose-sparing protocol that would start imaging at 3 Frames/second, switching to imaging at 1 Frames/second 4–4.33 seconds into the acquisition, and then switching to imaging at 2 Frames/second 12–12.33 seconds into the acquisition.

In Table 2.2, cases were organized by into datasets according to frame-rate, and whether or not they had repeated acquisitions. Of the 24 cases, 7 had at least two repeated angiograms.

Case Number	Datasets						Pial Grade Truth p_c
	A (6 Fr/s)	**A_3 (3 Fr/s)**	**A_M (Mixed Frame-Rate)**	**B (Mixed Frame-Rate)**	**A_r (6 Fr/s repeated acquisitions)**	**B_r (Mixed Frame-Rate repeated acquisitions)**	
1	✓	✓	✓				1
2	✓	✓	✓				5
3	✓	✓	✓		✓		3
4	✓	✓	✓		✓		1
5	✓	✓	✓				2
6	✓	✓	✓		✓		4
7	✓	✓	✓		✓		2
8	✓	✓	✓				2
9	✓	✓	✓				3
10	✓	✓	✓		✓		3
11	✓	✓	✓		✓		2
12				✓			2
13				✓			2
14				✓			2
15				✓			2
16				✓			3
17				✓			2
18				✓			3
19				✓			1
20				✓		✓	2
21				✓			2
22				✓			3
23				✓			4
24				✓			4
Number of Cases	11	11	11	13	6	1	- -

Table 2.2: Organization of Case Angiograms. Note that cases may be organized by frame-rate and whether or not they have repeated DSA acquisitions. Note that additional datasets were generated by downsampling Dataset A to 3 Fr/s (i.e. Dataset A_3) and according to the mixed frame-rate protocol (i.e., Dataset A_M).

CHAPTER 3

FUZZY C-MEANS SEGMENTATION OF VESSELS IN ANGIOGRAPHIC IMAGES OF STROKE

3.1 Background

The central hypothesis of this thesis is that computerized and accurate quantification of the extent of pial arterial supply (PAS) to the ischemic region can alter the assessment of a stroke patient's candidacy for reperfusion treatment. Because of the role reconstituted MCA branches (i.e., MCA branches affected by PAS) play in patient assessment, the ability to segment major vessels in angiographic images of stroke will be critical to developing a computerized assessment method of PAS. In current interventional settings, major vessel branches are identified visually on X-ray DSA series by interventional radiologists. However, this involves acquiring image series than run into the late venous phase and identifying multiple major vessel branches across almost all image frames, which is very time-consuming. Therefore, manual delineation of vessel boundaries in an interventional setting is highly impractical.

Methods have been developed to segment vessel in DSA images. *Sang et. al.* proposed two methods (one for developed for computational speed and the other for accuracy) that involve adaptive thresholding based on *a priori* knowledge of the vessels' diameters [45]. In *Franchi et. al*, a shape recognition algorithm that utilizes anisotropic Gaussian filters, angular mapping, and thresholding schemes is proposed that had fewer false positives when compared to the more accurate method described in *Sang et. al* [18]. However, these methods require involved user input, making them unsuitable in an interventional setting. Furthermore, they focus on segmenting vessels within a given frame in a DSA series and assume a background with little contrast. During acute ischemic stroke, MCA branches affected by PAS may fill over the course of many frames and the presence of contrast blush due to capillaries violates the assumption of a background with little contrast. Therefore, a

technique that is robust over multiple frames in a DSA series and properly handles capillary filling will be able to better segment vessels in the ischemic territory.

Fuzzy C-Means (FCM) clustering is an unsupervised pattern-recognition method that has been shown to reliably segment breast lesions in dynamic contrast-enhanced (DCE) MRI. In *Chen et. al, 2006*,[7], the post-contrast DCE-MRI images are divided by the pre-contrast image to remove unenhanced tissue prior to application of the FCM algorithm [7]. This processing of DCE-MRI series can be treated as an analog to X-ray DSA. Therefore, in this study, the FCM clustering is adapted to segmenting reconstituted MCA vessels in X-ray DSA series. The performance is evaluated by comparing vessel pixel classification against radiologists' manual designations on retrospectively-acquired DSA series.

3.2 Methods

3.2.1 Review of Fuzzy C-Means Clustering

Fuzzy C-Means (FCM) clustering is an unsupervised learning method for pattern recognition. Its goal is to find the fuzzy partition of data set X comprising N data vectors ($X = \{\mathbf{x}_i, i = 1, 2, ..., N | \mathbf{x}_i \in R^m\}$) into N_c clusters, or classes. The data vector $\mathbf{x}_i$ is an m-dimensional feature vector. The class means are represented by a $N_c \times m$ matrix, V. Each column of V corresponds to the mean feature vector of a class. The partition, or set of class membership scores, for X is given by the $N_c \times N$ matrix U. Each element of matrix U, u_{ki}, represents the membership score of the i^{th} data point to the k^{th} class and always falls in the range [0, 1]. The FCM implementation presented here follows the implementation detailed in *Chen et al, 2006* for solving for U and V [7], except that this implementation is done on with a GTX Titan graphical processing unit (nVidia Corporation, USA) on a cluster node with 256 GB of memory.

3.2.2 Vessel Segmentation via FCM clustering

An angiogram may be represented as $D(x, y, t)$, where x and y are spatial pixel coordinates and t is time. For each pixel i, the contrast over time is shown via a time density curve $D_i(t)$, where t is time. These curves are input directly into the FCM algorithm via the contrast contrast values at each time index.

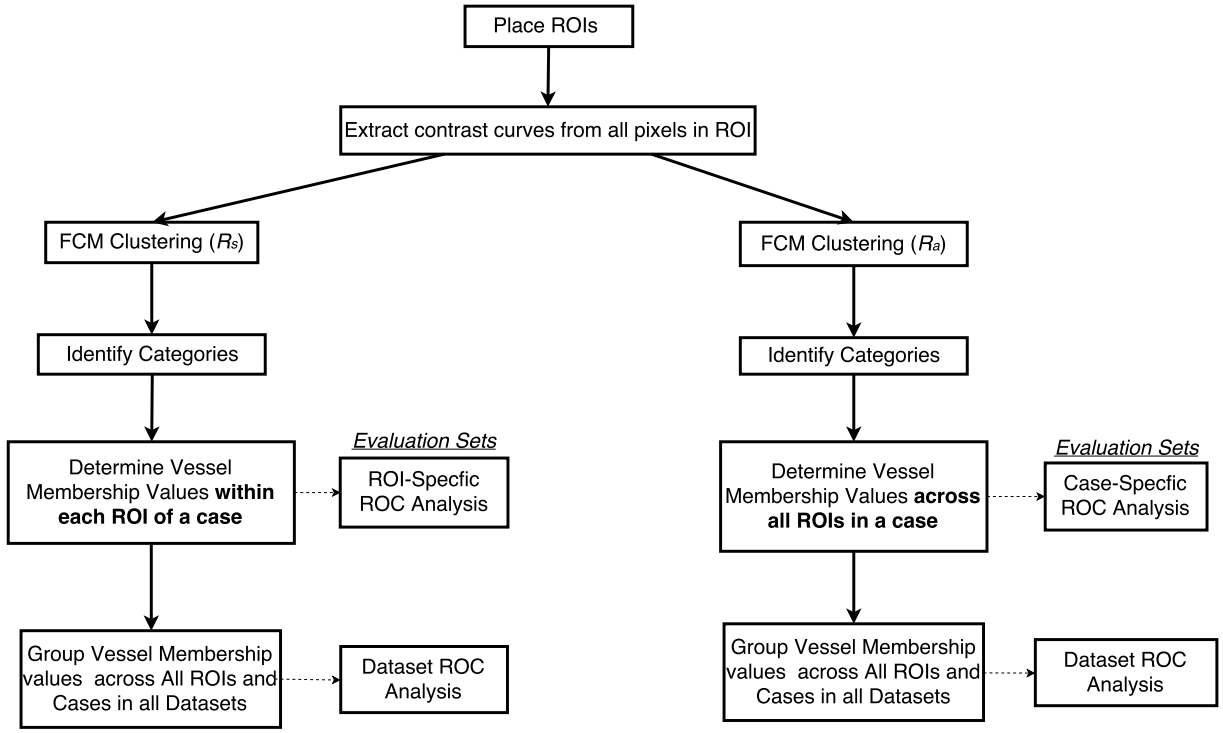

Figure 3.1: Flow-chart for the proposed FCM vessel segmentation algorithm with ROC analysis conducted in the task of distinguishing between pixels that are vessels and pixels that are not vessels.

Using the pixel curves as inputs (i.e., $\mathbf{x}_i = \mathbf{D}_i$, where $\mathbf{D}_i$ is the vector notation of curve data in $D_i(t)$), FCM clustering then is used to separate pixels into 2 or 3 classes ($N_c \in \{2\ 3\}$). When $N_c = 2$, the two classes are (1) background and parenchymal blush due to capillaries and (2) large blood vessels, or major vessels; when $N_c = 3$, the 3 classes are (1) background, (2) parenchymal blush due to capillaries, and (3) major vessels. The steps of the segmenting algorithm are outlined in Figure 3.1. The output of FCM are matrices $U = [\,U_1\ U_2\ U_3\,]^T$ of size $3 \times N$ and $V = [\,V_1\ V_2\ V_3\,]^T$ of size $3 \times M$. Each row of U is the transpose of the

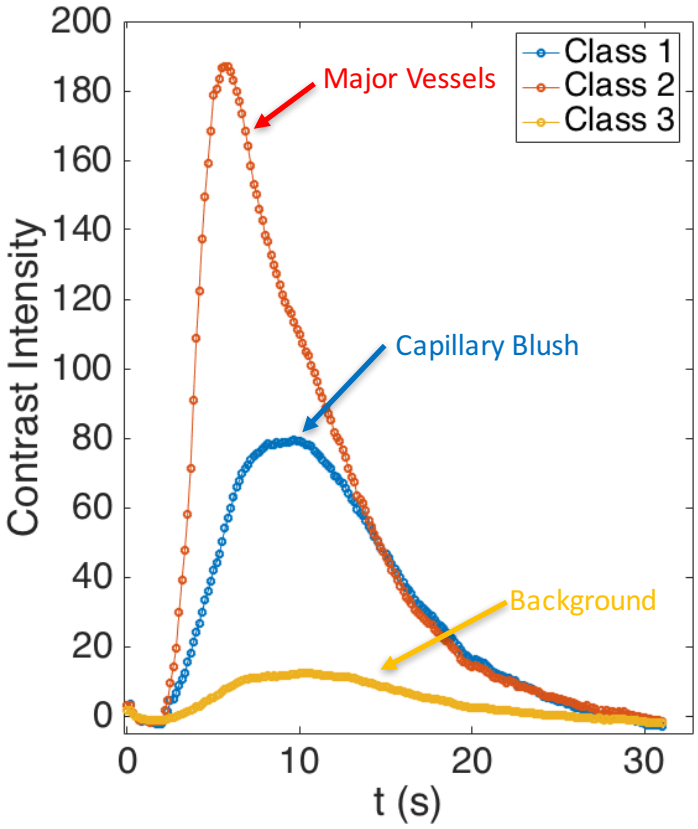

Figure 3.2: Mean curves in V for input curves from ROI $r = 3$ in Fig 3.5a. The curves are identified with their respective classes (text with arrows) using the peak heights.

column vector representation of a class's membership map. Similarly, each row vector of V represents the mean density curve of one of the 3 classes (Fig 3.2), with the cluster ordering in V matching that in U. The rows of U and V are then sorted according to peak heights of the mean density curves in V.

If $N_c = 3$, the mean curve with the highest peak is identified as belonging to the major vessel class; the mean curve with the median peak is identified as belonging to the capillary blush class; and the curve with the lowest peak is identified as belonging to the background class. Similarly, if $N_c = 2$, the mean curve with the higher peak is identified as belonging to the major vessel class and the mean curve with the lower peak is identified as belonging to the capillary blush class. The ordering for the curve-peak-sorted rows in U, and hence the class membership maps, is the same as for the mean peak–height-sorted contrast curves in V. Sample sorted mean density curves of the major vessel, capillary blush, and background

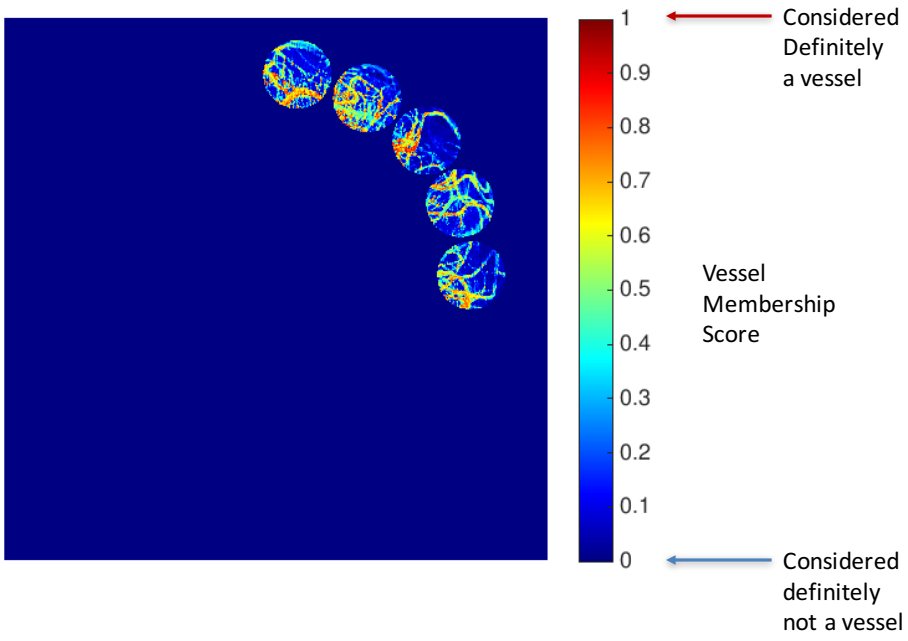

Figure 3.3: Class membership map for major vessels in Fig. 3.5a.

classes are shown in Figure 3.2 and a corresponding vessel membership map is shown in Figure 3.3.

As a contrast bolus travels through the vasculature tree, it undergoes dispersion and delayed arrival, which broadens a pixel's density curve and lowers its height (Figure 3.4). We will exploit this property to identify pial collateral arteries. However, in the occluded MCA territory, this delay-and-dispersion effect causes a pixel density curve in capillary blush-only region (anterograde filling) to appear similar to a pixel density curve in a major MCA branch (retrograde filling) that is further downstream (i.e., within later-filling segments of the MCA territory) in the direction of flow. To reduce the resulting misidentification of anterograde capillary blush as retrograde filling of an arterial branch, circular regions of interest (ROIs) are specified in the direction of flow. For MCA occlusions (Figure 3.5a), 5 circular regions of interest (ROIs) with indices $r = 1$–5 were specified in the direction of retrograde filling. Four ROIs contained the MCA branches, while one ROI was chosen in the anterior cerebral artery (ACA) branches (normal, anterograde filling) for reference. This process was repeated

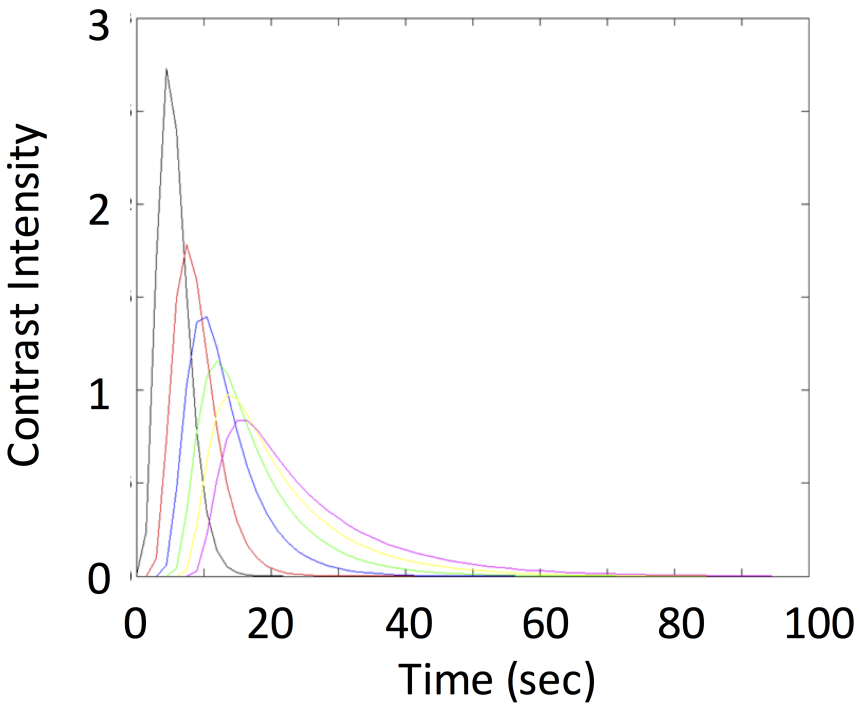

Figure 3.4: Effect of delay and dispersion (courtesy of *Mouannes-Srour* [36]). Given a reference contrast curve (black), delay-and-dispersion will cause a successive lowering of the peak height and broadening of contrast curves (colored curves) as the contrast bolus travels through the vasculature.

for Internal Carotid Artery (ICA) occlusions; however, because the occlusion-side ACA is affected by an ICA occlusion, an additional circular ROI was chosen in the normal-side ACA territory (Figure 3.5b) to act as the reference for normal perfusion. Circular shapes were chosen for these ROIs because they would not intrude into the edge of the calvaria as easily as conventional rectangular shapes. These ROIs were automatically placed at regular angular intervals in each image in the angiogram with the ability for adjustment by the operator. FCM clustering was then conducted on a) each individual circular ROI to reduce the influence of dispersion (input data protocol R_s, see Figure 3.6 and Table 3.1), and b) inputting all ROIs of a given case together (input data protocol R_A, see Figure 3.7 and Table 3.1). The latter was done to better understand the effect of delay-and-dispersion on segmentation performance.

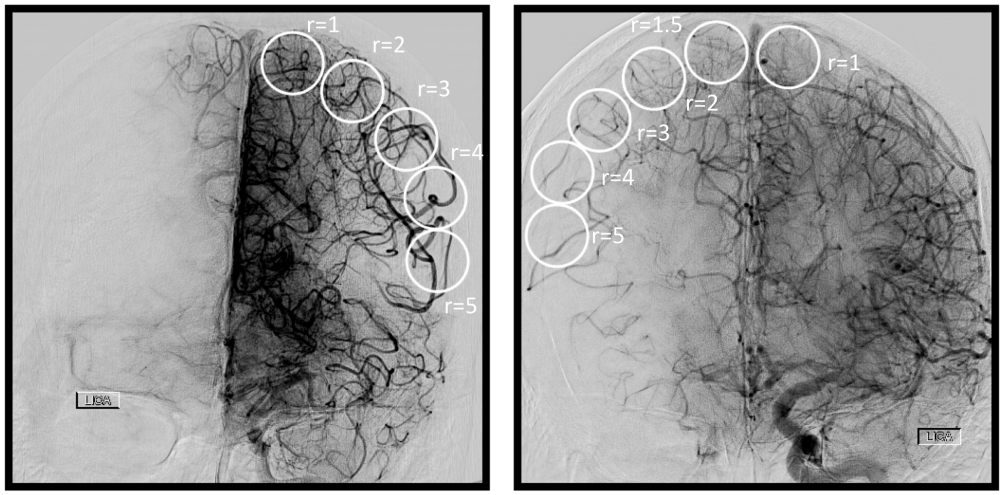

Figure 3.5: Circle placement in angiographic images. (a) For MCA occlusions, 5 circles are placed in the ipsilateral ACA ($r = 1$) and reconstituted MCA branches ($r = 2$–5). (b) For ICA occlusions, 6 circles are placed on the normal-side ACA ($r = 1$), occlusion-side ACA ($r = 1.5$), and reconstituted MCA branches ($r = 2$–5).

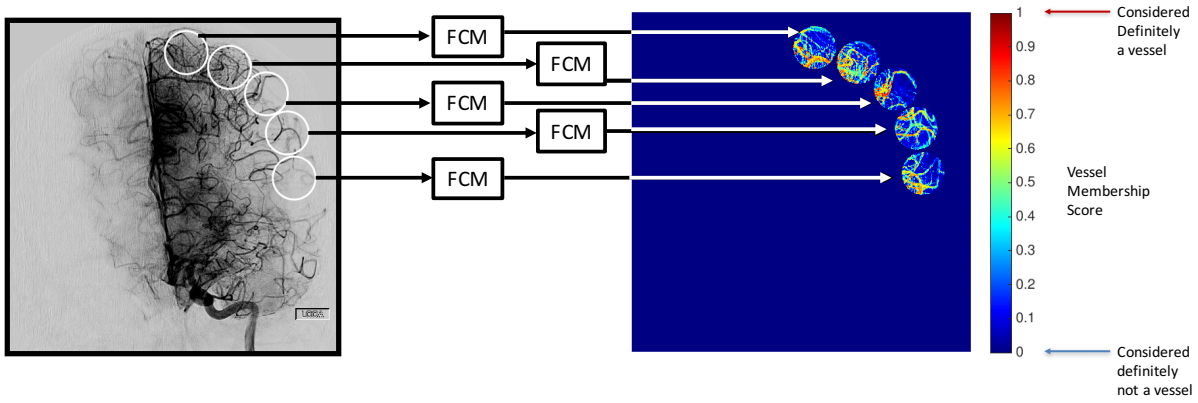

Figure 3.6: Implementing FCM using R_s (each ROI as a separate input to FCM; see Table 3.1)

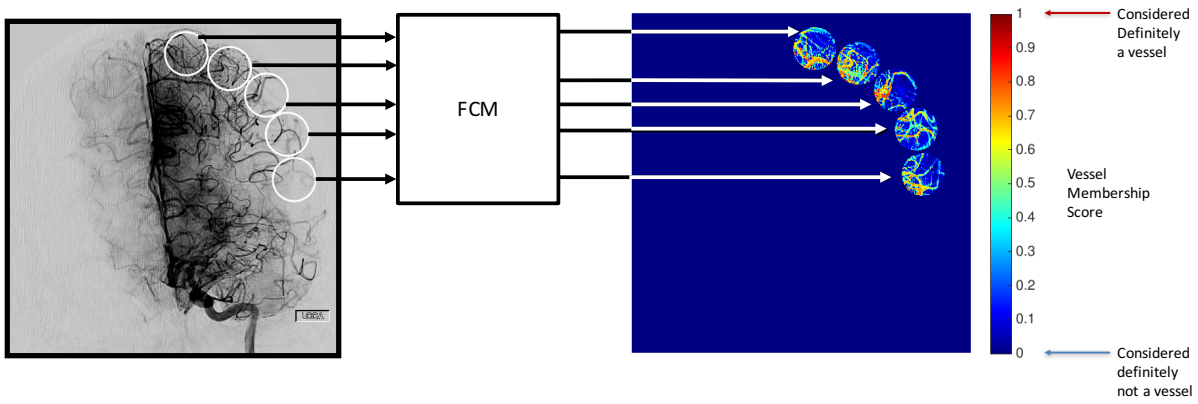

Figure 3.7: Implementing FCM using R_A (All ROIs as input to FCM; see Table 3.1)

3.2.3 Evaluation

The FCM algorithm was evaluated via direct comparison with manually-determined ground truth (major vessels versus capillary blush/background). In this study, pixels in the ROIs for cases in Dataset A and B (see Table 2.2) were labelled by a board-certified neuroradiologist (G.A.C.) as belonging to one of the following categories: (1) major vessels or (2) capillaries or background.

For each category, 25–40 pixels were labelled in each ROI (i.e., ROI-specific truth), although this number may be lower if the prevalence for a category in a particular ROI is small. Using this truth, the task of separating major vessels from capillary blush was assessed using Receiver Operating Characteristic (ROC) analysis. ROC curves are generated by using the pixels' major vessel membership scores as the decision variable. The truth is used within each ROI, across all ROIs in an angiogram to generate case-specific ROC curves, across all cases of a given frame-rate is grouped to generate frame-rate-based curves, and finally across all cases to yield an ROC curve for the entire dataset. Because class membership values always fall in the range [0 1], this pooling scheme allows performance to be summarized for each ROI, each case, each frame-rate subset, and/or the entire dataset. ROC curves for the figures presented here were fitted using the proper binormal ROC model [40] software package and the non-parametric Wilcoxon area under the ROC curve AUC was used as the

Input Data Protocol	FCM Inputs	Evaluation Databases
R_s	Single ROI	1) All pixels across all cases 2) All pixels across cases of a specific frame-rate
R_A	Angiogram (All 5-6 ROIs)	1) All pixels across all cases 2) All pixels across cases of a specific frame-rate

Table 3.1: Organization of input data for FCM segmentation of major vessels from parenchymal blush due to capillaries

performance metric for this task.

The two sided 95% confidence interval for reported AUC values were empirically estimated using bootstrapping (1000 iterations). Performance was compared for different choices for the number of clusters in FCM (N_c), different input data protocols to FCM (Table 3.1), and for different frame-rates (Databases A, A_3, and A_M, see Table 2.2) were determined by evaluating the differences in AUC (ΔAUC). Any difference in AUC values was assessed through bootstrapping (3000 iterations) and two-sided 95% confidence intervals were calculated for superiority testing. One-sided 90% confidence intervals were calculated for non-inferiority assessment when superiority testing was inconclusive. Non-inferiority was reached if the lower limit of the confidence interval was larger than -0.02 [20].

3.3 Results

The FCM segmentation technique was implemented in Matlab (Mathworks, Inc.) and was run on an nVidia GTX Titan graphical processing unit. When the input data spanned 1 ROI per administration of FCM, segmentation for all ROIs in a case takes approximately 15 seconds; when the input data spans all ROIs in a case, the segmentation takes approximately 30 seconds.

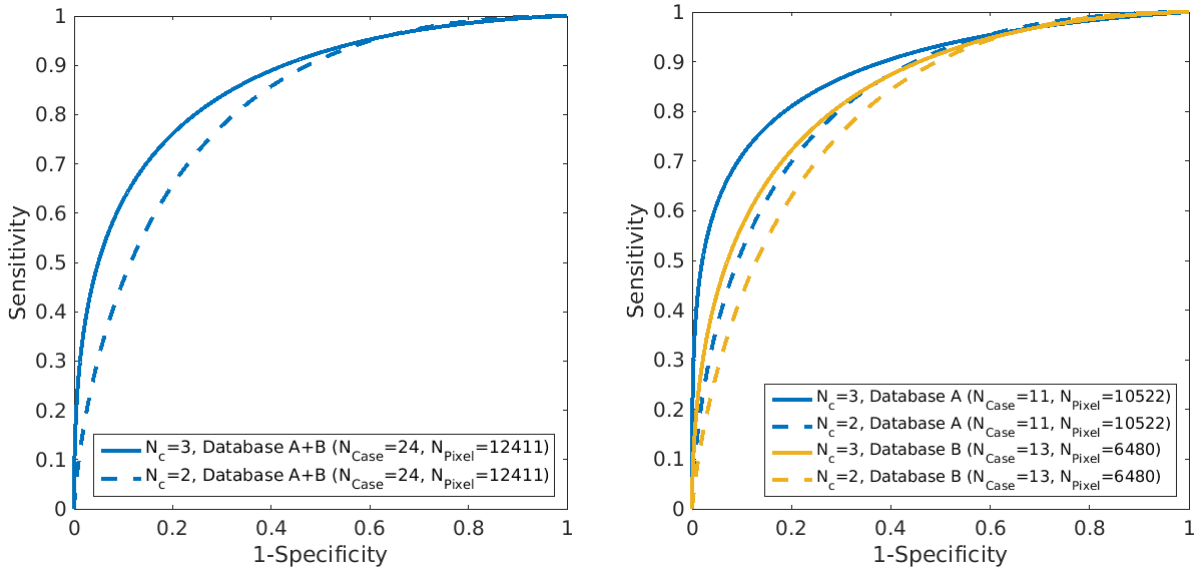

(a) (b)

Figure 3.8: Fitted binormal ROC curves for the performance in separating vessels from parenchymal blush and background for number of categories $N_c = 3$ and $N_c = 2$. The ROC curves span Dataset A+B (see Table 2.2) in (a) and Datasets A and B (datasets for 6 Fr/s and Mixed frame-rate acquisitions, respectively) in (b). The truth for Dataset A+B includes all pixels across all cases; the truth ROCs from Datasets A and B include all pixels across all cases acquired at 6 Fr/s and the Mixed Frame-rate protocol, respectively. The input protocol to FCM was R_s.

$\mathbf{N_c}$	**AUC**	**95% Confidence Interval of ΔAUC**	**p-Value** ($\alpha = \mathbf{0.025}$)
3	0.86 [0.87; 0.89]	$[0.03; 0.05]$	< 0.001
2	0.82 [0.81; 0.83]		

Table 3.2: Database ROC statistics for different numbers of input classes N_c and input protocol R_s (Fig. 3.8a), with 95% confidence intervals in brackets (using Dataset A+B, 24 cases). Because the 95% confidence interval is above zero, there is a statistically significant improvement in separating major vessels from parenchymal blush and background when $N_c = 3$. The significance level α is adjusted using a Holm correction.

Frame-Rate	N_c	AUC	95% Confidence Interval of ΔAUC	p-Value ($\alpha = 0.025$)
6 (Dataset A)	3	0.89 [0.88; 0.89]	[0.03; 0.06]	< 0.001
	2	0.84 [0.83, 0.85]		
Mixed (Dataset B)	3	0.85 [0.84; 0.86]	[0.02; 0.05]	< 0.001
	2	0.81 [0.80; 0.82]		

Table 3.3: Frame-rate ROC statistics for different numbers of input classes N_c and input protocol R_s (Fig. 3.8b), with 95% confidence intervals in parentheses. The superior performance is consistent across both frame-rates for $N_c = 3$. The significance level α is adjusted using a Holm correction.

3.3.1 Effect of Number of FCM Categories N_c

In this section, the input data protocol for each administration of FCM was R_s, i.e., each input was restricted to 1 ROI (Table 3.1). Segmentation of major vessels from parenchymal blush and background using FCM with $N_c = 3$ has favorable performance over using FCM with $N_c = 2$ (Figure 3.8a and Table 3.2). In particular, the bootstrapped 95% confidence intervals for ΔAUC are above zero, indicating a clear separation between $N_c = 3$ and $N_c = 2$. This improved performance for $N_c = 3$ holds between acquired frame-rates as well (Figure 3.8b and Table 3.3). In Figure 3.9, it can be seen that, except for 2 cases, the mean ROI AUC for $N_c = 3$ are consistently higher than for $N_c = 2$.

3.3.2 Comparing Input Data Protocols

In this section, the number of clusters was $N_c = 3$. The input data protocol R_s leads to improved performance across the database compared with using the input data protocol R_A (Table 3.1) for FCM (Figure 3.10a and Table 3.4). The bootstrapped 95% confidence interval of ΔAUC is above zero (Table 3.4), indicating superior performance when FCM is administered on each ROI separately. This effect also holds when assessing performance separately for the DSA series acquired at the different frame-rates (Table 3.5). In Figure 3.11, using R_s for FCM yields mean ROI AUCs that are higher for 75% of cases than the case

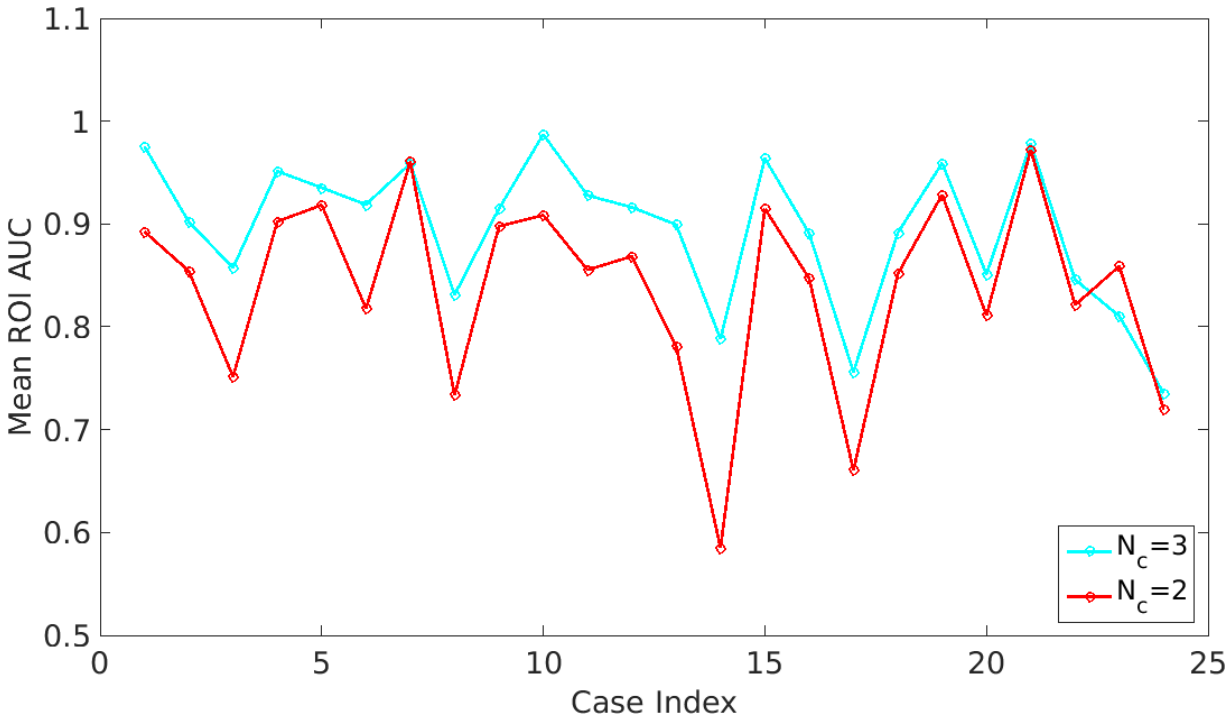

Figure 3.9: Mean ROI *AUC* for each case (Dataset A+B; see Table 2.2). For 22 of the 24 cases, $N_c = 3$ yielded better performance than $N_c = 2$ in the task of identifying major vessels from parenchymal blush and background.

AUCs obtained when using R_A into FCM. For the remaining 25% of cases, the differences between the case AUCs and the mean ROI AUCs are ≤ 0.07.

Input Data Protocol	**AUC**	**95% Confidence Interval of ΔAUC**	**p-Value** ($\alpha = 0.05$)
R_s (Individual ROIs)	0.86 [0.86; 0.87]	[0.05; 0.07]	< 0.001
R_a (All ROIs in Case)	0.80 [0.79; 0.81]		

Table 3.4: Database ROC statistics for different input protocols and $N_c = 3$ (Fig. 3.10a), with 95% confidence intervals in brackets (Database A+B, see Table 2.2). Because the 95% confidence interval is above zero, there is a statistically significant improvement in separating major vessels from parenchymal blush and background when using R_s into FCM.

3.3.3 Effect of Frame-Rate

When using $N_c = 3$ using data protocol R_s for FCM, the 6 Fr/s (Database A) and 3 Fr/s (Database A_3) subsets yielded nearly identical ROC curves and $AUC = .89$ for all frame-

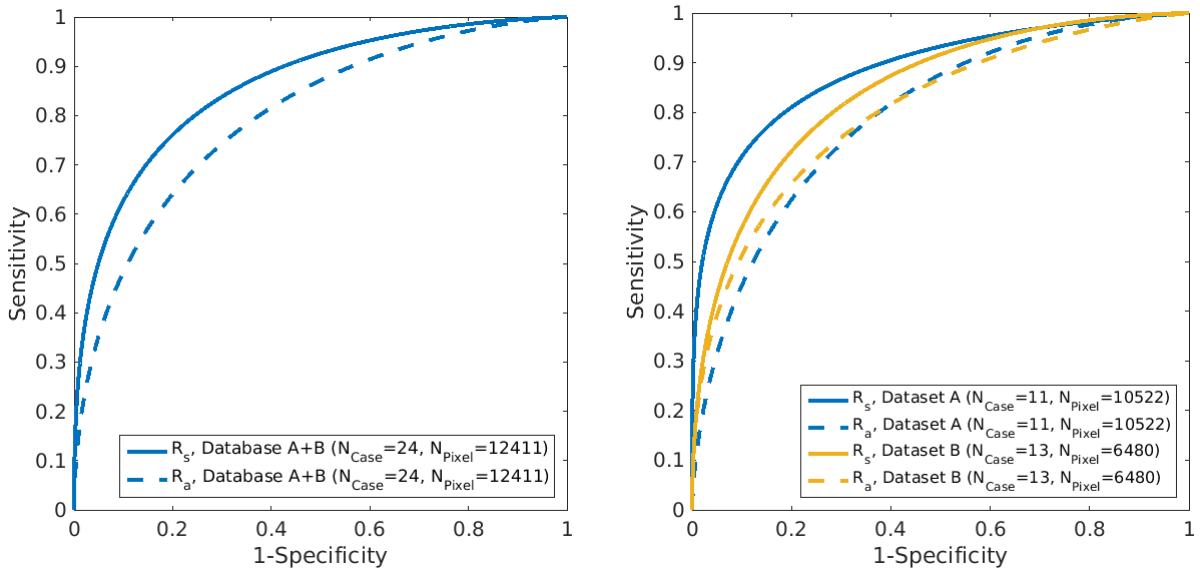

Figure 3.10: Fitted binormal ROC curves for the performance in separating vessels from parenchymal blush and background for using $N_c = 3$ and different input data protocols (see Table 3.1). The ROC curves span Dataset A+B (see Table 2.2) in (a) and Datasets A and B (datasets for 6 Fr/s and Mixed frame-rate acquisitions, respectively) in (b). The truth for Dataset A+B includes all pixels across all cases; the truth ROCs from Datasets A and B include all pixels across all cases acquired at 6 Fr/s and the Mixed Frame-rate protocol, respectively.

Frame-Rate	**Input Data Protocol**	**AUC**	**95% Confidence Interval of ΔAUC**	**P-Val ($\alpha = 0.025$)**
6 (Dataset A)	R_s: Individual ROIs R_a: All ROIs in Case	0.89 [0.88; 0.89] 0.80 [0.78; 0.81]	[0.07; 0.11]	< 0.001
Mixed (Dataset B)	R_s: Individual ROIs R_a: All ROIs in Case	0.85 [0.84; 0.86] 0.81 [0.79; 0.82]	[0.02; 0.06]	< 0.001

Table 3.5: ROC statistics for $N_c = 3$ and different input protocols separating cases imaged at different frame-rates (Fig. 3.8b). The superior performance is consistent across both frame-rates when using R_s into FCM. The significance level α is adjusted using a Holm correction.

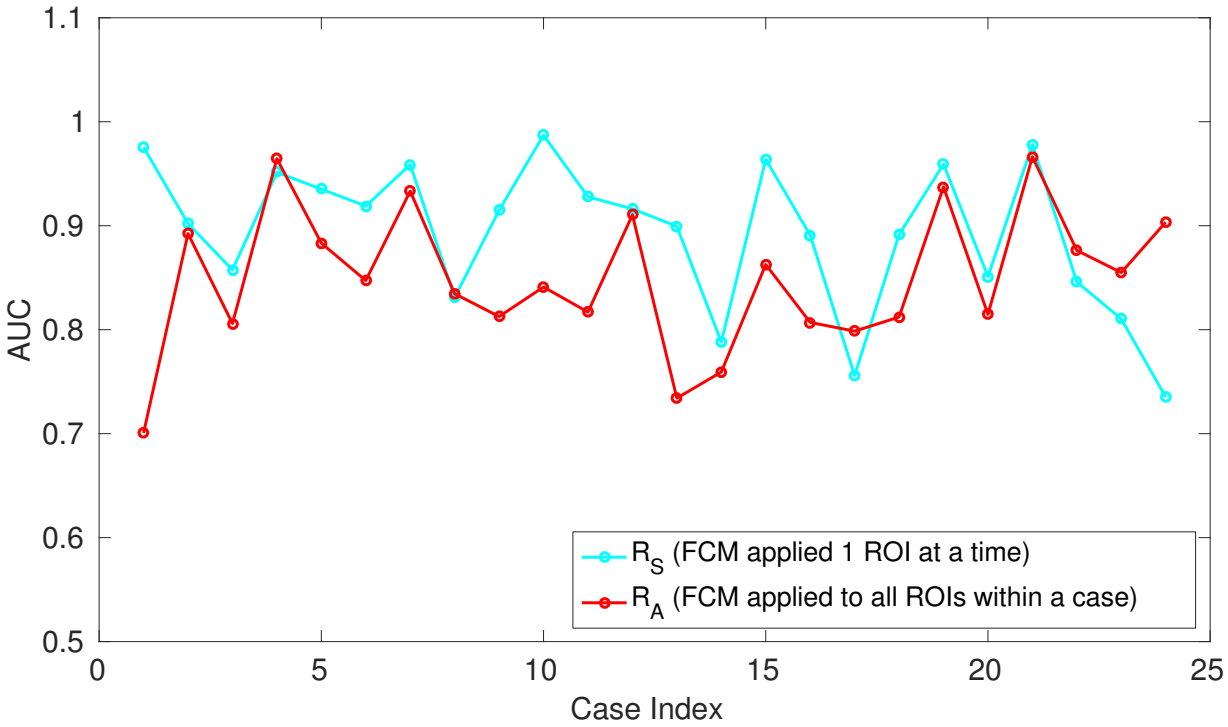

Figure 3.11: Within-case performance in the task of identifying major vessels from parenchymal blush and background for each choice of input range to FCM, with 95% confidence intervals in parentheses (Dataset A+B; see Table 2.2). The curve for using R_s into FCM (cyan) represents the Mean ROI AUC and curve for using R_A into FCM (red) represents the case-wide AUC.

rates examined in this study (Figure 3.12 and Table 3.6), indicating that this method is insensitive to frame-rates that may be used in the clinic (Table 2.2). Similarly, the 95% confidence interval for AUC for the angiograms taken under the mixed frame-rate protocol is only slightly wider than the uniform frame-rate angiograms. This robustness is further reflected in the bootstrapped pairwise difference between the subgroup's AUC shown in Table 3.7. The difference in performance for the different frame-rates failed to reach statistical significance (Table 3.7, two-sided 95% confidence interval for ΔAUC). Moreover, non-superiority testing (Table 3.7, one-sided 90% confidence interval for ΔAUC) demonstrated that the performances for different frame-rates could be considered equivalent. The P-values were all compared to a Holm-corrected significance level of $\alpha = .025$.

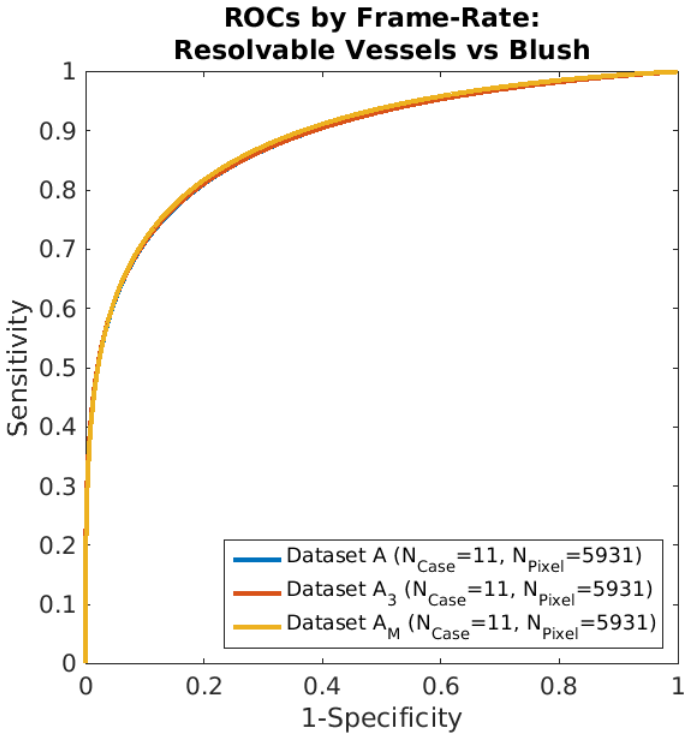

Figure 3.12: Fitted binormal ROC curves for each frame-rate dataset ($N_c = 3$ and input protocol R_s). The curves for 6 Fr/s and 3 Fr/s are so close that they overlap in the figure. Area under the curve AUC is reported in the legend with the 95% confidence intervals in parentheses.

Frame-rate Dataset	N	AUC
Dataset A	11	0.89 [0.88; 0.89]
Dataset A_3	11	0.89 [0.88; 0.89]
Dataset A_M	11	0.89 [0.88; 0.90]

Table 3.6: *AUC*'s with 95% confidence intervals in brackets for Datasets A, A_3,A_M (see Figure 3.12 and Table 2.2). FCM was conducted using $N_c = 3$ classes and input protocol R_s.

Frame-rate Dataset Comparison	ΔAUC	Two-sided 95% Confidence Interval	One-sided 90% Confidence Interval
A vs A_3	-4.0×10^{-4}	[-0.012; 0.012] (0.53)	[-0.008; 1]
A vs A_M	-5.0×10^{-3}	[-0.017; 0.007] (0.79)	[-0.013; 1]

Table 3.7: Pairwise bootstrapped difference in *AUC* between frame-rates with confidence intervals (brackets) and P-values (parentheses). FCM was conducted using $N_c = 3$ classes and input protocol R_s. The significance level is adjusted to $\alpha = 0.025$ using a Holm correction.

3.4 Discussion

By clustering input data into 3 classes and inputting each ROI separately into FCM, FCM clustering has substantial performance in segmenting major vessels from capillary blush and background. There are two major reasons for this level of performance. The first and most direct reason is that because of vascular dispersion, there is a higher concentration of contrast in the vessels about the peak time, leading to higher and wider contrast curves. A second and very important reason is that bone and cranial parenchyma are automatically subtracted out in the cases' angiographic images. This removes the corresponding constant offsets in each pixel's contrast curve, allowing only curve values representative of contrast concentration to be input to FCM.

The improved performance for $N_c = 3$ demonstrates that capillary filling, though reduced relative to the major vessels, is considerable enough to separate it from the noisy background. For the 2 cases in Figure 3.11 in which $N_c = 2$ had improved performance over $N_c = 3$, there were ROIs with either relatively little capillary blush or few background pixel; for these ROIs, $N_c = 2$ would be a more appropriate choice. Cluster analysis using silhouetting criteria may

be a useful means for determining the best choice of N_c for a given ROI.

Using input protocol R_s (i.e., individual ROIs) for FCM produces favorable overall performance for the database and within datasets separated by frame-rates; however, in Figure 3.11, using protocol R_a produced better performance for 6 cases. One case was an ICA occlusion in which contrast was visible only in the 2 ACA ROIs ($r = 1$ and $r = 1.5$ in Figure 3.5). In these ROIs, the degree of delay-and-dispersion is reduced relative to occluded MCA branches. As a result, the input data schemes are roughly comparable.

Closer examination of the remaining 5 cases revealed that mild motion artifacts (i.e., more visible bone and parenchyma) are present as contrast moves through the ischemic region. The artifacts are present across the affected ROIs and obscure the effect of delay-and-dispersion on the capillaries, making administration of FCM on separate ROIs less useful than administering FCM on all ROIs per case. Indeed, absent such artifacts, the consequences of delay-and-dispersion can be clearly seen (Fig. 3.13). Therefore, reducing motion would allow for better segmentation of major vessels from capillary blush and from background.

An important finding in these results is that a high frame-rate is not necessary to satisfactorily segment major vessels. This indicates that the difference between major vessels and parenchymal filling due to capillaries is captured in low frequency components in the pixel contrast curves.

3.4.1 Limitations

The database consisted of DSA series from only 24 cases. Therefore, results in this chapter need to be confirmed with a larger database. Because FCM's success depends on the absence of bone and parenchymal tissue in the pixel curve data, severe motion artifacts will result in poor segmentation. To reduce motion during imaging, general anesthesia was given to 21 patients. Temporarily restraining patients during imaging or the development of robust motion-correction techniques may also help reduce motion artifacts. In each ROI, ground

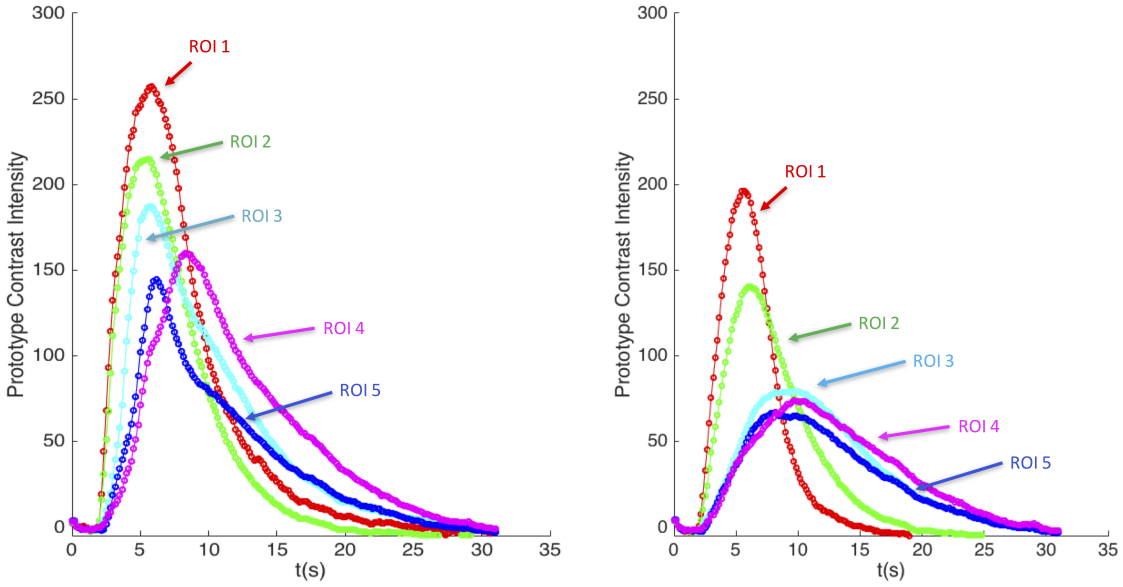

(a) Major Vessel Class (b) Capillary Class

Figure 3.13: Mean curves for each ROI (input separately to FCM) for the case in Fig 3.5a. Note the effect of delay-and-dispersion in the direction of flow for both major vessels and capillaries (parenchymal blush).

truth was specified using only 25-40 pixels per class. Outlining major vessels in each ROI would allow for more complete representation of the ground truth. Using this approach, interoperator variability can be measured and an overlap ratio or Dice coefficient may be used as the performance metric.

3.5 Conclusion

In conclusion, an FCM-based method for automatically segmenting collateralized MCA vessels in acute ischemic stroke using digitally-subtracted X-ray angiograms was developed. This method shows promise in identifying vessel pixels and has robust performance at all clinical angiographic frame-rates examined in this study.

CHAPTER 4

KINETIC FEATURES AND THEIR RELATIONSHIP WITH PIAL COLLATERAL PRESENCE

4.1 Background

There are numerous techniques for assessing collateral formation and reconstitution of the ischemic territory [35]. *Christoforidis et al* have developed a 5-point grading scale which rates PAS based on the extent of retrograde filling of the Middle Cerebral Artery territory on X-ray angiographic images [11]. Other scales developed by *Qureshi et al* and *Bang et al* assess the occlusion site, rapidity, and the extent of PAS [42, 4, 35]. However, such techniques frequently suffer from operator bias and are not quantitative [35]. A computerized and quantitative assessment of PAS during X-ray angiographic imaging would be more objective and has the potential to be more reliable than a human operator, which can better inform treatment decisions.

As early as 1985, *Heintzen et. al.* explored extracting kinetic features, or parameters, to quantify angiographic images [22]. More recently, in canine experiments, the arterial arrival time from normal to occluded vasculature, the relative cerebral blood volume, relative transit time, and relative cerebral blood flow as measured on X-ray DSA were suggestive of infarct volume as measure on MRI [12, 8, 10]. Furthermore, *Strother et. al.* has shown that presentation of peak-contrast parameters from X-ray DSA images improved clinicians' treatment planning and evaluation of various disease states, including stroke [46].

Because of the known beneficial effect that collateral supply has on the penumbra and infarct volumes, in this chapter we developed and evaluated a quantitative approach for assessing collateral supply based on the filling of iodinated contrast in X-ray Digital Subtraction Angiography (DSA). Since the degree of collateral filling affects the size of the ischemic penumbra and the endovascular treatment decisions, we hypothesize that our new method allows for monitoring of intra-interventional changes in collateral supply. Another

aim of this study was to investigate the performance of kinetic features—extracted from the ischemic region in X-ray DSA—in characterizing PAS, and hence their performance to determining patients' candidacy for treatment.

4.2 Methods

4.2.1 Reference Standard: Grading of Pial Supply

The grading system developed in *Christoforidis et al., 2005* to classify the degree of PAS to the occluded Middle Cerebral Artery (MCA) branches was used as the gold standard truth [11]. With this grading, the 14 patients with grades $p_c = 1$–2 were considered to have good PAS (Table 4.1), thus making excellent candidates for reperfusion treatment, while the 10 patients with pial grades $p_c = 3$–5 were considered to have poor PAS and thus less suitable for reperfusion treatment. Because some patients with $p_c = 3$ were potentially treatable, this pial grade represents a borderline state between patients with $p_c = 1$–2 (considered to reflect patently good PAS and for which treatment is recommended) and patients with $p_c = 4$–5 (considered to reflect patently poor PAS and for which treatment should be avoided).

PAS Grade p_c	**Number** of **Cases**
1	3
2	11
3	6
4	3
5	1

Table 4.1: Distribution of PAS Grade p_c within the clinical database

4.2.2 Semi-automated Delineation of Kinetic Regions of Interest

For DSA angiograms with M1 or proximal M2 occlusions (Figure 4.1a), 5 circular regions of interest (ROIs) with indices $r = 1$–5 were specified in the direction of retrograde flow. Four ROIs contained the occluded MCA branches while one ROI was chosen in the (normally

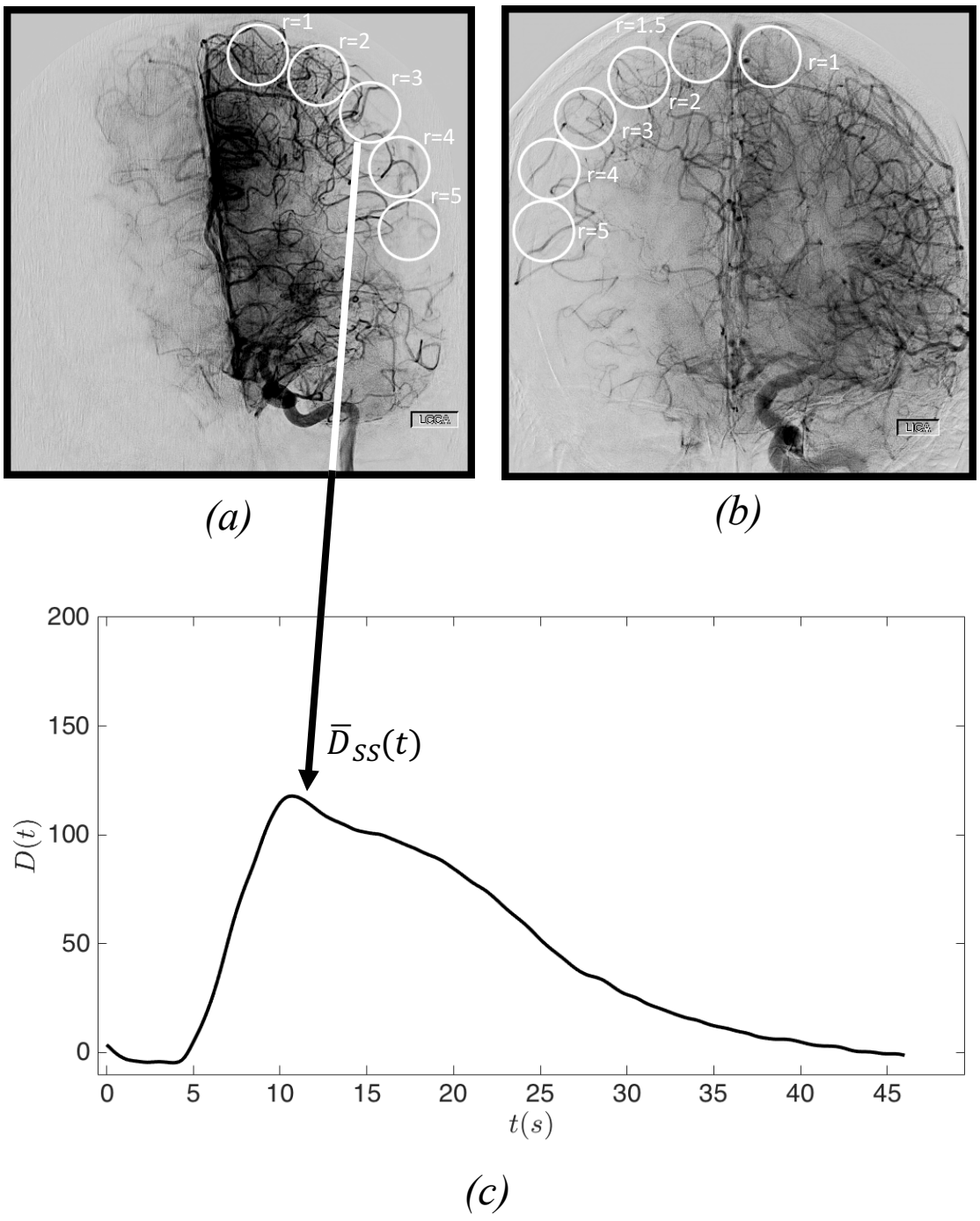

Figure 4.1: ROIs were placed and identified by indices r =1–5 as shown for MCA occlusions (a) and ICA occlusions (b). Because the second ROI in (b) represents a borderline status between normal and ischemic filling, it was given an index of $r = 1.5$. A mean contrast curve $\overline{D}_r(t)$ extracted from each ROI was fitted with a smoothing spline (c) to produce the curve $\overline{D}_{r,SS}(t)$.

perfused) distal anterior cerebral artery (ACA) branches for reference. This process was repeated for Internal Carotid Artery (ICA) occlusions; however, because the distal ACA branches on the occluded side experience reduced flow, an additional circular ROI was chosen in the contralateral distal ACA territory (Figure 4.1b) to act as the reference for normal perfusion. Circular shapes were chosen for these ROIs because they did not intrude into the edge of the calvaria as easily as rectangular shapes. These ROIs were automatically placed at regular angular intervals in each image in the angiogram with the ability for adjustment by the operator.

In this study, an angiogram was represented as a 3D array (2D projection plus time) of contrast curves, $D(x, y, t)$, where x and y correspond to spatial pixel coordinates and t is time in seconds. For each ROI within each angiographic case, a mean contrast-time curve $\overline{D}(t)$ was calculated by averaging all the pixel values within an ROI at each image frame (i.e., time):

$$\overline{D}_r(t) = \frac{\sum_{x,y \text{ in ROI}} D(x, y, t)}{N}, \tag{4.1}$$

where N is the number of pixels in within an ROI. Thus, over the database of 24 cases (16 cases with 5 ROIs, 8 cases with 6 ROIs), 128 contrast-time curves were calculated. To reduce the influence of residual noise and small-scale oscillatory motion due to breathing and pulsation, each $\overline{D}(t)$ was fitted with a cubic smoothing spline (smoothing parameter p=0.98981) [44, 15].The smoothing spline (SS) was sampled at a rate of 1/6 Hz, so that all smoothed curves $\overline{D}_{r,SS}(t)$ had the same sampling rate of 6 Fr/s (i.e., 6 Frames/second).

4.2.3 Computer-Extracted Kinetic Features

A set of computer-calculated kinetic features (Table 4.2) was extracted from each smoothed contrast curve, $\overline{D}_{r,SS}(t)$, to assess the degree of PAS. The features extracted were either purely timing-based or had a combination of both timing and density-based components (the latter category will be referred to as density-based features). Features based on timing

alone were the arterial arrival time AAT, time to peak TTP, and estimated mean transit time $eMTT$. Density-based features include the area under the contrast curve A_D, contrast curve peak PK, area under the uptake phase of the contrast curve $A_{D,Uptke}$, uptake rate UR, contrast value at uptake $\overline{D}_{r,SS}(t_{UR})$, slope to peak S, and ABF. These features are described as follows:

Feature	**Description**	**Has Density Component?**
A_D	Total area for $\overline{D}_{r,SS}(t)$	Yes
PK	Peak height of $\overline{D}_{r,SS}(t)$	Yes
$A_{D,Uptke}$	Area for arterial phase of $\overline{D}_{r,SS}(t)$	Yes
AAT	Time of contrast arrival from ICA	No
TTP	Time-to-peak	No
$eMTT$	Estimated mean transit time	No
UR	Uptake Rate=Maximum Slope of $\overline{D}_{r,SS}(t)$	Yes
$\overline{D}_{r,SS}(t_{UR})$	Density at time of UR	Yes
S	Mean slope of arterial phase of $\overline{D}_{r,SS}(t)$	Yes
ABF	Ratio of $A_{D,Uptke}$ to $eMTT$	Yes

Table 4.2: Descriptions of the extracted kinetic features.

Area under the Contrast Curve A_D

The total volume of contrast in an ROI, a surrogate for blood supply, was inferred by calculating the area under the smoothed curve $\overline{D}_{r,SS}(t)$:

$$A_D \approx \frac{t_{end}}{2m_{end}} \sum_{m=0}^{m_{end}} \overline{D}_{r,SS}(l\Delta t), \tag{4.2}$$

where $\Delta t = 1/6$ Hz is the sampling interval, $m = 01, 2, 3, ..., m_{end}$ is the frame index for time $t = m\Delta t$, and t_{end} is the time for the last frame in the angiogram (see Figure 4.2).

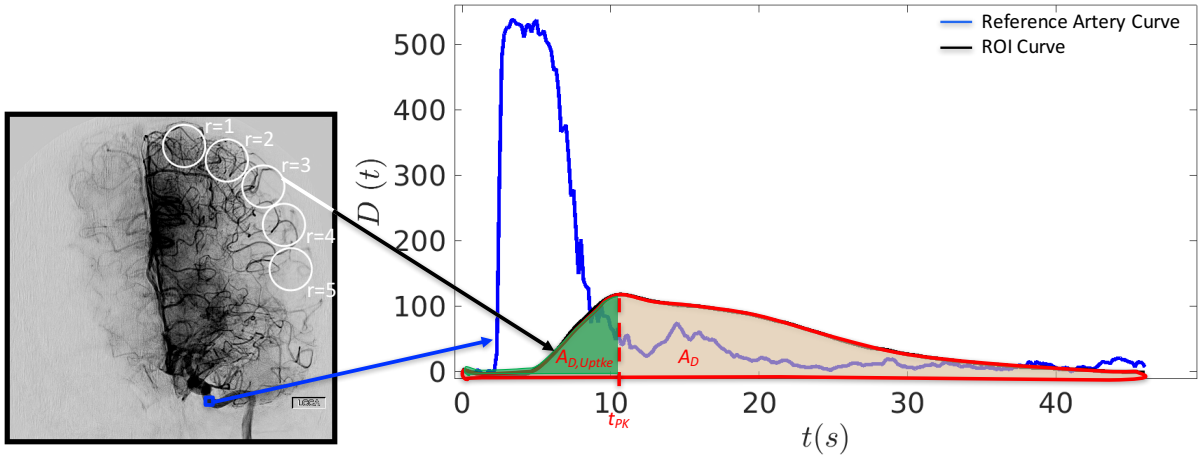

Figure 4.2: Volumetric Features A_D (red outline) and $A_{D,Uptke}$.

Contrast Curve Peak PK

The contrast peak PK was calculated as the maximum value of $\overline{D}_{r,SS}(t)$, and the corresponding time of PK is given by t_{PK} (Figure 4.3). For ROI index $r > 1$, if $\frac{PK_r}{PK_1} < 0.08$, then PK_r was considered to represent noise rather than peak contrast.

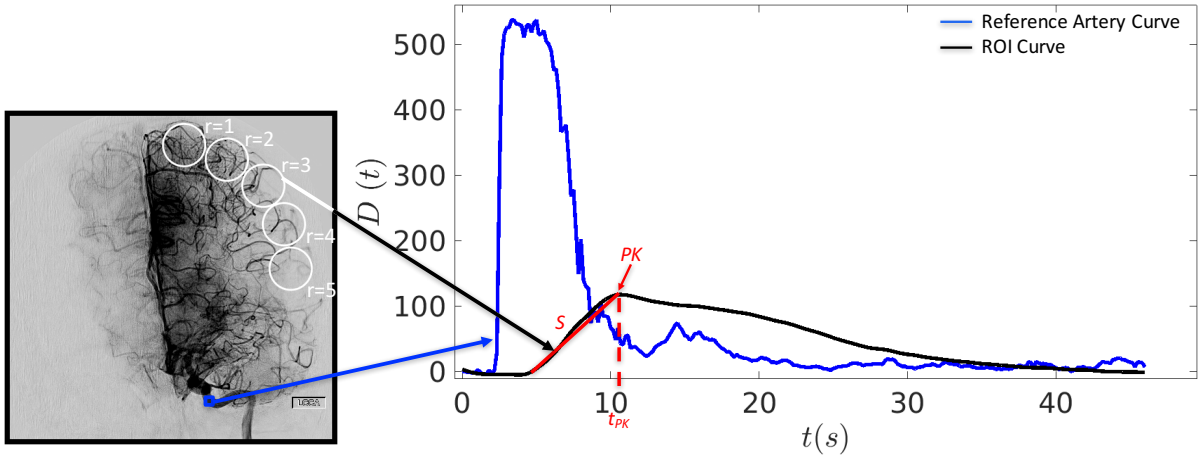

Figure 4.3: Pressure Features S and PK

Area under the Uptake Phase of the Contrast Curve $A_{D,Uptke}$

Since it may better reflect the total volume of contrast and local transit time in an ROI, the area under $\overline{D}_{r,SS}(t)$ from the start of acquisition to t_{PK}, denoted here as $A_{D,Uptke}$ (shown

in green in 4.2), is

$$A_{D,Uptke} \approx \frac{t_{PK}}{2l_{PK}} \sum_{l=0}^{l_{PK}} \overline{D}_{r,SS}(l\Delta t). \tag{4.3}$$

Arterial Arrival Time AAT

The contrast arrival time, t_{CA}, for a given ROI is defined as the time interval between the start of the angiogram and the moment that contrast arrives in that ROI. This quantity is extracted using the technique described in *Carroll et al.* [6]. It must be noted, however, that contrast was not always injected into the bloodstream at the same time during the scan. To eliminate this complication, Arterial Arrival Time (AAT) is defined as the temporal distance between the specific ROI and the Internal Carotid Artery (ICA) (Figure 4.4):

$$AAT = t_{CA} - t_{CA,ICA}. \tag{4.4}$$

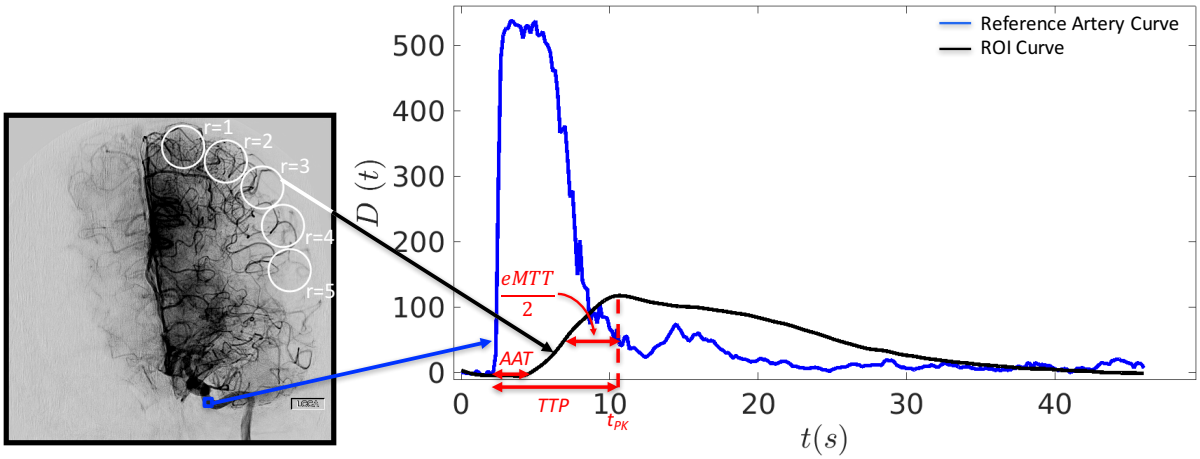

Figure 4.4: Timing Features AAT, TTP, and $eMTT$.

Time to Peak TTP

An ROI's time to peak TTP was defined as the temporal difference between its peak time t_{PK} and the contrast arrival time of the ICA $t_{CA,ICA}$(Figure 4.4).

Estimate Mean Transit Time $eMTT$

The estimated mean transit time ($eMTT$) in an ROI is determined as follows:

$$eMTT = 2 \times LHWHM, \tag{4.5}$$

where $LHWHM$ is the left half-width-at-half-maximum of $\overline{D}_{r,SS}(t)$.

Uptake Rate UR

The uptake rate UR (another surrogate for transit time) is defined as the maximum value of the first derivative of $\overline{D}_{r,SS}(t)$ between t_{CA} and t_{PK} (Figure 4.5):

$$UR = \max(\overline{D}'_{SS}(t)) \qquad t_{CA} \leq t \leq t_{PK}, \tag{4.6}$$

where $\overline{D}'_{SS}(t)$ denotes the first derivative of $\overline{D}_{r,SS}(t)$. The time at which $\overline{D}'_{SS}(t) = UR$ is t_{UR}.

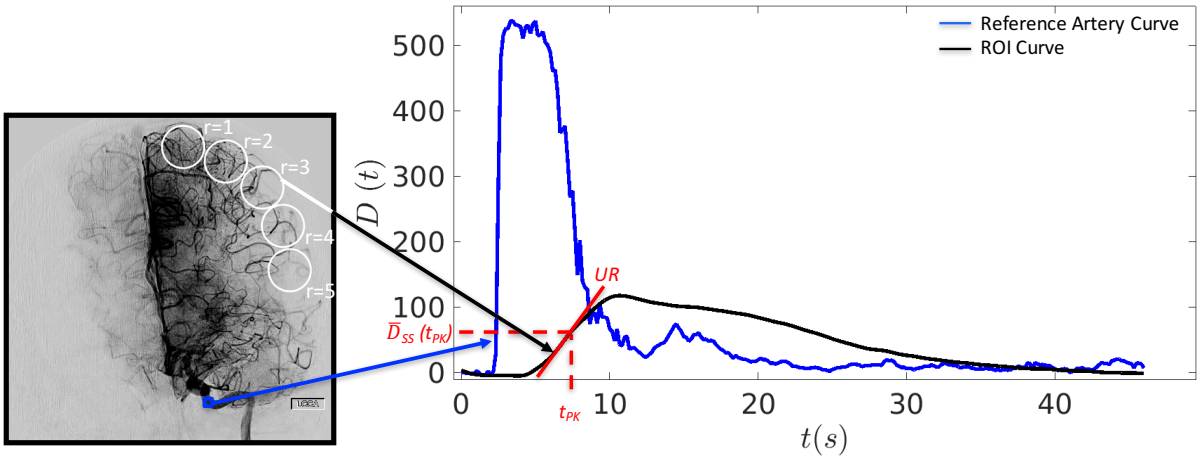

Figure 4.5: Features UR and $\overline{D}_{r,SS}(t_{UR})$.

Contrast Value at Uptake $\overline{D}_{r,SS}(t_{UR})$

The contrast value measured at t_{UR} was also extracted to understand the relationship between pial grade and a contrast curves inflection point during uptake.

Slope to Peak S

The slope-to-peak S was defined as the mean slope of $\overline{D}_{r,SS}(t)$ between t_{CA} and t_{PK}, or

$$S = \frac{\overline{D}_{r,SS}(t_{PK}) - \overline{D}_{r,SS}(t_{CA})}{t_{CA} - t_{PK}}. \tag{4.7}$$

This feature can be considered as an alternative to UR for inferring transit time.

ABF

Because $A_{D,Uptke}$ represents the volume of contrast filling in the ROI, we infer the perfusion through an ROI as the ratio

$$ABF = \frac{A_{D,Uptke}}{eMTT}. \tag{4.8}$$

4.2.4 Gold Standard "Truth" for the Kinetic Features

In order to assess the accuracy of the computer-extracted kinetic features (Section D), all features except for A_D measured in the Dataset A+B (see Table 2.2) were estimated manually, serving as the "gold standard truth". This was done for all cases in Dataset A+B.

Since t_{PK} was used to calculate $A_{D,Uptke}$, a manual measurement of t_{PK} (denoted as $t_{PK,Man}$) was made and verified by a board-certified radiologist (GAC). The resulting values of $A_{D,Uptke}$ using $t_{PK,Man}$ were then compared with those calculated with t_{PK}.

To assess the accuracy of PK, the automatically determined value of PK was compared against a manually chosen value that was verified by a board-certified radiologist. The corresponding time of this manually-determined PK was $t_{PK,Man}$.

Manual measurements of arrival time $t_{CA,Man}$ on plots of $\overline{D}(t)$ were designated as truth to compare against the corresponding automated measurement t_{CA}. Measured values of $t_{CA,Man}$ and $t_{CA,ICA}$ were verified by a board-certified radiologist who was blinded to the computerized calculation of t_{CA} and $t_{CA,ICA}$. The resulting AAT_{Man} was then treated as truth to be compared against the automatically calculated value in each ROI. Similarly, manual measurements of $t_{CA,ICA}$ and t_{PK} were used to calculate the TTP_{Man} to be compared against the automatically calculated TTP in each ROI.

Because UR was calculated between t_{CA} and t_{PK}, accuracy was measured by finding the maximum of $\overline{D}'_{SS}(t)$ between $t_{CA,Man}$ and $t_{PK,Man}$. The time of this maximum was denoted $t_{UR,Man}$. $\overline{D}_{r,SS}(t_{UR,Man})$ was treated as the truth against which the automatically-calculated $\overline{D}_{r,SS}(t_{UR})$ was compared.

The truth for $S, eMTT, A_{D,Uptke}$, and ABF were determined using the same equations as their automatically-calculated counterparts (Eqs. 4.3, 4.5 4.7, and 4.8, respectively) but $t_{CA,Man}$ and $t_{PK,Man}$ were used in the respective places for t_{CA} and t_{PK}.

4.2.5 Effect of Frame-Rate on Feature Values

To understand the performance of the kinetic features at frame-rate acquisitions typically used in the clinic, each angiogram acquired at 6 Fr/s (Dataset A, see Table 2.2) was subsampled to generate synthetic angiograms with temporal sampling according the dose-sparing mixed frame-rate protocol described (Dataset A_M, see Table 2.2). For each ROI in each case, the value of each feature was compared between the Datasets A and A_M. Comparisons were visualized using Bland-Altman analysis. The grand mean of values across all ROIs from Datasets A and A_M was calculated and compared against the range of feature values from the 6 Fr/s angiograms. In addition, the Bland-Altman bias, or mean difference, in feature values between the two frame-rates and the standard deviation σ of this difference were calculated. The Bland-Altman mean bias and $|simgma$ were compared against the grand mean and range. To assess the degree of consistency between feature values extracted

from Datasets A and A_M, the intraclass correlation (ICC) for each feature was calculated using a consistency definition and 2-way ANOVA [33].

4.2.6 Between-Injection Reproducibility of Kinetic Features

In the patient database, there were 7 cases that had repeated angiographic series (Datasets A_r and B_r, see Table 2.2). These repeated series were taken within 16 min of each other, allowing for intra-patient comparison of each extracted feature. Angiograms for 6 of the 7 cases were acquired at 6 Fr/s and the remaining case was acquired using the mixed frame-rate protocol. To understand the effect of temporal sampling on feature reproducibility, 2 separate datasets are analyzed (Table 4.3). The first, Dataset A_r consists of 6 Fr/s angiograms. The second, Dataset $A_{M,r} + B_r$, includes the angiograms from the cases acquired at the mixed frame-rate protocol (Dataset B_r) and synthetic angiograms downsampled from the 6 Fr/s angiograms in Dataset A to the mixed frame-rate protocol (Dataset $A_{M,r}$). For each feature in the r^{th} ROI, the measure feature value F was normalized by the extracted value of F in the first ROI (i.e, $r = 1$) of the series. In each dataset, the normalized value of F at the r^{th} ROI was then compared between each injection in a case and the comparisons for all ROIs in the 7 cases are visualized using Bland-Altman analysis. The Bland-Altman bias, or mean difference, in feature values between the two frame-rates and the standard deviation σ of this difference were calculated. To assess the degree of consistency between repeat injections, the intraclass correlation (ICC) for each feature was calculated using a consistency definition and 2-way ANOVA [33].

4.2.7 ROI Indices for each Kinetic Feature

The values for each kinetic feature F changes across the 5 (or 6) ROIs (Figure 4.1.) It is hypothesized that the magnitude of this response can be used to identify a patient's pial arterial supply. To account for differences in image quality caused by differences in image acquisition (such as differences in tube voltage, tube current, contrast injection volume, im-

Angiograms	N	Dataset A_r	Dataset $A_{M,r} + B_r$
Angiograms acquired at 6 Fr/s (Dataset A_r)	6	✓	
Angiograms downsampled from 6 Fr/s to mixed frame-rate protocol (Dataset $A_{M,r}$)	6		✓
Angiograms acquired according to the mixed frame-rate protocol (Dataset B_r)	1		✓

Table 4.3: Datasets in which between-injection reproducibility is assessed (Also found in Table 2.2). Note that angiograms from cases with mixed frame-rates (Datasets $A_{M,r}$ and B_r) are placed into one dataset.

age magnification, or proprietary vendor post-processing) the value for $F(r)$ was normalized by the extracted value of F at $r = 1$ (i.e., the first ROI). Because vascular flow has been shown to follow an exponential response function in space and time (*Ostergaard et. al, 1996*) [38, 39], the normalized feature values $F_{Norm}(r)$ was fitted according to the following equation:

$$F_{Norm}(r) = e^{\beta(r-1)} \tag{4.9}$$

where r is the ROI index defined according to Figure 4.1, β is the parameter of exponential response for the particular feature F, and F_{Norm} is the normalized feature value. The fitting was done using the Levenberg-Marquardt algorithm. To harmonize the dataset, the 6 Fr/s angiograms were down-sampled to create synthetic angiograms with temporal sampling according to the mixed frame-rate acquisition protocol (see Section 2). The goodness-of-fit R^2 and the root-mean-square error (RMSE) were calculated for each case.

4.2.8 Classification-Performance Evaluation

For this section, 3 datasets are used (Table 4.4). The first, the Dataset A (see Table 2.2), is composed only of angiograms acquired at 6 Fr/s. Dataset A_d consists of angiograms downsampled from Dataset A to the mixed frame-rate protocol. Finally, Dataset A_M+B (see Table 2.2) consists of the angiograms in Dataset A_M and the angiograms from cases

Cases	Dataset A	Dataset A_M	Dataset A_M+B
Cases imaged at 6 Fr/s ($N = 11$)	✓		
Cases with angiograms downsampled to mixed frame-rate protocol ($N = 11$)		✓	✓
Cases imaged according to the mixed frame-rate protocol ($N = 13$)			✓

Table 4.4: Data subsets for box plots in Figures 4.14 and 4.15.

imaged under the mixed frame-rate protocol (Dataset B). For each dataset, the potential usefulness of each kinetic feature was determined by its ability to separate patients into two different PAS subpopulations (Table 4.5). Task I was the separation of PAS grade $p_c = 1$–2 (considered favorable PAS) vs $p_c = 3$–5 (considered poorer PAS); Task II was the separation of PAS grade $p_c = 1$–3 (for which treatment was feasible) vs $p_c = 4$–5 (for which treatment was to be avoided). Box plots are generated for the distribution of each feature F with populations with $p_c = 1$–2, $p_c = 3$, and $p_c = 4$–5. For each feature F derived from and task performed on Dataset A_M+B, a Receiver Operating Characteristic (ROC) curve was generated by sweeping a threshold β_{TH} across the subpopulations' distributions of β and then measuring the True Positive and False Positive Fractions at each choice of β_{TH}. The Wilcoxon area under the ROC curve AUC [3, 40] was used as the metric performance in distinguishing between the two PAS subpopulations.

Task	PAS sub-population 1	PAS sub-population 2
I	$p_c = 1$–2	$p_c = 3$–5
II	$p_c = 1$–3	$p_c = 4$–5

Table 4.5: Two separation task for PAS-subpopulations. The difference between tasks hinged on whether patients with a borderline PAS score ($p_c = 3$) were considered suitable for reperfusion treatment.

4.3 Results

4.3.1 Gold Standard "Truth" for the Kinetic Features

Figures 4.6 and 4.7 displays the Bland-Altman plots and correlations plots, respectively for the accuracy of the kinetic features measured in Dataset A+B. In Figures 4.6a, b, g, and h, the mean bias and standard deviation were very small compared to the Bland-Altman mean and range. For these features, there was high agreement between the truth and computer-calculated features except at lower values (Figure 4.7a, b, g, and h). For $eMTT$, the discrepancies occurred between 10–23 sec and can exceed 100% of the truth values. One cause of discrepancy for these four features was low contrast volume in certain ROIs. In this situation, the signal of opacification in $\overline{D}_{r,SS}(t)$ was averaged out by the numerous pixels with no contrast flowing through them. A total of 6 ROIs coming from 3 cases were affected in this manner. Another cause was motion artifact arising near the end of the angiogram for one case; 2 ROIs were affected. Therefore, these results suggested that when sufficient signal was present (i.e., signal with normalized $PK > 0.08$), and motion was minimized, measurement of these features was highly robust. However, in the absence of these conditions, the accuracy could degrade, particularly for $eMTT$. For the purposes of measuring feature response and classifying patients (next 2 sections), a workaround for cases with ROIs that had normalized $PK < 0.08$ would be to omit the associated $eMTT$ from exponential fitting. For motion artifacts, correction prior to feature extraction would be necessary.

In Figures 4.6c and 4.7c, discrepancies ΔAAT in AAT lay in bands that were multiples of 1/6 sec, reflecting the synthetic sampling of the smoothing spline fit to $\overline{D}(t)$. The worst discrepancies ($|\Delta AAT| > 9$ sec) were caused by the 6 ROIs with heavily-averaged opacification, reflecting the fact that the contrast curve was too weak to distinguish from image noise. These 6 ROIs skewed the mean bias and standard deviation to normalized values of $\geq 0.67 sec$ in Figure 4.6b. The shift in frame-rates at 4 or 4.33 sec was another major source of error, with the associated $|\Delta AAT|$ ranging from 0.50–1.17 sec. One ROI suffering from

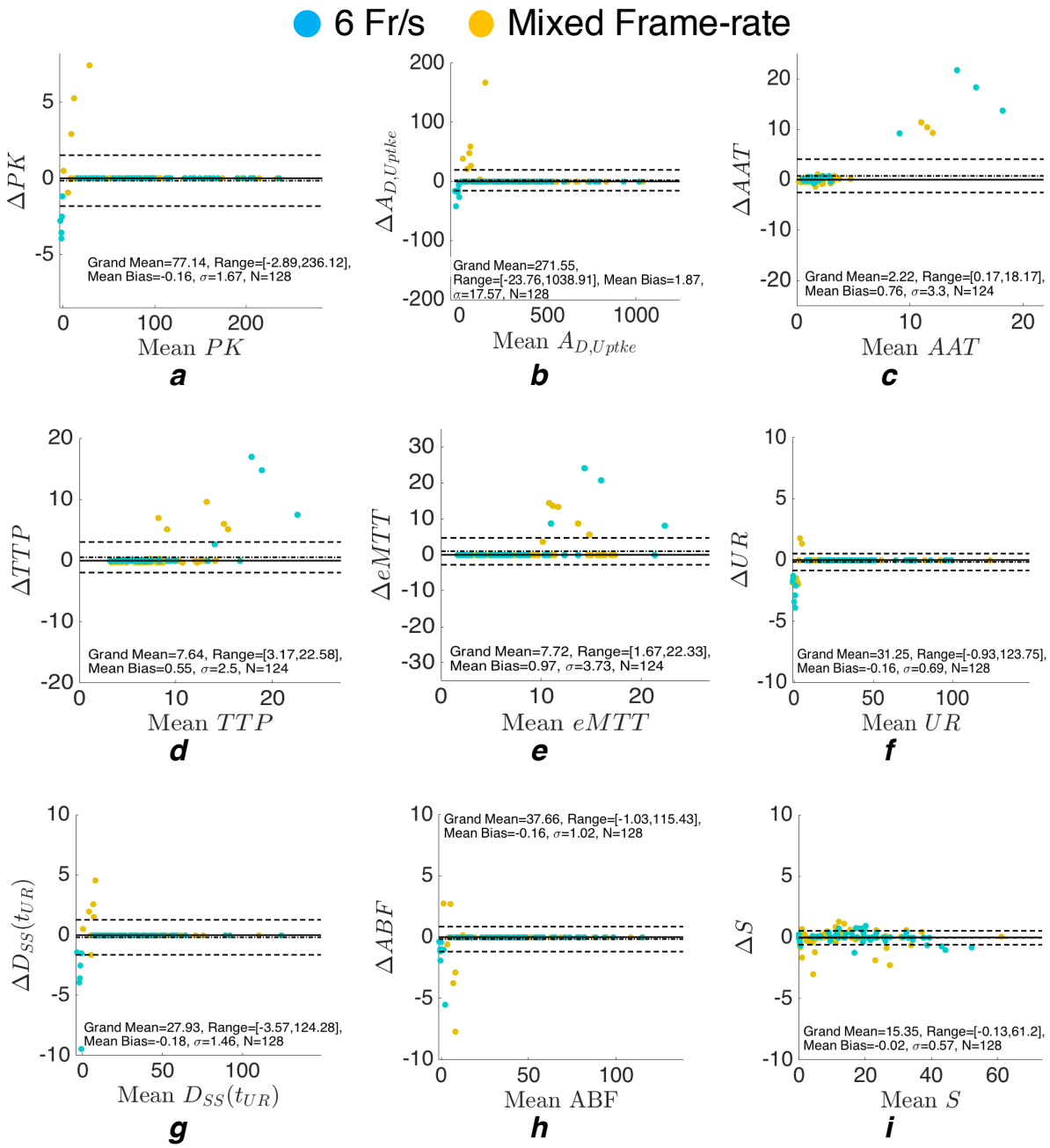

Figure 4.6: Bland-Altman plots for feature accuracy (Dataset A+B). The standard deviation σ is indicated by the dashed line in each kinetic feature's plot.

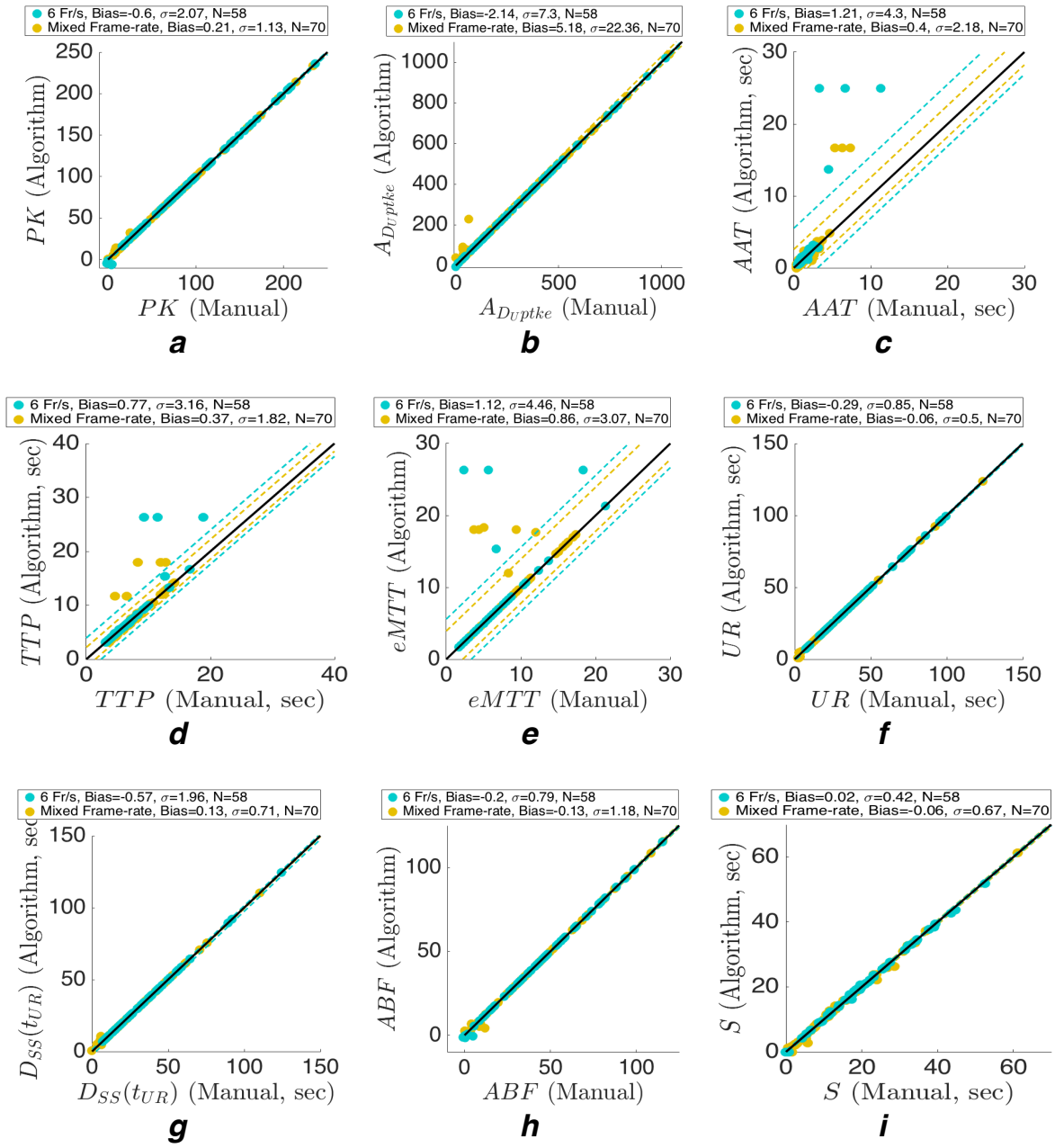

Figure 4.7: Correlation plots for feature accuracy (Dataset A+B). The Bland-Altman standard deviation σ for each frame-rate is indicated by the dashed lines in each kinetic feature's plot. Note that for all but the timing features and $A_{D,Uptke}$, the σ are too small to make out against the plotted points and the unity line.

substantial motion artifact prior to contrast arrival had $\Delta AAT = 1.33$ sec, highlighting the effect motion had on timing measurements. Algorithm limitations and skull lightening prior to contrast arrival frequently caused $0.17 \leq |\Delta AAT| \leq 0.6$ sec, reflecting the best accuracy available when sampling at uniform frame-rates of 3 or 6 Fr/s and when motion is reduced.

In Fig 4.6d, discrepancies of $\Delta TTP \geq 2.67$ sec were caused either by low opacification or motion artifact. Other errors were caused by $t_{CA,ICA}$ discrepancy of up to 0.33 sec. For the majority of ROIs in the database however, there was no difference between the manually- and the automatically-determined TTP.

In Figs 4.6f, g, and i, there was high agreement (Mean Bias of $< 1, \sigma < 1$) between the automatically-determined values of and the truth values for $UR, \overline{D}_{r,SS}(t_{UR})$, and S. Discrepancies in UR and $\overline{D}_{r,SS}(t_{UR})$ were caused by weak opacification, uneven frame-rate, or motion artifact. Those discrepancies were $\geq 8\%$ and $\geq 20\%$ of the root of the variance of the distribution of UR_{Man} and $\overline{D}(t_{UR,Man})$, respectively. Furthermore, these discrepancies occur only for values $UR_{Man} < 8.05$ and $\overline{D}(t_{UR,Man}) < 3.07$. Discrepancies in S had the same causes as those for both AAT and PK because of the use of both t_{CA} and t_{PK} in the calculation of S. These results indicate that in the presence of uneven Frame-rate and sufficient signal, $UR, \overline{D}_{r,SS}(t_{UR})$, and S were accurate.

4.3.2 Effect of Frame-Rate on Feature Values

In Table 4.6, the Bland-Altman bias between Datasets A and A_M for each feature is small and except for $\overline{D}_{r,SS}(t_{UR})$, the Bland-Altman standard deviation σ relative to the respective grand mean was $< 20\%$. The Bland-Altman standard deviation σ for $A_{D,Uptke}$, the timing features, $\overline{D}_{r,SS}(t_{UR})$, and S are greater than 6% of those features' respective grand means. In particular, $\overline{D}_{r,SS}(t_{UR})$ suffered the worst from downsampling, with $\sigma = 39\%$ of its grand mean and having $> 5\%$ error between the frame-rates in 59% of all ROIs. A_D, PK, and ABF, by contrast, had $\sigma \leq 3\%$ of their grand means and their values from $\geq 90\%$ of all ROIs agreed to within 5% error.

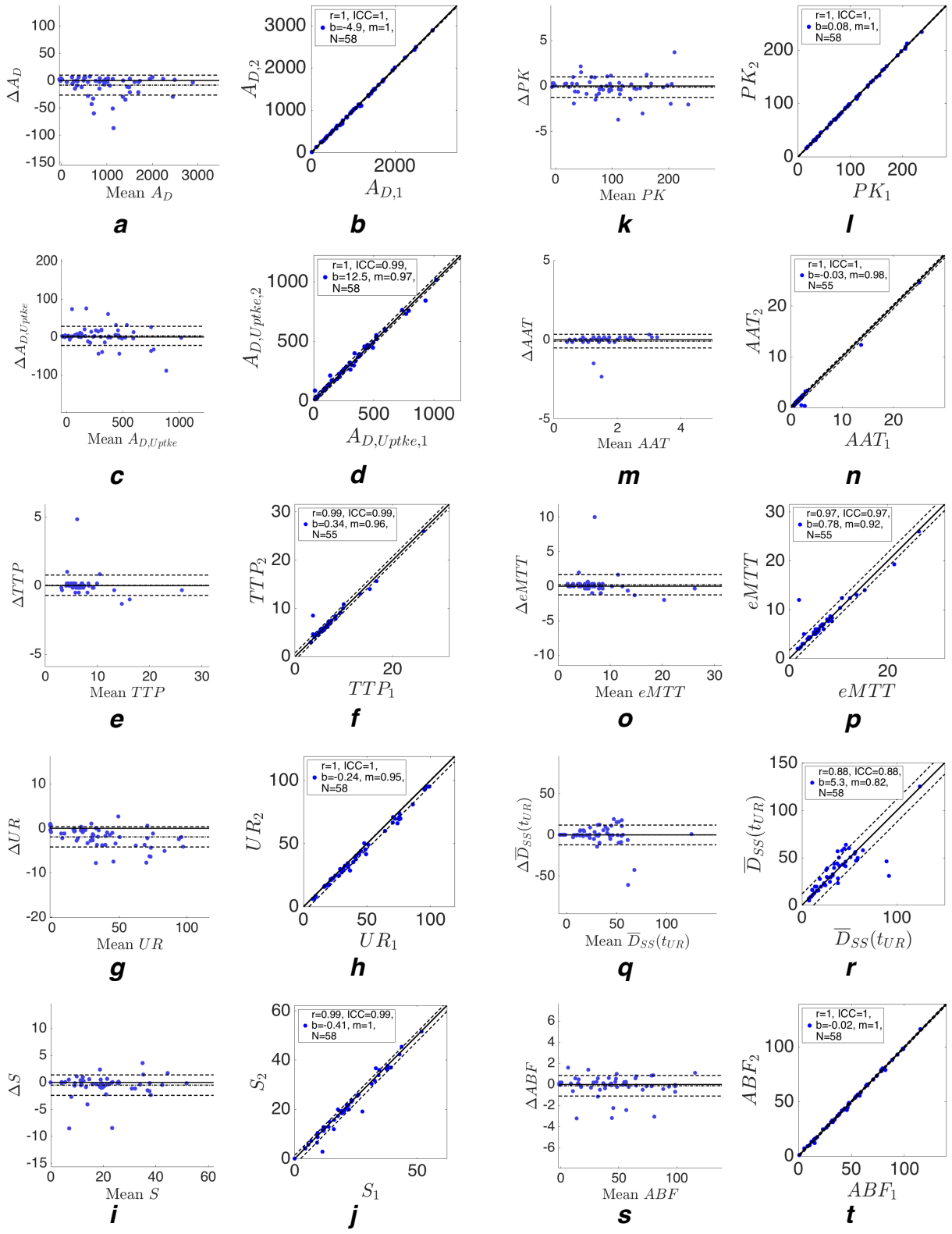

Figure 4.8: Correlation and Bland-Altman plots for effect of downsampling (i.e., comparing Datasets A and A_M; see Table 2.2)

Feature	**Number of ROIs (11 cases)**	**Range (6 Fr/s)**	**Grand Mean**	**Bland-Altman Bias**	**Bland-Altman σ**	**Fraction of ROIs within (5%)**
A_D	58	[-39.87,2893.96]	926.20	-8.38	18.24	0.93
PK	58	[-6.74, 236.12]	88.83	0.14	1.13	0.98
$A_D, Uptke$	58	[-39.87, 1018.73]	286.47	3.02	25.18	0.55
AAT	55	[0.50, 25.00]	2.94	-0.09	0.43	0.55
TTP	55	[3.17, 26.33]	7.66	0.03	0.74	0.82
$eMTT$	55	[1.67, 26.33]	7.57	0.21	1.46	0.55
UR	58	[2.07, 99.26]	36.74	-2.03	2.18	0.48
$\overline{D}_{r,SS}(t_{UR})$	58	[-1.19, 124.28]	30.95	-0.13	12.00	0.41
S	58	[0.00, 51.77]	18.66	-0.50	1.89	0.66
ABF	58	[-1.51, 115.17]	43.3	-0.12	0.97	0.90

Table 4.6: Bland Altman Statistics for the effect of temporal subsampling on extracted features (i.e., comparison is made using Datasets A and A_M; see Table 2.2).

4.3.3 Between-Injection Reproducibility of Kinetic Features

For Dataset A_r (Figure 4.9 and Table 4.7), the normalized values for all features except AAT had little mean bias (< 0.15). The cause of the large bias in normalized AAT arises from 4 ROIs with heavily averaged opacification. The averaging also skewed the Bland-Altman standard deviation σ for AAT. Normalized A_D, PK, $A_{D,Uptke}$, UR, S, and ABF had reduced standard deviations ($\sigma \leq 0.26$). By contrast, the AAT,TTP,$eMTT$, and $\overline{D}_{r,SS}(t_{UR})$ had considerably greater standard deviation ($\sigma \in [0.33, 3.92]$). These greater σ are influenced by outliers. Interestingly, ABF, which is derived from the less reliable $eMTT$, is very reproducible. This may be because effects from difference in imaging acquisition cancel out in Eq. 4.8. Furthermore, AAT and $\overline{D}_{r,SS}(t_{UR})$, which have the highest σ, also had the lowest ICC of all features. The Bland-Altman bias and σ for Dataset $A_{M,r} + B_r$ (Figure 4.10 and Table 4.8) closely mirror those for Dataset A_r, except that the ICC for AAT,TTP, and $\overline{D}_{r,SS}(t_{UR})$ are noticeably lower ($|\Delta ICC \geq 0.06$).

Feature (6 cases, 31 ROIs)	**Bland-Altman Mean Bias**	**Bland-Altman Standard deviation σ**	**Intraclass Correlation** (ICC)
A_D	-0.02	0.11	0.95
PK	-0.05	0.10	0.97
$A_{D,Uptke}$	0.01	0.23	0.87
AAT	-1.45	3.92	0.84
TTP	-0.05	0.33	0.92
$eMTT$	-0.02	0.39	0.87
UR	-0.11	0.26	0.91
$\overline{D}_{r,SS}(t_{UR})$	-0.14	0.42	0.65
S	-0.08	0.16	0.94
ABF	-0.05	0.15	0.96

Table 4.7: Reproducibility statistics for features extracted from Dataset A_r (6 Fr/s angiograms, 6 cases, 31 ROIs total). The mean bias and standard deviation σ are drawn from Bland-Altman Analysis, while the intraclass correlation coefficient ICC is calculated using 2-way ANOVA.

Feature (7 cases, 36 ROIs)	**Bland-Altman Mean Bias**	**Bland-Altman Standard deviation σ**	**Intraclass Correlation** (ICC)
A_C	-0.01	0.11	0.95
PK	-0.05	0.09	0.97
$A_{C,Uptke}$	0.04	0.20	0.90
AAT	-0.87	2.73	0.87
TTP	-0.02	0.34	0.89
$eMTT$	0.08	0.39	0.84
UR	-0.06	0.20	0.95
$\overline{D}_{r,SS}(t_{UR})$	0.01	0.38	0.70
S	-0.08	0.13	0.96
ABF	-0.06	0.12	0.95

Table 4.8: Reproducibility statistics for features extracted from Dataset $A_M + B$ (7 cases, 31 ROIs total; see Table 4.4). The mean bias and standard deviation σ are drawn from Bland-Altman Analysis while the intraclass correlation coefficient ICC is calculated using 2-way ANOVA.

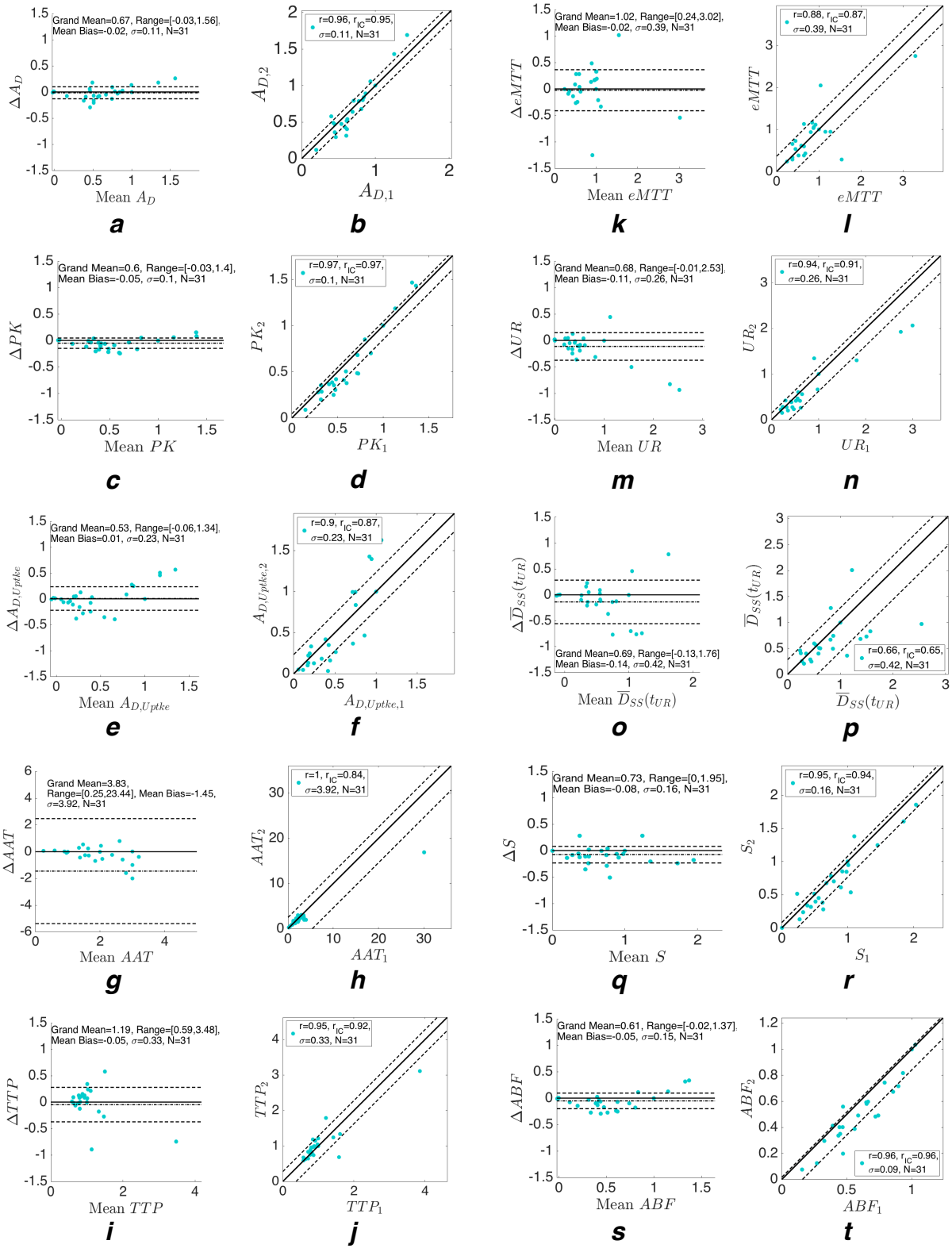

Figure 4.9: Reproducibility of kinetic features between subsequent angiograms for Dataset A_r (see Tables 2.2 and 4.3). In the correlation plots, $r_{IC} = ICC$.

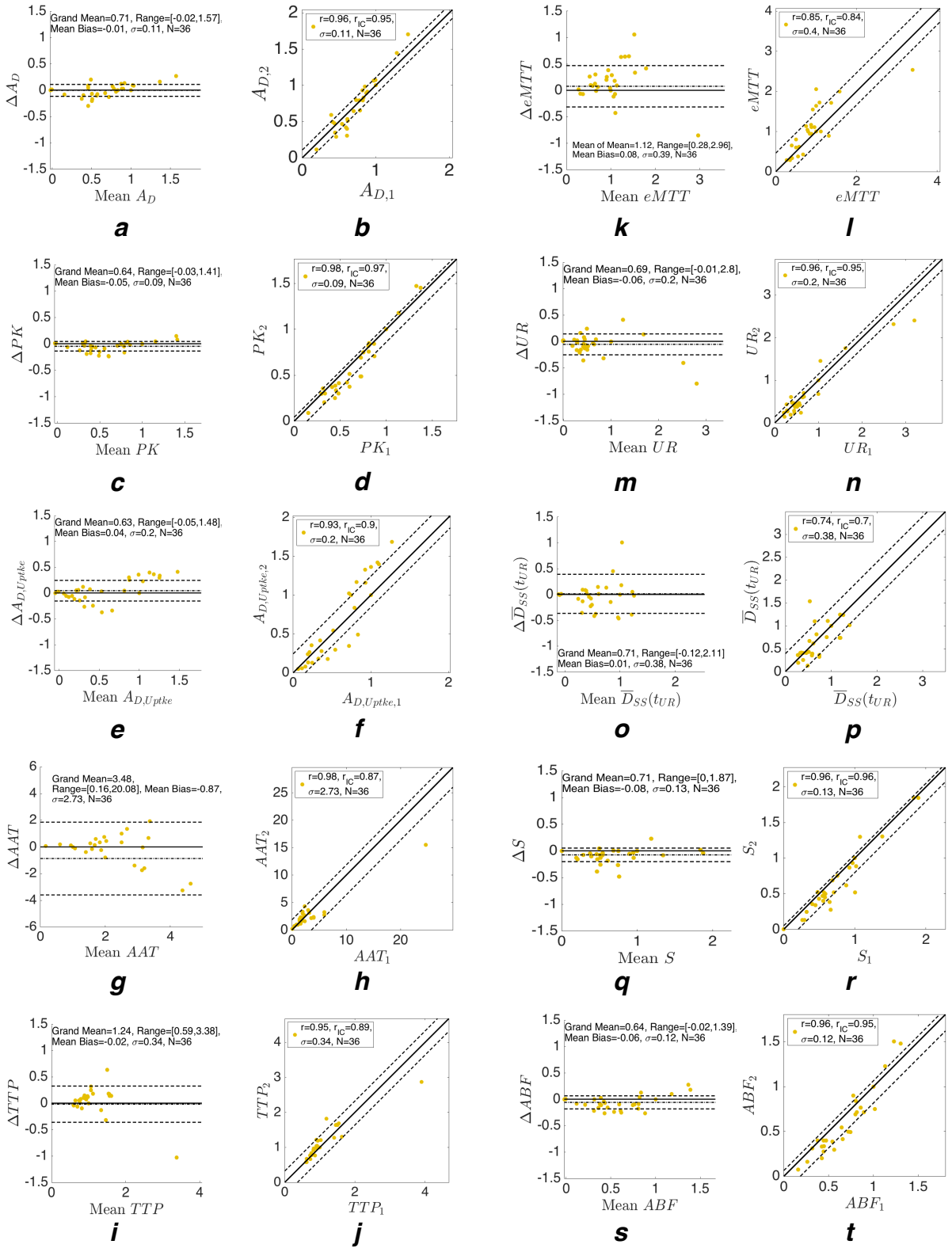

Figure 4.10: Reproducibility of kinetic features between subsequent angiograms for Dataset $A_M, r + B_r$ (see Table 4.3). In the correlation plots, $r_{IC} = ICC$.

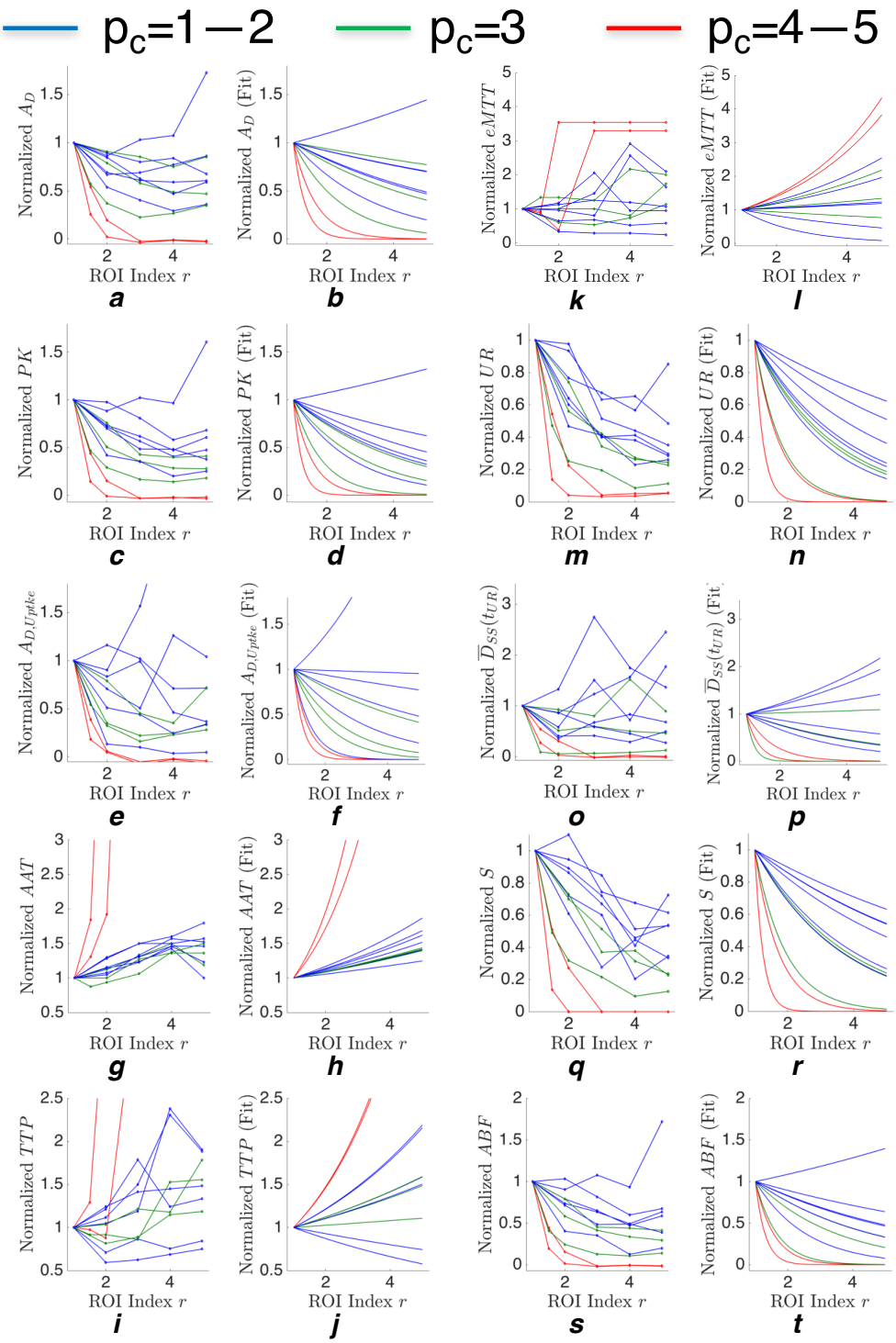

Figure 4.11: Kinetic Feature behavior as a function of ROI index r (see Eq. 4.9) for Dataset A (see Tables 2.2 and 4.4). The plots of normalized $A_D, A_{D,Uptke}, AAT, PK$, and TTP are in 1st column and the associated fits are in the 2nd column. Similarly, plots of normalized $UR, \overline{D}_{r,SS}(t_{UR}), eMTT$, ABF, and S are in the 3rd column and the associated fits are in the 4th column.

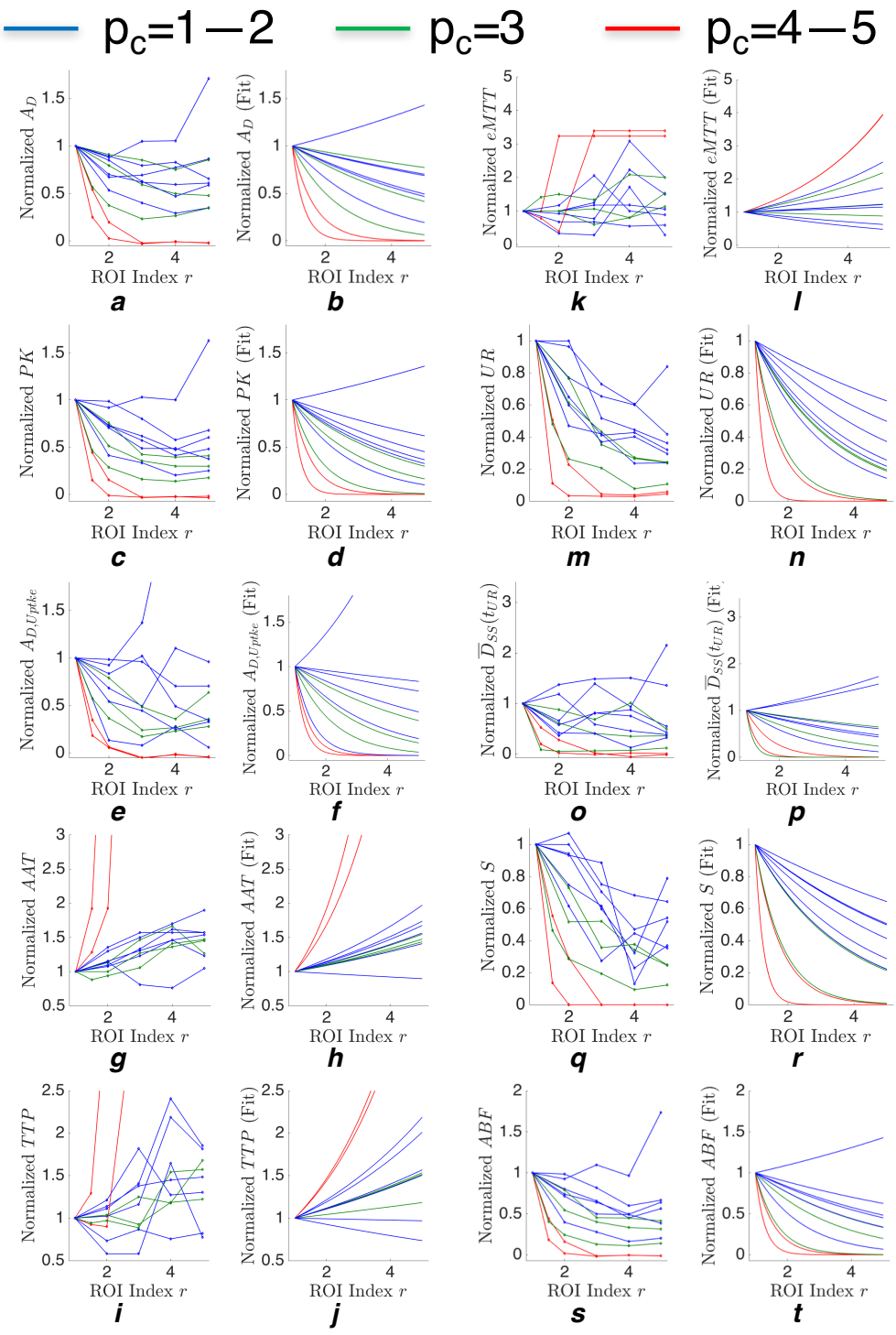

Figure 4.12: Kinetic Feature behavior as a function of ROI index r (see Eq. 4.9) for Dataset A_M (see Tables 2.2 and 4.4). The plots of normalized $A_D, A_{D,Uptke}, AAT, PK$, and TTP are in 1st column and the associated fits are in the 2nd column. Similarly, plots of normalized $UR, \overline{D}_{r,SS}(t_{UR}), eMTT$, ABF, and S are in the 3rd column and the associated fits are in the 4th column.

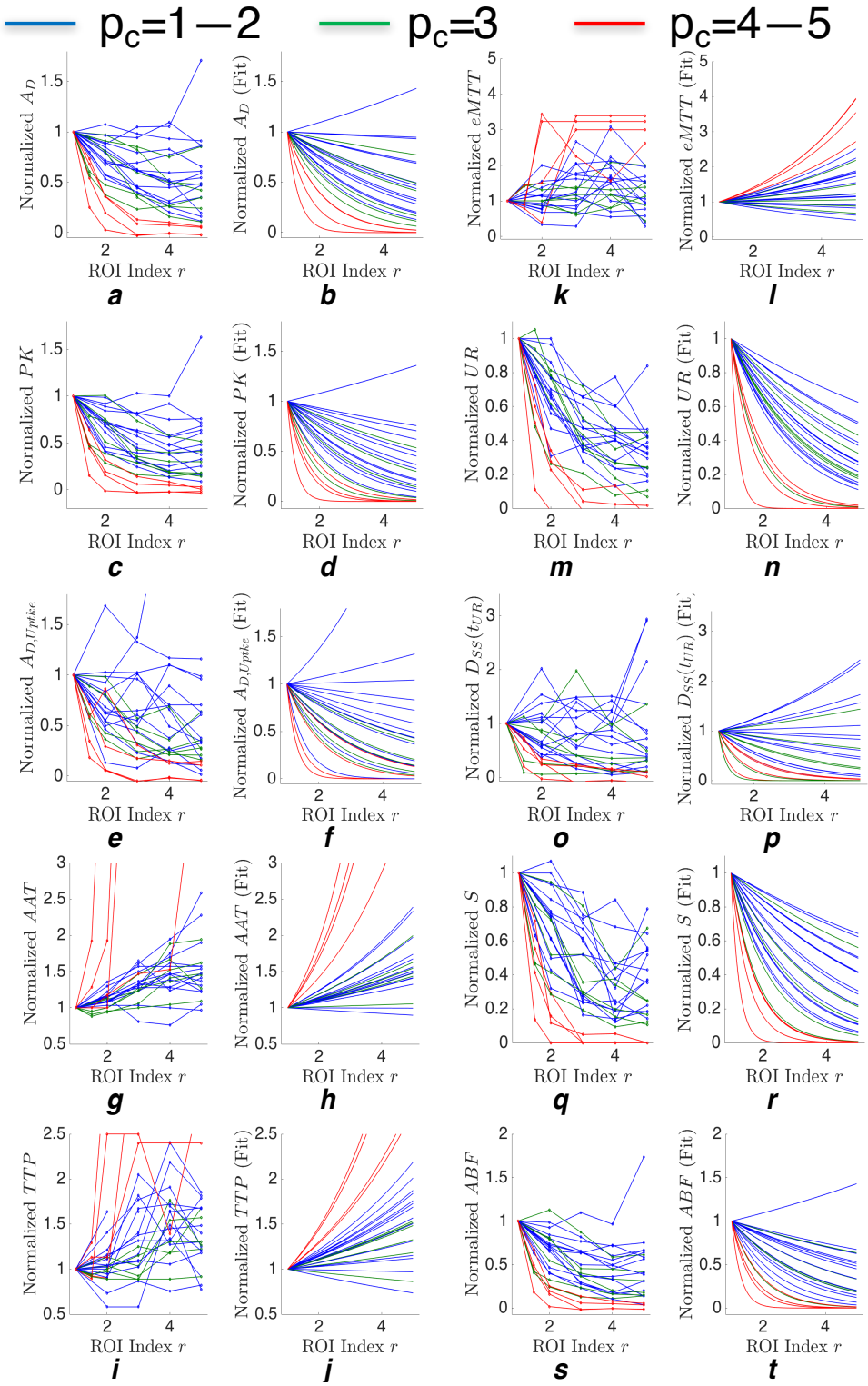

Figure 4.13: Kinetic feature behavior as a function of ROI index r for Dataset $A_M + B$ (Tables 2.2 and 4.4). Plots of normalized $A_D, A_{D,Uptke}, AAT, PK$, and TTP are in 1st column and the associated fits are in the 2nd column. Similarly, plots of normalized $UR, \overline{D}_{r,SS}(t_{UR}), eMTT$, ABF, and S are in the 3rd column and the associated fits are in the 4th column.

4.3.4 ROI Indices for each Kinetic Feature

Figure 4.11 show plots the kinetic features from cases in the Dataset A against the ROI number (first and third column) along with the associated exponential fits (second and fourth column).Figures 4.12 and 4.13 are similar, except that they show plots and fits for angiograms from Datasets A_M and $A_M + B$, respectively. As can be seen from these 3 figures and from Figure 4.14, for all features, there is very little difference in the fits and β distributions between Datasets A and A_M. Therefore, performance for Tasks I and II would not change appreciably between Datasets A and A_M. Therefore, the following results and analysis will focus on Dataset $A_M + B$. The corresponding mean and standard deviation R^2 and RMSE of the fits in Figure 4.13 taken over all cases was shown in Table 4.9.

Feature	$\mathbf{R^2}$	**RMSE**	**AUC for Task I ($\mathbf{p_c}$ = 1–2 vs) ($\mathbf{p_c}$ = 3–5)**	**AUC for Task II ($\mathbf{p_c}$ = 1–3 vs) ($\mathbf{p_c}$ = 4–5)**
A_D	0.74 ± 0.34	0.09 ± 0.05	0.81 ± 0.10	$1.00 \pm 0.00*$
PK	0.86 ± 0.15	0.08 ± 0.04	0.84 ± 0.09	0.99 ± 0.02
$A_{D,Uptke}$	0.63 ± 0.45	0.15 ± 0.09	0.84 ± 0.08	0.94 ± 0.06
AAT	0.57 ± 0.36	0.51 ± 1.04	0.7 ± 0.12	$1.00 \pm 0.00*$
TTP	0.36 ± 0.40	0.31 ± 0.29	0.59 ± 0.13	$1.00 \pm 0.00*$
$eMTT$	0.12 ± 0.40	0.44 ± 0.28	0.66 ± 0.13	$1.00 \pm 0.00*$
UR	0.87 ± 0.19	0.08 ± 0.04	0.77 ± 0.11	0.98 ± 0.03
$D_{r,SS}(t_{UR})$	0.58 ± 0.42	0.20 ± 0.16	0.81 ± 0.09	0.9 ± 0.06
S	0.83 ± 0.15	0.10 ± 0.05	0.82 ± 0.10	$1.00 \pm 0.00*$
ABF	0.84 ± 0.17	0.09 ± 0.05	0.81 ± 0.10	0.98 ± 0.03

Table 4.9: Feature exponential fit statistics (Dataset A_M+B; see Figure 4.13 and Table 4.4) and Area AUC under the ROC curve for two classification tasks. *Results of $AUC = 1$ are likely due to small patient sample size

Density-based features such as A_D, PK, S, UR and ABF had the best fits (mean $R^2 > 0.70, \sigma_{R2} < 0.40$; mean $RMSE \leq 0.10, \sigma_{RMSE} \leq 0.05$) and their respective β clearly separated patients with p_c = 1–2 from patients with p_c = 4–5 (see Figures 4.15b,e,f,i, and j). Patients with $p_c = 3$ were not as cleanly separated from those with good or patently poor p_c, however. Other density-based features such as $\overline{D}_{r,SS}(t_{UR})$ and $A_{D,Uptke}$ had poorer fits (mean $R^2 < 0.70, \sigma_{R2} > 0.40$; mean $RMSE > 0.10, \sigma_{RMSE} > 0.10$) and worse separation

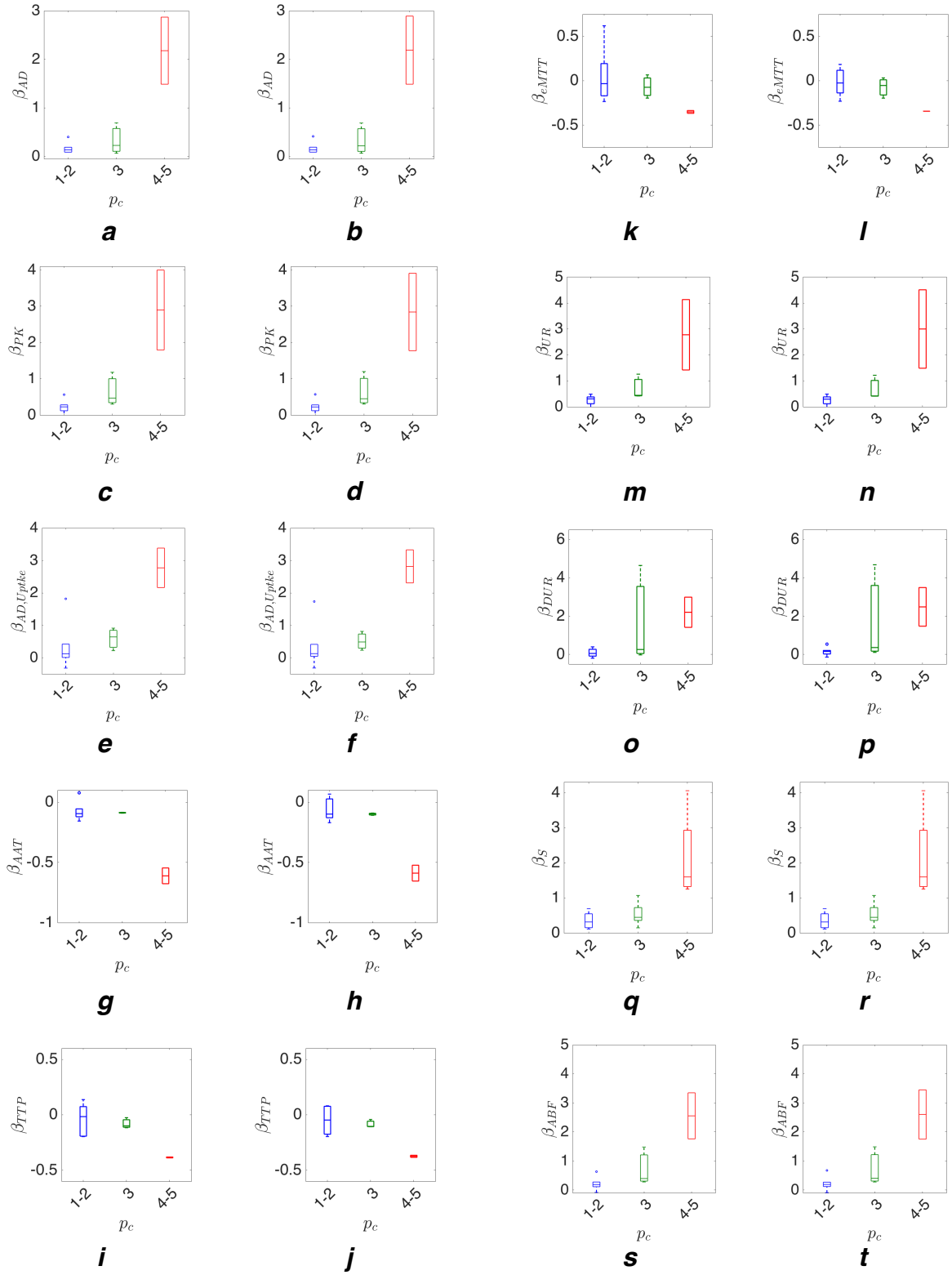

Figure 4.14: Box plots for features extracted from angiograms in Dataset A(1st and 3rd columns; see Table 2.2) and for Dataset A_M (2nd and 4th columns).

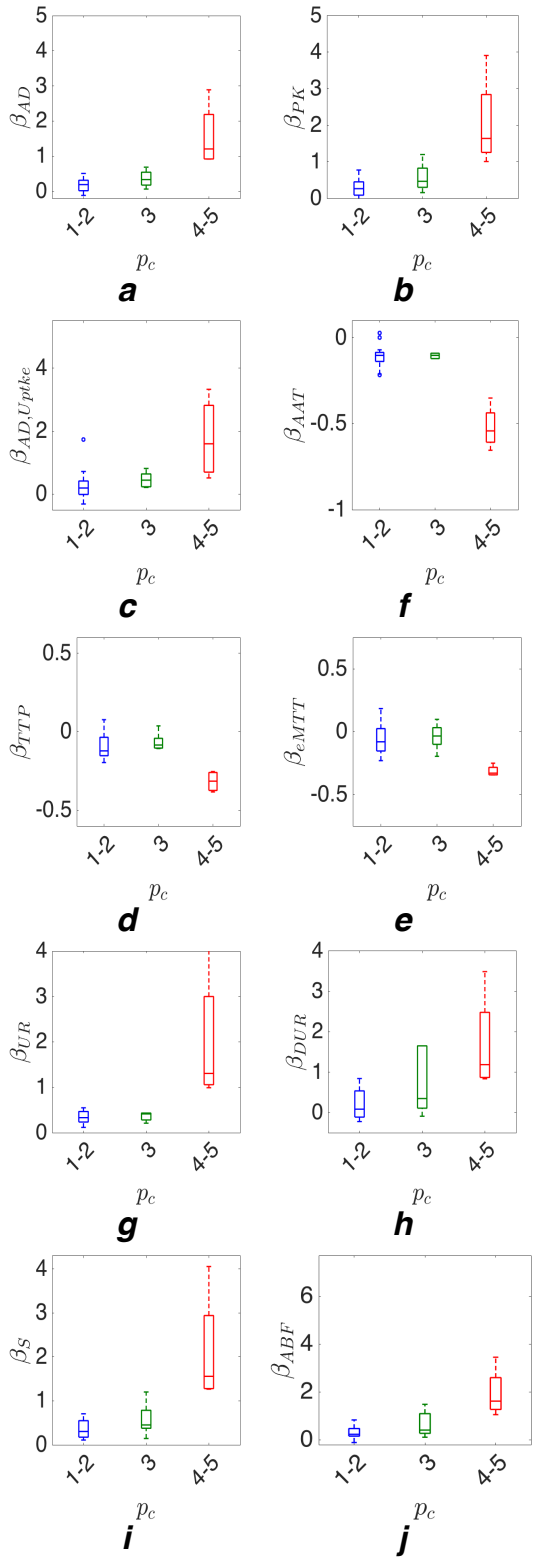

Figure 4.15: Box plots of exponential decay parameters for each feature in Dataset $A_M + B$.

between the p_c = 1–2 and p_c = 4–5 groups (see Figures 4.15a and 4.15g). In Figure 4.13a and 4.13c, there was higher noise for these 2 features than for the other density-based features. The worse fits for the latter two density-based features can be attributed to "noisy" variations in their normalized values.

Timing Features such as TTP and $eMTT$ had poorer fits than $\overline{D}_{r,SS}(t_{UR})$ and do not appear to follow an exponential fit. The timing features from cases with p_c = 4–5 reach horizontal asymptotes at $r \geq 2$, which suggests that these features (particularly $eMTT$) follow more logistic patterns. The fit to AAT does fare better than TTP or $eMTT$, but was still worse than most of the density-based features. Of the time-based features, $eMTT$ provides the best separation between the p_c groups, and, like the density-based features, clearly separates p_c = 1–2 from p_c = 4–5.

4.3.5 Classification-Performance Evaluation

Table 4.9 gives the Wilcoxon estimates for the area under the ROC curves AUC for the

task of distinguishing between patients with $p_c = 1$–2 from those with $p_c = 3$–5 (Task I). All density-based features had $AUC > 0.80$ except for UR; UR fares worse because of extensive overlap in β_{UR} values between with $p_c = 1$–2 and $p_c = 3$–5 (see Figure 4.15e). However, the timing-based features–AAT, TTP, and $eMTT$–had AUC that were little better than guessing. It was found that the density features with the best AUC were amongst the features with the best exponential fits (on average). For the task of distinguishing between $p_c = 1$–3 and $p_c = 4$–5 (Task I), all features except for AAT and TTP had $AUC > 0.90$, with $A_D, PK, eMTT, S$ and UR having the best performance.

4.4 Discussion

4.4.1 Feature Accuracy Relative to the Gold Standard "Truth"

To quickly and objectively assess pial arterial supply (PAS), an automatic means of extracting angiographic contrast-time curves from the ischemic region was developed. Within ROIs placed in angiograms, ten features were extracted from each smoothed contrast-time curve to characterize and classify the degree of retrograde filling. In each case, we find either an approximate exponential decay of certain features (UR, PK, A_D) or an approximate exponential growth of other kinetic features (AAT). This corroborates prior modeling of vascular dispersion as an exponential falloff along the vascular tree [38, 39]. Therefore, our results suggested that when normalization to the first ROI was performed, the response of each feature through the ischemic region was governed primarily by anatomic and physiologic effects.

The results suggest that when sufficient signal was present (i.e., signal with normalized $PK > 0.08$), and motion is minimized, measurements of $PK, A_D, A_{D,Uptke}$ and ABF were highly accurate and reproducible (Figures 4.6, 4.7, 4.9, and 4.10).

When sufficient signal was not present (i.e., signal with normalized $PK < 0.08$), or motion was substantial, however, the accuracy could degrade, particularly for $eMTT$. For

the purposes of measuring feature response and classifying patients (next 2 sections), a workaround for cases with ROIs that had normalized $PK < 0.08$ would be to omit the associated $eMTT$ from exponential fitting. For motion artifacts, correction prior to feature extraction would be necessary. Because motion artifacts can diminish the accuracy of the calculated feature values, it is important to reduce patient motion during the acquisition. Anesthesia may be appropriate for some patients, and for other cases physical immobilization during imaging would be necessary [Dr. Christoforidis can best weigh in.].

One method for improving AAT accuracy is to image at a uniform frame rate. Because measurement of $t_{CA,Man}$ was done using $\overline{D}(t)$, the human observer had a high uncertainty in finding the the true t_{CA} because of the coarse 1 Fr/s sampling rate. For this reason, it is recommended that angiography for automatic AAT measurement be conducted at a uniform 3 or 6 Fr/s.

4.4.2 Kinetic Feature Reproducibility between Injections

The results suggest that, between injections, features that are surrogates for CBV (A_D and PK) Perfusion (ABF) are the most reproducible of the features examined in this study, while density-based features that are surrogates for CBF (S, and UR) and $A_{D,Uptke}$, TTP, are somewhat less reproducible. Motion and noise between repeated series can lower this reproducibility. Therefore, to better apply CBF surrogates to dynamic patient monitoring, it is important to reduce patient motion during the acquisition. AAT, $\overline{D}_{r,SS}(t_{UR})$, and $eMTT$ were amongst the least reproducible features. TTP and $eMMT$ are sensitive to changes in the time at which $\overline{D}_{r,SS}(t)$ peaks and in the value of PK; this is especially important when there are distinguishable peaks for arterial and venous filling. AAT can be sensitive to injection volume and rate. Furthermore, all timing features have poor intra-series agreement in ROIs with low contrast concentration (i.e., ROIs with normalized $PK < 0.08$), making them less reliable for assessing patients with poor PAS.

4.4.3 Classification-Performance Evaluation

The similarity in fits seen in Figures 4.12 and 4.11 and the corresponding similarity in β seen in Figure 4.14 for all p_c indicate that despite the difference in feature values between 6 Fr/s angiograms and corresponding downsampled mixed frame-rate angiograms, Levenberg-Marquardt fitting is robust. Therefore, performance for Tasks A and B would not change appreciably between the two different frame-rates for the cases in the Dataset A. As is shown in Figure 4.15 and reflected in Table 4.9, there was categorically greater exponential growth or decay (i.e., greater β) of $A_D, A_{D,Uptke}, PK, eMTT, S$, and ABF for patently poor PAS ($p_c = 4$–5) versus PAS ($p_c = 1$–3). These results indicated that, for each of those features, there was a definite range of a where the risks of reperfusion treatment rise considerably. This range also reflected the relatively smaller penumbra volumes in the ischemic region, indicating reduced benefits to reperfusion treatment. Therefore, these features may be used to screen out cases best suited to alternative treatments or no treatment.

4.4.4 Limitations

Because motion, noise, and low contrast concentration between repeated series reduce the reproducibility of density-based features that are surrogates for CBF, it is important to reduce patient motion during the acquisition. When done under anesthesia, patient motion is reduced. The development of robust motion-correction techniques may also help improve the reporducitbility of CBF surrogates. Standardizing injection rates and ensuring that there is enough contrast to visualize the entire extent of PAS could help improve reproducibility as well.

Although A_D, PK, AAT, S, and ABF could readily distinguish patients with good PAS from those with poor PAS, this study was performed with only 24 patients, 4 of whom had poor PAS; The results are thus skewed toward patients with $p_c \leq 3$. This is because patients with poor PAS tend to have lower ASPECTS scores and are not sent to interventional angiography.

The reduced abilities to distinguish borderline cases ($p_c = 3$) from poor PAS ($p_c = 4$–5) or from good PAS ($p_c = 1$–2) were problematic. Projection imaging can often lead to overlap of external vascular structure with the affected MCA branches, but this can be overcome with strategic ROI placement. However, even with prudent ROI placement, it was very difficult to place additional ROIs beyond the distal M2 segment of the MCA without encountering overlap with the unoccluded ACA or Posterior Cerebral Artery branches and the transverse sinus vein. These overlapping vessels could contribute to misleading values in the kinetic features, leading to poorer separation. The use of 4D (3D in space plus time) X-ray DSA would remove this overlap problem and allow 3D ROIs to be placed medial to the M2 segments, potentially leading to better separation between the three p_c subpopulations. Another approach would be to use Fuzzy C-means segmentation in a manner similar to Chapter 3 to identify vessels from the unoccluded ACA and Posterior Cerebral Artery territories.

4.5 Conclusion

We have devised a computerized feature-based method to measure the degree of pial arterial supply in acute ischemic stroke and compared its performance against a clinical pial grading system. It was found that exponential response parameters β of kinetic features extracted from the ischemic region could distinguish patients that had patently poor PAS from those that had patently good or borderline PAS. One limitation of this method is the difficulty in distinguishing between patients best-suited for reperfusion treatment from those with borderline suitability. Therefore, this method could potentially serve as an effective and efficient clinical technique for contraindicating reperfusion treatment, thereby sparing patients who are worst suited to it.

CHAPTER 5

KINETIC FEATURE PERFORMANCE FROM FCM-SEGMENTED VESSELS

5.1 Background

In Chapter 4, it was demonstrated that kinetic features extracted from pixel curves averaged over ROIs immediately preceding and within the ischemic territory can estimate PAS and allow for detection of drastic changes in the patient's suitability to for treatment. However, in the clinic, interventionists frequently use the observed extent of retrograde filling of the arteries [11] or the observed extent of parenchymal blush due capillaries in X-ray DSA image series [1]. The existence of contrast opacification in parenchyma is important because it is a direct indicator of the viability of neural tissue. The extent of contrast opacification of arteries can provide this information as well because contrast filling in the parenchyma is dependent on nearby arterial branches to supply it. A way to quantitate the extent of arterial or capillary opacification due to contrast would be to extract kinetic features from arteries or parenchyma in each ROI. To accomplish this, it is necessary to segment the arteries or parenchymal blush due to capillaries from all other vessel types. Therefore, in this chapter, first, a Fuzzy C-Means (FCM) based approach to segmenting arteries from non-arteries in X-ray DSA was developed. Kinetic features were then extracted from curves generated using the segmented arteries, and their performance in the task of characterizing PAS was evaluated. Since it has been shown in Chapter 3 that FCM can robustly separate major vessels from capillary blush, kinetic features were extracted from segmented blush and their performance in the task of characterizing PAS was evaluated. The performances of features extracted from curves generated using these FCM-segmented vessel classes were compared to features extracted from curves generated using all the pixels in each ROI. It is hypothesized that kinetic features extract from curves derived from FCM-segmented arteries and curves derived from FCM-segmented parenchymal blush in circular ROIs (see Section

4.2.2) will better quantitate PAS than features extracted from curves derived from all pixels in the circular ROIs.

5.2 Methods

Though the contrast curves for major arteries and veins are distinguishable from those for parenchymal blush due to capillaries (see Chapter 3), there are differences in contrast curves between arteries and veins as well. Delay-and-dispersion is the underlying mechanism behind this difference. Since contrast curves and therefore kinetic features can be extracted from individual pixels in X-ray DSA series, it is expected that pixels located in veins will have higher values for timing features (AAT, $eMTT$) lower UR, lower $A_D, Uptke$, lower ABF, and (because veins are larger than arteries), lower A_D. Therefore, if kinetic features are calculated at every pixel, feature maps (Figure 5.1) can be generated for each of them. These maps can be used along with the pixel curve data as inputs into FCM-clustering for the task of differentiating arteries from non-arteries.

5.2.1 Maps of Pixel-Wise Kinetic Features

For pixel coordinates (x, y) the pixel contrast curve $D_{x,y}(t)$ was extracted. To reduce the influence of noise, each $D_{x,y}(t)$ was fitted with a smoothing spline (smoothing parameter $p = 0.98981$). The smoothing spline (SS) was sampled at a rate of 1/6 Hz, so that all smoothed curves $D_{x,y,SS}(t)$ had the same "sampling rate" of 6 Fr/s. From $D_{x,y,SS}(t)$, the features $pAAT$, pUR, $peMTT$, pA_D, $pA_D, Uptke$, and $pABF$ are extracted and maps of these features (Figure 5.1) are generated. These features are defined in the analogous manner to AAT, UR, $eMTT$, A_D, $A_D, Uptke$, and ABF, respectively, except that $\overline{D}_{r,SS}(t)$ is replaced by $D_{x,y,SS}(t)$.

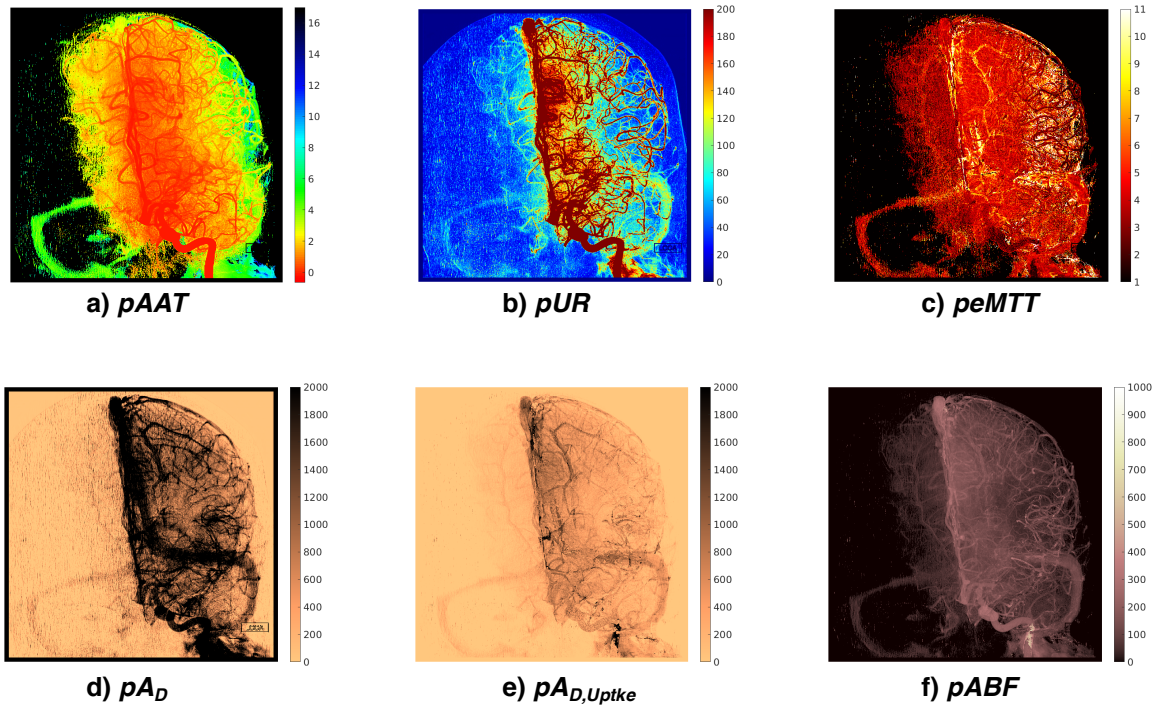

Figure 5.1: Pixel-wise feature maps to be investigated as inputs to FCM segmentation of arteries from non-arteries. Feature descriptions can be found in Section 4.2.3.

5.2.2 Segmentation of Vessel and Capillary Curve Data

A binary mask is geneated to filter out non-vessel pixels in the angiogram and the corresponding feature maps (see Figure 5.2). For a pixel to be included to be in this vessel mask (i.e., to equal 1), its highest class membership score in FCM 1 must come from the vessel class (see Figures 5.3 and 3.3). The filtered angiogram will be referred to as the "vessel angiogram" $D_V(x, y, t)$. In a similar manner, the binary mask for parenchymal blush is generated as well and the resulting "capillary blush angiogram" is denoted $D_B(x, y, t)$, except that the highest membership score in FCM 1 can come from either the "blush" class or the "background class" (the lack of parenchymal filling is jsut as telling as the presence of parenchymal presence). $D_V(x, y, t)$ will be used as the input to FCM segmentation of arterial vessel (see Figure 5.3 and the Section 5.2.3), and both $D_V(x, y, t)$ and $D_B(x, y, t)$ will be used to extract ROI-derived kinetic features in a manner similar to Chapter 4 (Section 4.2.3).

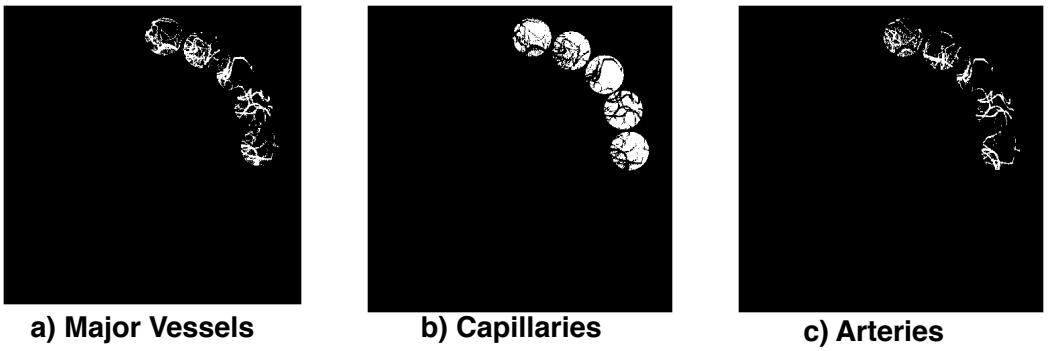

Figure 5.2: Binary Masks derived from FCM membership maps

5.2.3 Arterial Segmentation via FCM Clustering

FCM is used to segment arteries from arteries non-arteries in a manner very similar to segmenting major vessels from parenchymal blush due to capillaries under input protocol R_s (see Chapter 3), with the exception that kinetic features from $D_{x,y,SS}(t)$ are used along with curve data points as inputs in each ROI (Figure 5.3) and that the binary mask for major vessels is used to filter the angiogram and the kinetic feature maps prior to implementation of FCM clustering.

Because it is not currently known what set of features into FCM will best segment arteries from non-arteries, the sets of features outlined in Table 5.1 will be investigated. pA_D, pPK, $pA_D, Uptke$, and $pABF$ are included because of the relatively high performance of their $\overline{D}_{r,SS}(t)$-derived analogs in separating patients into separate p_c subpopulations (Chapter 4). $pAAT$, pUR,and $peMTT$ are chosen because they may be able to account for the effect dispersion between arteries and veins.

Feature-Set Index	**Curve Data Points**	$pAAT$	pUR	$peMTT$	pA_D	pPK	$pA_{D,Uptke}$	$pABF$
0	✓							
1	✓	✓	✓	✓				
2	✓				✓	✓	✓	✓
3	✓	✓	✓	✓	✓	✓	✓	✓

Table 5.1: Sets of kinetic features input to FCM for the task of distinguishing arterial pixels from non-arterial pixels.

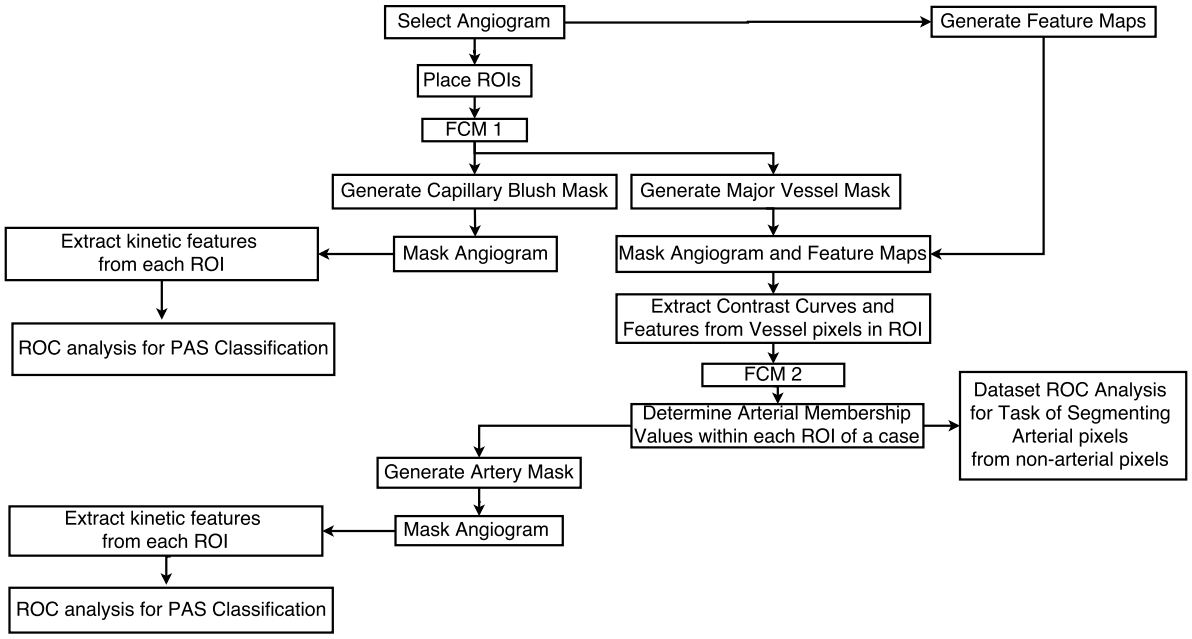

Figure 5.3: Flow-chart for the proposed cascaded FCM artery segmentation algorithm.

5.2.4 Evaluate the Performance of FCM Segmentation of Arteries from Non-Arteries

In this study, pixels in the kinetic ROIs were verified by a board-certified neuroradiologist (G.A.C.) as belonging to one of the following categories: (1) arteries with no overlapping veins, (2) veins with no overlapping arteries, (3) overlap between Arteries and veins, and (4) parenchymal blush due to residual capillaries in $D_V(x, y, t)$. These labeled pixels serve as clinical truth in evaluating the proposed FCM artery segmentation method.

For each category, 25-50 pixels were labelled in each ROI, although this number may be lower if the prevalence for a category in a particular ROI is small. Because arteries frequently overlap with veins in $D_V(x, y, t)$ the truth categories 1 and 2 were combined "arteries" truth category. To evaluate FCM's performance in separating arteries from non-arteries, categories 3 and 4 were combined into a "non-arteries" truth category. Using the truth for arteries and non-arteries, the task of separating arteries from non-arteries was assessed using ROC analysis. The truth is used within each ROI, across all cases of a given frame-rate is grouped to generate frame-rate-based curves (i.e., one ROC curve each for

Datasets A and B; see Table 2.2), and finally across all cases to yield an ROC curve for the entire dataset (i.e., Dataset A+B). Because category membership values always fall in the range [0 1], this pooling scheme allows performance to be summarized for each ROI, each frame-rate subset, and/or the entire dataset.

ROC curves were fitted using the proper binormal ROC model [40] software package and the non-parametric Wilcoxon area under the ROC curve (AUC) was chosen as the performance metric for this task.

The two sided 95% confidence interval of each AUC is estimated using bootstrapping. In this method, the arterial category membership values for the arterial and non-arterial categories were stored in a single dataset. 1000 bootstrap samples were selected from the arterial and non-arterial categories and AUC was calculated for each sample. The two sided 95% confidence interval was then calculated from these 1000 AUC's.

Using Dataset A+B (Table 2.2), performance comparisons for effect of different choices of the number of categories $N_{c,Art}$ and different Feature Set inputs to FCM were determined by evaluating the differences in AUC (ΔAUC). Using Datasets A, A_3, and A_M, (Table 2.2), performance comparisons for different frame-rates were determined by evaluating the differences in AUC (ΔAUC) as well. The differences in AUC for these 3 kinds of comparisons was assessed using bootstrapping (3000 iterations) and two-sided 95% confidence intervals of ΔAUC for superiority testing. If superiority testing was inconclusive, one-sided 90% confidence intervals of ΔAUC were calculated for non-inferiority testing. Non-inferiority was reached if the lower limit of the confidence interval was larger than -0.02 [20].

5.2.5 Extract Selected Kinetic Features from Segmented Classes

Within each case in Dataset A+B (see Table 2.2), a binary mask is geneated to filter out non-arterial pixels in the angiogram and the corresponding feature maps (see Figure 5.2). For a pixel to be included to be in this arterial mask (i.e., to equal 1), its highest class membership score in FCM 2 (see Figures 5.3) must come from the artery class. The resulting mask

was used to filter out non-arterial pixels in $D(x, y, t)$, resulting the "arterial angiogram" $D_A(x, y, t)$. We refer to the capillary and arterial angiograms $D_B(x, y, t)$ and $D_A(x, y, t)$ as filtered angiograms. If we denote a vascular category (e.g., arteries, capillaries) with τ, then $D_\tau(x, y, t)$ serves as a general notation for the filtered angiograms. The ROIs that were delineated in Chapters 3 and 4 are used for each $D_\tau(x, y, t)$ as well. In each ROI, a mean curve $\overline{D}_\tau(t)$ was calculated by averaging all unfiltered pixel values within an ROI at each image frame (i.e., time):

$$\overline{D}_{\tau,r}(t) = \frac{\sum_{x,y \text{ in ROI}} D(x, y, t)}{N}, \tag{5.1}$$

where N is the number of pixels in within an ROI. Thus, over the database of 24 cases, 128 contrast-time curves were calculated. To reduce the influence of residual noise and small-scale oscillatory motion due to breathing and pulsation, each $\overline{D}_{\tau,r}(t)$ was fitted with a smoothing spline (smoothing parameter p=0.98981).The smoothing spline (SS) was sampled at a rate of 1/6 Hz, so that all smoothed curves $\overline{D}_{\tau,r,SS}(t)$ had the same "sampling rate of 6 Fr/s.

For each category τ (i.e., capillary blush, arteries) set of computer-extracted kinetic features was extracted from each $\overline{D}_{\tau,r,SS}(t)$ to assess the degree of PAS. Because they exhibited superior stability after temporal downsampling, reproducibility, and performance in separating patients into p_c subpopulations in Chapter 4, the features extracted were A_D, PK, $A_D, Uptke$, and ABF. Their definitions are the same here as in Chapter 4, except that $\overline{D}_{r,SS}(t)$ is replaced by $\overline{D}_{\tau,r,SS}(t)$.

5.2.6 Exponential Response of Kinetic Features

For each category τ, the values of each kinetic feature F_τ change across the 5-6 ROIs. As in Chapter 4, it is hypothesized that the magnitude of this response can be used to classify a patient's suitability for reperfusion treatment. Therefore, for every τ, we apply the fitting

procedure described in Section 4.2.7 of Chapter 4 to the features F_τ. In a manner similar to Eq. 4.9, the normalized feature values $F_{\tau,Norm}(r)$ were fitted according to the following equation:

$$F_{\tau,Norm}(r) = e^{\beta(r-1)} \tag{5.2}$$

where r is the ROI index defined according to Figure 4.1, β is the parameter of exponential response for the particular feature F, and $F_{\tau,Norm}$ is the normalized feature value. The fitting was done using the Levenberg-Marquardt algorithm [30, 32]. To harmonize the dataset, the 6 Fr/s angiograms were down-sampled to create synthetic angiograms with temporal sampling according to the mixed frame-rate acquisition protocol (see Section 2). The value of β between the 6 Fr/s angiograms and the downsampled mixed frame-rate angiograms were then compared to determine if lowering the acquisition frame-rate affected performance. The goodness-of-fit R^2 and the root-mean-square error (RMSE) were calculated for each case.

5.2.7 Classification-Performance Evaluation

In Dataset A+B (see Table 2.2), the potential usefulness of each kinetic feature was determined by its ability to separate patients into two different PAS subpopulations (Table 4.5).Task I was the separation of PAS grade p_c = 1–2 (considered favorable PAS) vs p_c = 3–5 (considered poorer PAS); Task II was the separation of PAS grade p_c = 1–3 (for which treatment was feasible) vs p_c = 4–5 (for which treatment was to be avoided). The first, the Dataset A (see Table 2.2), is composed only of angiograms acquired at 6 Fr/s. Dataset A_d consists of angiograms downsampled from Dataset A to the mixed frame-rate protocol. Finally, Dataset B (see Table 2.2) consists of the angiograms in the downsampled subset and the angiograms from cases imaged under the mixed frame-rate protocol. For each dataset, the potential usefulness of each kinetic feature was determined by its ability to separate patients into two different PAS subpopulations (Table 4.5). Task I was the separation of PAS grades p_c = 1–2 (considered favorable PAS) vs p_c = 3–5 (considered poorer PAS); Task

II was the separation of PAS grades $p_c = 1$–3 (for which treatment was feasible) vs $p_c = 4$–5 (for which treatment was to be avoided). Box plots are generated for the distribution of each feature F_τ with subpopulations with $p_c = 1$–2, $p_c = 3$, and $p_c = 4$–5. For each feature F and each vascular category τ, box plots are generated for the distribution of each feature F_τ within the p_c subpopulations. For each F_τ derived from and each task performed on Database B, an ROC curve was generated by sweeping a threshold β_{TH} across the subpopulations' distributions of β and then measuring the True Positive and False Positive Fractions at each choice of β_{TH}. The Wilcoxon area under the ROC curve AUC [3, 40] was used as the performance metric in distinguishing between the two PAS subpopulations.

Task	**PAS subpopulation 1**	**PAS subpopulation 2**
I	$p_c = 1$–2	$p_c = 3$–5
II	$p_c = 1$–3	$p_c = 4$–5

Table 5.2: Two separation task for PAS-subpopulations. The difference between tasks hinged on whether patients with a borderline PAS score ($p_c = 3$) were considered suitable for reperfusion treatment.

5.3 Results

5.3.1 Evaluation of FCM Segmentation of Arteries

Effect of Input Feature-Set

In this subsection the number of clusters was $N_{c,Art} = 3$. In Figure 5.4a and Table 5.3, using Feature Set 1 as the input data to FCM gave the highest AUC in the task of separating arteries from non-arteries across Dataset A+B. The bootstrapped 95% confidence interval of the difference ΔAUC between Feature Set 1 and Feature Set 0 (i.e., curve data points alone) is above zero, indicating superior performance across Dataset A+B. The superior performance of Feature Set 1 over all other feature-sets investigated in this chapter holds within Datasets A and B as well (i.e., within frame-rates; see Table 2.2, Figure 5.4b, and

Table 5.4). In Figure 5.5, it can be seen that in Database A+B, except for 3 cases, the mean ROI AUC for Feature Set 1 are consistently high than for the other Feature Sets.

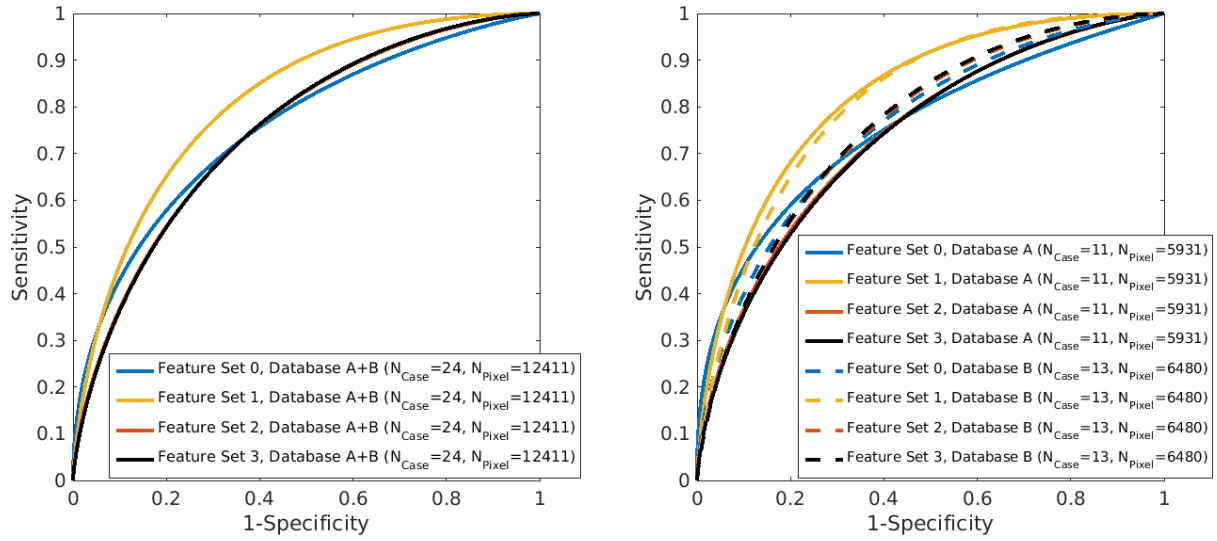

(a) (b)

Figure 5.4: Fitted binormal ROC curves for the performance in separating arterial pixels from non-arterial pixels for each input feature-set (see Table 5.1) for (a) Dataset A+B (Table 2.2) and (b) Datasets A and B (i.e., the different Frame-rates). The truth for the entire database includes all pixels across all cases; the truth for ROCs from Datasets A and B include all pixels across all cases acquired at 6Fr/s and the Mixed Frame-rate protocol, respectively. The inputs protocol to FCM was R_s.

Effect of Number of FCM Classes $N_{c,Art}$

In this subsection, Feature Set 1 (curve data points, pUR, $pAAT$, $peMTT$) was used as the input data to FCM. In Figure 5.6a and Table 5.5, segmentation of arteries from non-arteries in Dataset A+B using $N_{c,Art} = 3$ gives slightly better performance over FCM using $N_{c,Art} = 2$ or $N_{c,Art} = 4$. However, the bootstrapped 95% confidence intervals for ΔAUC indicate that only the difference in performance between $N_{c,Art} = 3$ and $N_{c,Art} = 4$ is statistically significant. For Dataset A (Figure 5.6b and Table 5.6), the ΔAUC for $N_{c,Art} = 3$ is significantly better than for $N_{c,Art} = 2$ or $N_{c,Art} = 4$, but as in Table 5.5, the improvement is minimal. For Dataset B, there are no statistically significant differences in performance

Input Feature -Set Indices	**AUC**	**95% Confidence Interval of ΔAUC**	**p-Value** ($\alpha = \mathbf{0.017}$)
0	0.77 [0.76; 0.78]	—	—
1	0.82 [0.81; 0.82]	[-0.036; -0.059]	< 0.0001*
2	0.76 [0.75; 0.77]	[-0.020; 0.004]	0.88
3	0.76 [0.75; 0.77]	[-0.020; 0.0-4]	0.90

Table 5.3: Database ROC statistics for Fig. 3.8a, with 95% confidence intervals in brackets (using Database A+B, 24 cases; See Table 2.2). The significance level is adjusted $\alpha = 0.017$ using a Holm correction. Feature Set 1 is the only set that shows statistically significant improvement over Feature Set 0.

Frame-Rate	**Input Feature-Set Indices**	**AUC**	**95% Confidence Interval of ΔAUC**	**p-Value** ($\alpha = \mathbf{0.0083}$)
6 (Dataset A)	0	0.76 [0.75; 0.78]	—	—
	1	0.83 [0.82; 0.84]	[0.047; 0.080]	$< 0.0001*$
	2	0.75 [0.74; 0.76]	[−0.004; 0.031]	0.93
	3	0.75 [0.73; 0.76]	[−0.037; 0.011]	0.98
Mixed (Dataset B)	0	0.77 [0.76; 0.78]	—	—
	1	0.82 [0.81; 0.83]	[0.032; 0.063]	$< 0.0001*$
	2	0.77 [0.76; 0.78]	[−0.019; 0.015]	0.60
	3	0.77 [0.76; 0.78]	[−0.017; 0.016]	0.48

Table 5.4: Frame-rate ROC statistics for Fig. 3.8b. The superior performance is consistent across both frame-rates for $N_c = 3$. The significance level is adjusted $\alpha = 0.008$ using a Holm correction. The asterisk (*) indicates statistical significance. Feature Set 1 is the only set that shows statistically significant improvement over Feature Set 0.

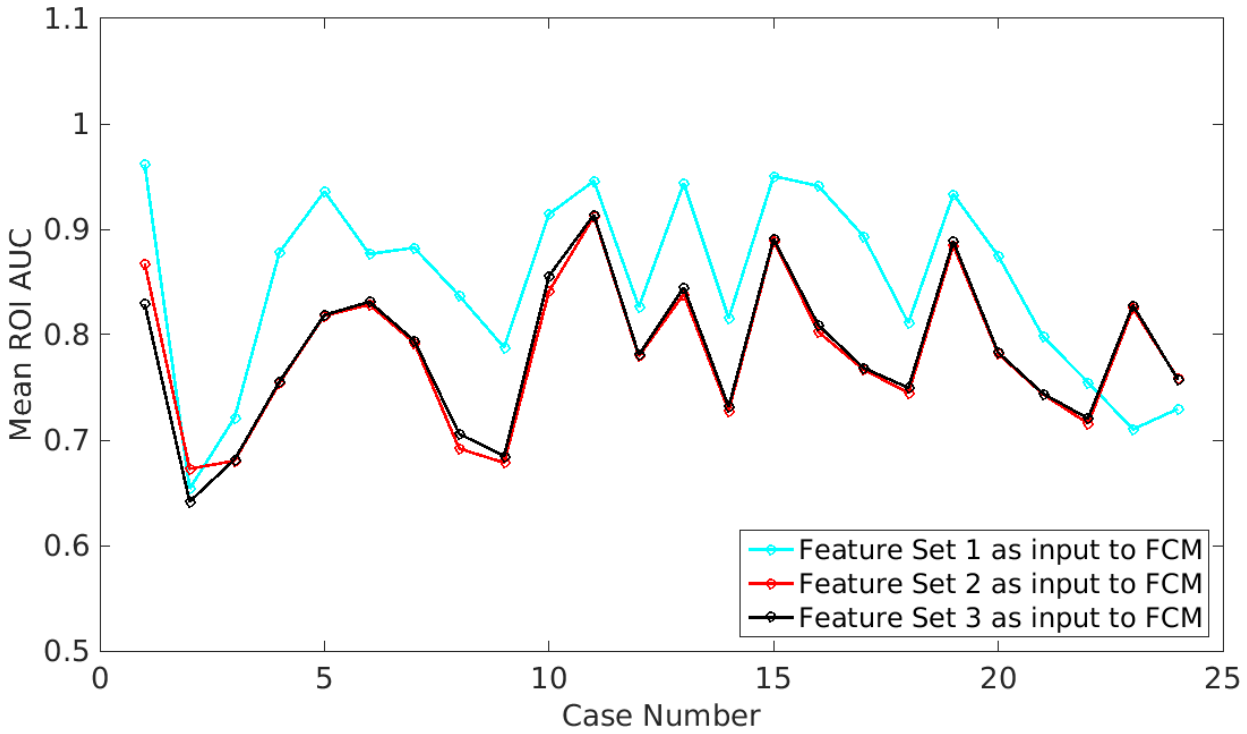

Figure 5.5: Mean ROI AUC for each case (Datset A+B; see Table 2.2). For 21 of the 24 cases, Set 1 has the best performance in the task of identifying arteries from non-arteries.

between the 3 choices of $N_{c,Art}$. The similarity in the 3 choices of $N_{c,Art}$ are further reflected by the mean ROI AUC in each case in Dataset A+B (Figure 5.7).

Effect of Frame-Rate

As shown in Figure 5.8, when using Feature Set 1 (Table 5.1) and $N_{c,Art} = 3$, there is a small (< 0.03) but visually discernible difference in AUC between Datasets A and A_M. This difference is statistically significant (see Table 5.7), indicating that imaging at mixed frame-rate protocol gives a better performance over a uniform 6 Fr/s acquisition. However, the ROC curves, AUC, and 95% confidence intervals Datasets A and A_3 are almost equivalent and the bootstrapped comparison between these two frame-rates passes the non-inferiority test, indicating that FCM segmentation of arteries from non-arteries for 6 Fr/s acquisitions is as good as FCM segmentation of arteries from non-arteries for 3 Fr/s acquisitions.

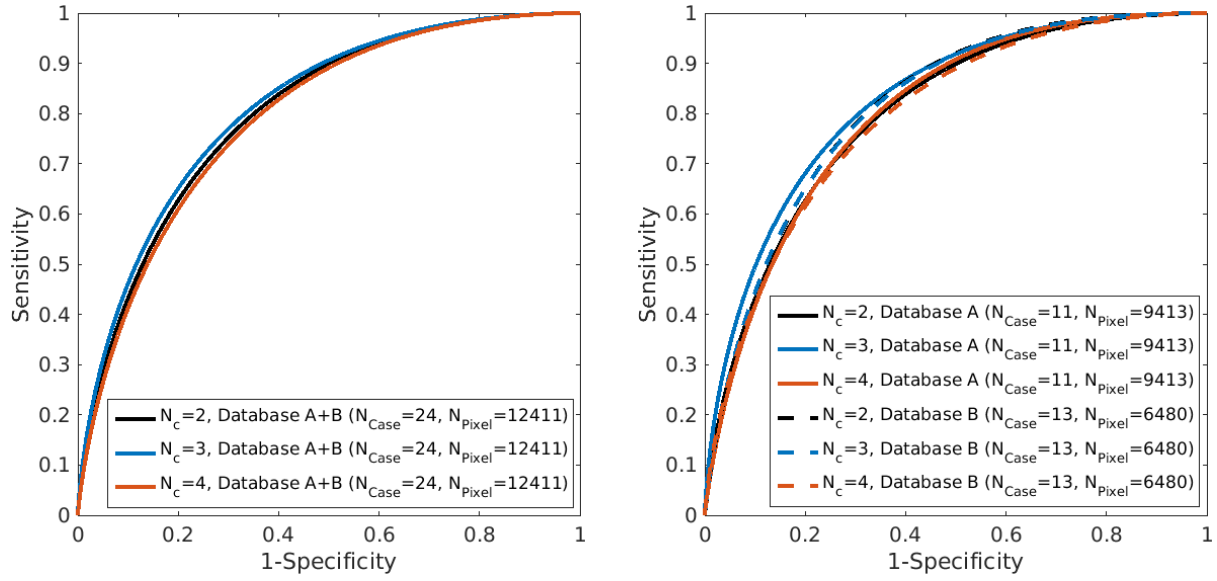

Figure 5.6: Fitted binormal ROC curves for the performance in separating arteries from non-arteries for number of classes $N_{c,Art} = 2$–4. The ROC curves span (a) Dataset A+B (Table 2.2) and (b) Datasets A and B (i.e., the different Frame-rates). The truth for Dataset A+B includes all pixels across all cases; the truth ROCs from Datasets A and B include all pixels across all cases acquired at 6 Fr/s and the Mixed Frame-rate protocol, respectively. The inputs protocol to FCM was R_s.

Number of Categories $N_{c,Art}$	AUC_{Wil}	**95% Confidence Interval for ΔAUC (p-Value)**	
2	0.81 [0.80; 0.81]	[0.006; 0.358] (0.004)*	[-0.019; 0.013] (0.66)
3	0.82 [0.81; 0.82]		
4	0.80 [0.79; 0.81]	[0.003; 0.033] (0.014)*	

Table 5.5: Database ROC statistics for Figure 5.6a with 95% confidence intervals in brackets. The significance level was adjusted to $\alpha = 0.017$ using a Holm correction. The asterisk (*) indicates statistical significance.

Frame-Rate	Number of Categories $N_{c,Art}$	AUC_{Wil}	95% Confidence Interval for ΔAUC (p-Value)	
6 (Dataset A)	2	0.81 [0.80; 0.82]	[0.004; 0.035] (0.008)*	[-0.020; 0.013] (0.64)
	3	0.83 [0.82; 0.84]		
	4	0.81 [0.80; 0.82]	[0.002; 0.033] (0.012)*	
Mixed (Dataset B)	2	0.82 [0.81; 0.83]	[-0.013; 0.016] (0.44)	[-7.87× 10^{-4}; 0.030] (0.032)
	3	0.82 [0.81; 0.83]		
	4	0.80 [0.79; 0.81]	[-2.4 × 10^{-4}; 0.031] (0.026)	

Table 5.6: Frame-rate ROC statistics for Figure 5.6b with 95% confidence intervals in brackets. The significance level was adjusted to $\alpha = 0.008$ using a Holm correction.The asterisk (*) indicates statistical significance.

Frame-rate Comparison	ΔAUC	Two-sided 95% Confidence Interval	One-sided 90% Confidence Interval
Dataset A vs Dataset A_3	-0.002	$[-0.017; 0.0124]$ (0.024)	$[-0.012; 1.000]$ $(0.012)*$
Dataset A_M vs Dataset A	0.026	$[0.012; 0.041]$ $(< 0.001)*$	$[0.017; 1.000]$ $(< 0.001)*$
Dataset A_M vs Dataset A_3	0.024	$[0.011; 0.004]$ $(< 0.001)*$	$[-0.003; 1.000]$ $(< 0.001)*$

Table 5.7: Pairwise bootstrapped difference in AUC between frame-rates with confidence intervals (brackets) and significance values (parentheses). The significance level was adjusted to $\alpha = 0.017$ using a Holm correction. The asterisk (*) indicates statistical significance.

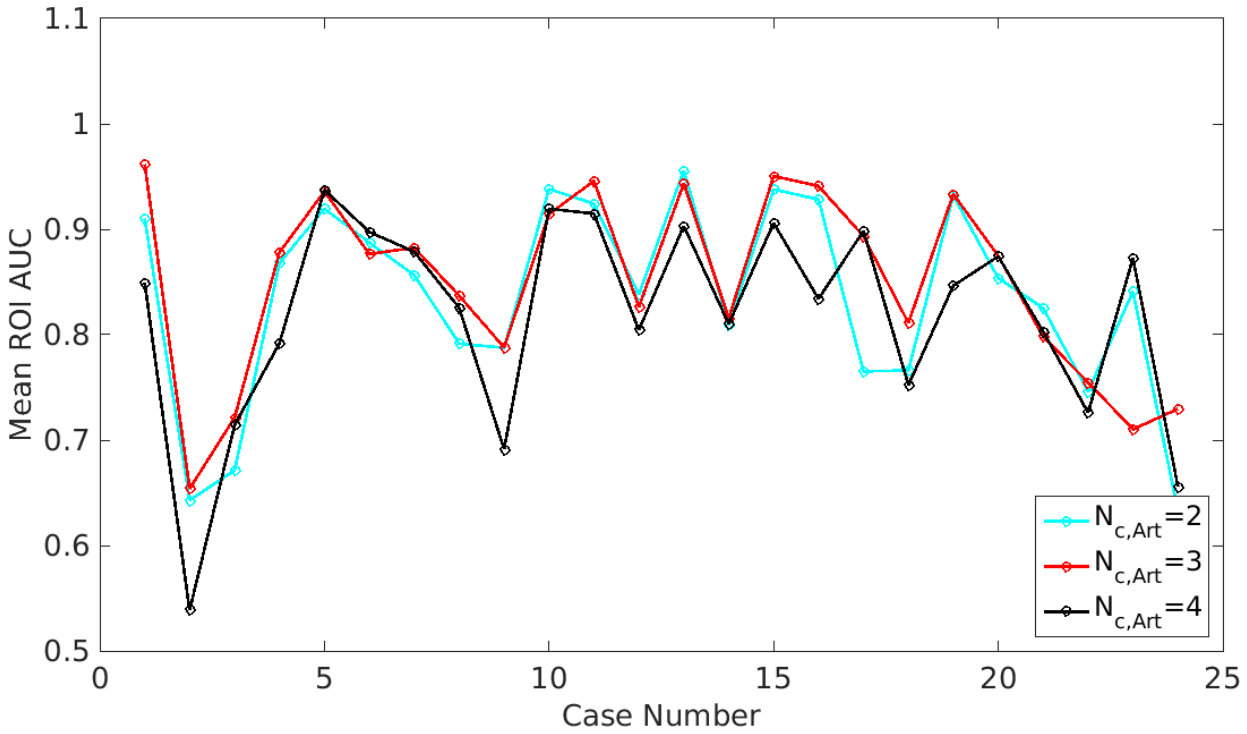

Figure 5.7: Mean ROI *AUC* for each case (Datset A+B; see Table 2.2). For only 11 of the 24 cases, $N_{c,Art} = 3$ has better performance than $N_{c,Art} = 2$ or $N_{c,Art} = 4$ in the task of identifying arteries from non-arteries.

5.3.2 Patient Classification Using Kinetic Features

Exponential Response of Kinetic Features

In Figure 5.9, A_D separates $p_c = 4$–5 from $p_c = 1$–3 within Dataset A+B with the least overlap for all pixels, arterial pixels, and capillary pixels. However, for each feature (particularly PK and $A_{D,Uptke}$), a clear pattern as a function of p_c can be seen for each subpopulation's median value. Though there is overlap between $p_c = 1$–2 and $p_c = 3$ for all features extracted from FCM-segmented arteries, FCM-segmented parenchymal blush, and all pixels in the ROIs in Dataset A+B, the β values are confined to lower values for features extracted from the capillary pixels.

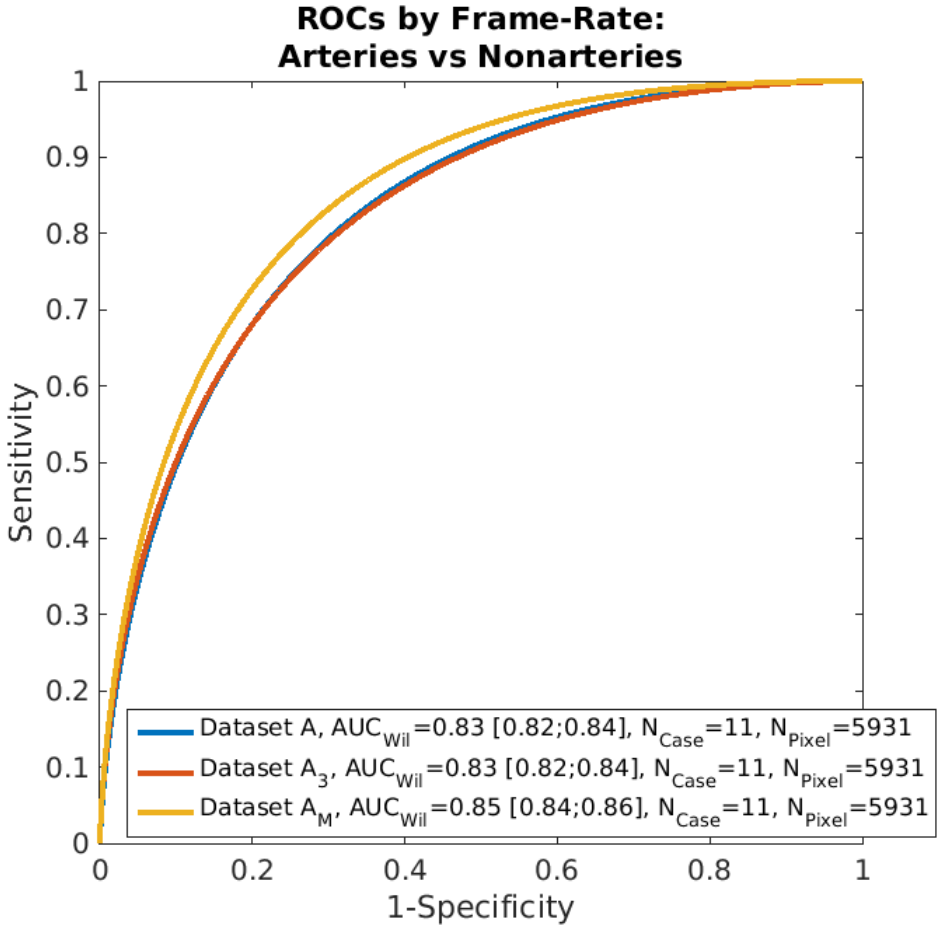

Figure 5.8: Fitted binormal ROC curves for each frame-rate subset ($N_{c,Art} = 3$ and input protocol R_s). Area under the curve AUC is reported in the legend with the 95% confidence intervals in parentheses.

Feature	$\mathbf{R^2}$	**RMSE**	**AUC for Task I: $\mathbf{p_c = 1}$–$\mathbf{2}$ vs $\mathbf{p_c = 3}$–$\mathbf{5}$**	**AUC for Task II: $\mathbf{p_c = 1}$–$\mathbf{3}$ vs $\mathbf{p_c = 4}$–$\mathbf{5}$**
A_D	0.74 ± 0.34	0.09 ± 0.05	0.81 ± 0.10	$1.00 \pm 0.00*$
PK	0.86 ± 0.15	0.08 ± 0.04	0.84 ± 0.09	0.99 ± 0.02
$A_{D,Uptke}$	0.63 ± 0.44	0.15 ± 0.09	0.84 ± 0.08	0.94 ± 0.06
ABF	0.84 ± 0.17	0.09 ± 0.05	0.80 ± 0.10	0.98 ± 0.03

Table 5.8: Fit and Evaluation statistics for kinetic features extracted from mean curves averaged across all pixels each in ROI in Dataset A+B (see Table 2.2). *Results of AUC = 1 are likely due to small patient sample size

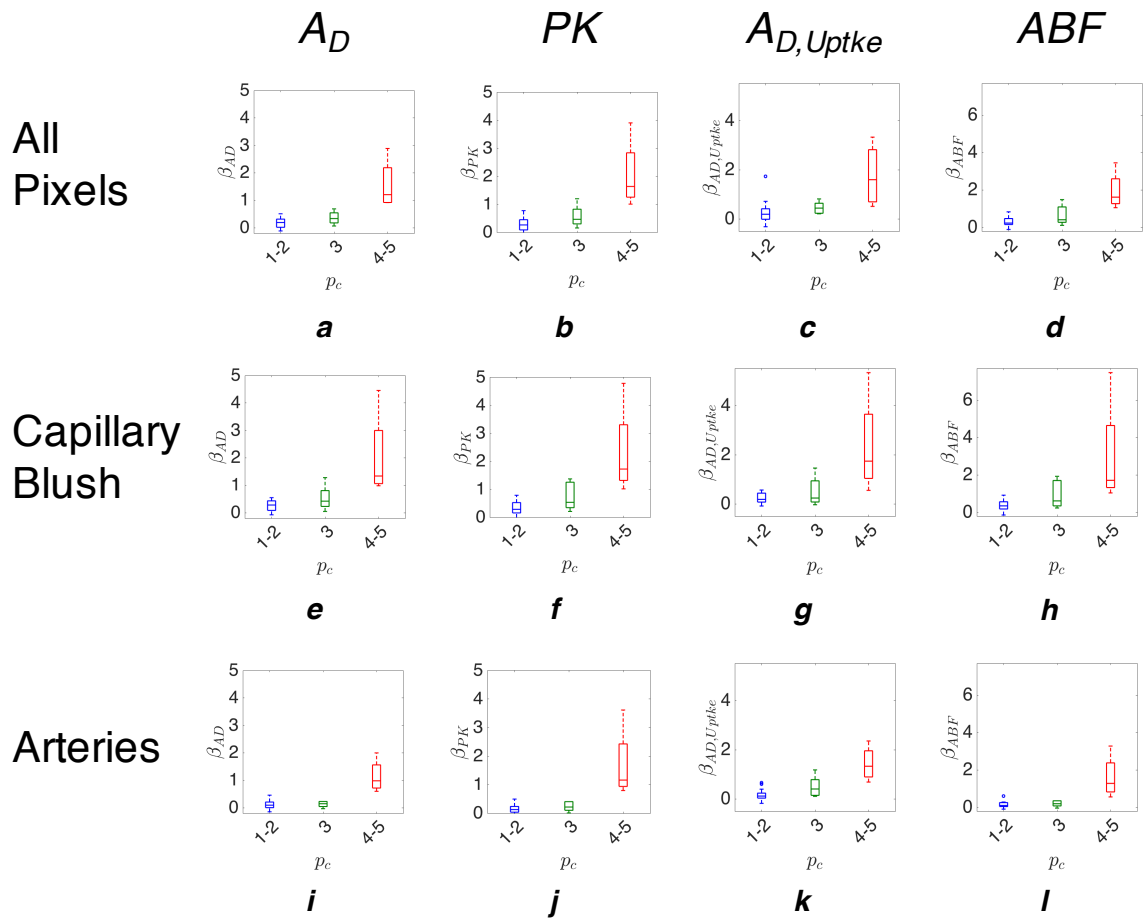

Figure 5.9: Box plot comparisons of extracted kinetic features from Dataset A+B for classifying patients according to pial grade p_c. A trend of steadily increasing median feature values for β is especially observable for FCM-segmented parenchymal blush.

Feature	**R^2**	**RMSE**	**AUC for Task I: $p_c = 1$–2 vs $p_c = 3$–5**	**AUC for Task II: $p_c = 1$–3 vs $p_c = 4$–5**
A_D	0.57 ± 0.37	0.1 ± 0.04	0.75 ± 0.11	0.96 ± 0.04
PK	0.62 ± 0.33	0.1 ± 0.04	0.77 ± 0.11	0.96 ± 0.04
$A_{D,Uptke}$	0.6 ± 0.37	0.16 ± 0.1	0.87 ± 0.07	0.96 ± 0.04
ABF	0.61 ± 0.32	0.11 ± 0.05	0.77 ± 0.11	0.95 ± 0.04

Table 5.9: Fit and Evaluation statistics for kinetic features extracted from averaged across FCM-segmented arterial curves each in ROI in Dataset A+B (see Table 2.2).

Feature	R^2	RMSE	AUC for Task I: $p_c = 1$–2 vs $p_c = 3$–5	AUC for Task II: $p_c = 1$–3 vs $p_c = 4$–5
A_D	0.78 ± 0.36	0.09 ± 0.05	0.81 ± 0.11	0.98 ± 0.03
PK	0.88 ± 0.18	0.08 ± 0.04	0.85 ± 0.08	0.98 ± 0.03
$A_{D,Uptke}$	0.57 ± 0.44	0.15 ± 0.09	0.74 ± 0.12	0.96 ± 0.04
ABF	0.89 ± 0.22	0.07 ± 0.04	0.85 ± 0.08	0.94 ± 0.05

Table 5.10: Fit and Evaluation statistics for kinetic features extracted from averaged across FCM-segmented capillary curves each in ROI in Dataset A+B (see Table 2.2).

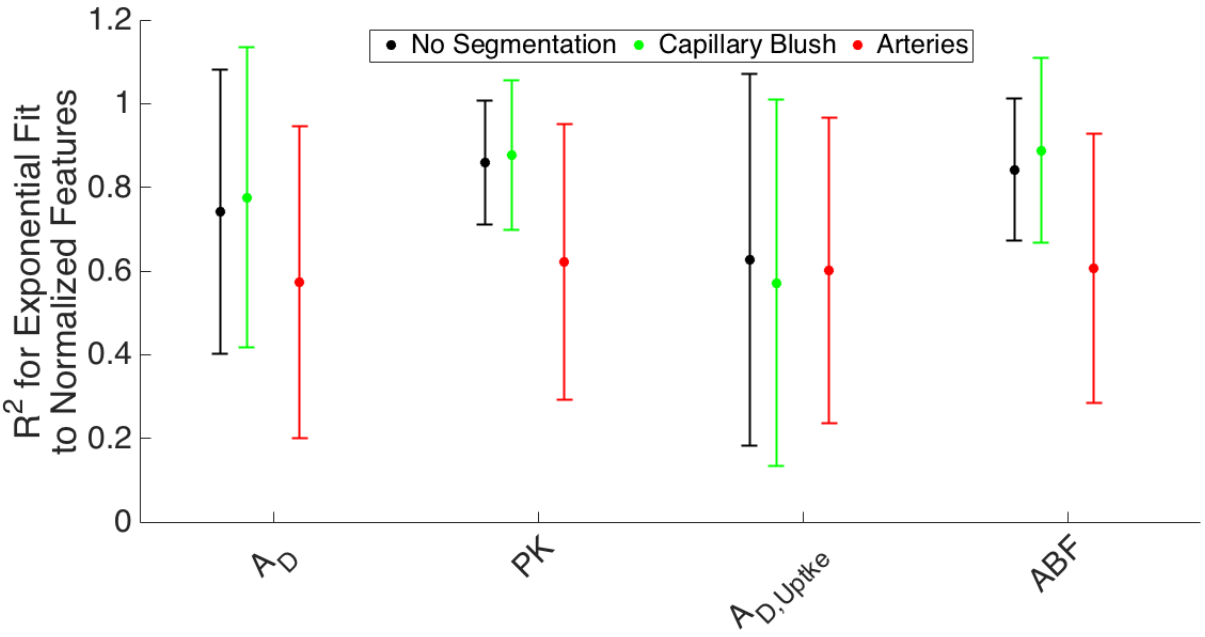

Figure 5.10: R^2 goodness of fit measure for each feature's exponential fit. Kinetic features are extracted within the listed vascular categories listed in the legend and come from Dataset A+B (see Table 2.2).

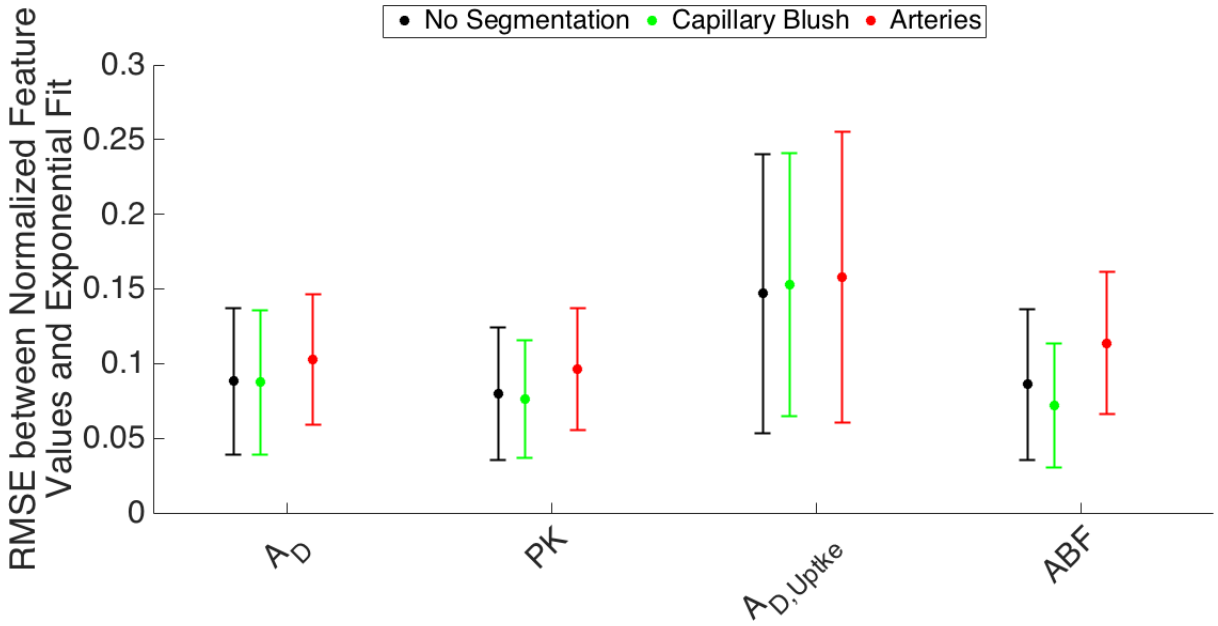

Figure 5.11: $RMSE$ for each the normalized kinetic features and their respective exponential fits. Kinetic features are extracted within the listed vascular categories listed in the legend and come from Dataset A+B (see Table 2.2).

Classification-Performance Evaluation

For Task I (Figure 5.12 and Tables 5.8, 5.9, and 5.10), A_D, PK, and ABF extracted from FCM-segmented arterial curves tended to have lower AUC than the features extracted from all pixel curves in each ROI. By contrast, A_D, PK, and ABF extracted from FCM-segmented capillary curves tended to have higher AUC for Task I than A_D, PK, and ABF extracted from all pixels curves in each ROI. In fact, PK and ABF extracted from FCM-segmented capillary curves had the highest AUCs for Task I. It is worth noting that for Task I, A_D extracted from FCM-segmented artery curves had the smallest AUC ($AUC = 0.73 \pm 0.11$).

In Task II and for every vascular category, all features had $AUC > 0.90$; in particular, A_D, PK, and ABF had $AUC > 0.95$. Interestingly, for FCM-segmented arterial curves $A_{D,Uptke}$ had the best performance.

In both tasks and for each feature, the error bars for the vascular category's AUC all overlap.

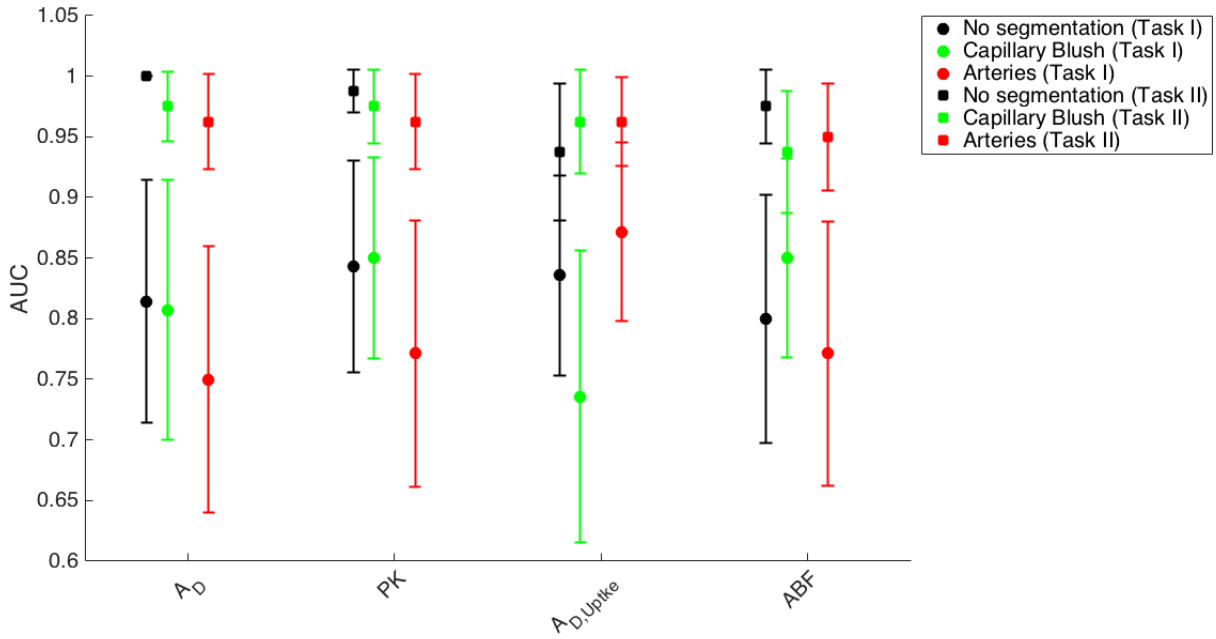

Figure 5.12: Wilcoxon AUC values for Tasks I and II using the extracted kinetic features. Kinetic features are extracted within the listed vascular categories listed in the legend and come from Dataset A+B (see Table 2.2). PK and ABF have preferable performance.

5.4 Discussion

5.4.1 FCM Segmentation of Arterial Pixels from Non-arterial Pixels

For pixels in major vessels, if curve data is used to segment arterial pixels from non-arterial pixels, the performance is drastically reduced when compared to the task of segmenting vessels from non-vessels (AUC=0.77 vs AUC=0.86; see Chapter 3). Because MCA branches affected by PAS have relative to normally-supplied arterial branches, reduced contrast filling, and they frequently overlap with veins on 2D angiograms, the contrast curves for arteries and veins are more similar to one another than they are to non-vessel pixels. It is for this reason that pA_D, pPK, and $pA_{D,Uptke}$ do not significantly improve performance for segmenting arteries from non-arteries.

However, in a given ROI, arteries always arrive before veins and are less dispersed than them. They, therefore, have shorter $pAAT$, shorter $peMTT$, and larger pUR. Therefore, using these 3 features and the pixel curve data improves arterial segmentation over using

pixel curve data alone. However, if pA_D, pPK, $pA_{D,Uptke}$, and $pABF$ are used alongside $pAAT$, $peMTT$, pUR, and pixel curve data, arterial segmentation does not improve compared with using pixel curve data alone. This means that even when "helpful" features (i.e., $pAAT$, $peMTT$, and pUR) are present in the input data to FCM Clustering , "non-helpful" features can still throttle any potential improvements in arterial segmentation. This implies that replicating $pAAT$, $peMTT$, and pUR for each pixel in the input data could improve performance. Another important implication from these comparisons is that dispersion between arteries and veins does not significantly affect pA_D, pPK, $pA_{D,Uptke}$, or $pABF$. Therefore, a direction for future research would be to verify these two implications.

For angiograms acquired at the mixed frame-rate protocol, the three choices for the number of input categories $N_{c,Art}$ ($N_{c,Art}$ = 2–4) do not lead to significant differences in AUC for the task of segmenting arteries from non-arteries. For angiograms acquired at 6 Fr/s (i.e., Dataset A), the bootstrapped 95% confidence interval for ΔAUC (see Table 5.6) was statistically significant, but $\Delta AUC = 0.02$ is considered too small to be of concern. Because arteries frequently overlap with veins in 2D X-ray angiograms, much of the pixel truth is overlap truth. As a result, arterial membership scores from this truth category likely dominate the calculation of the ROC curves and their Wilcoxon AUCs. Future work can address the contribution of overlap to ROC evaluation in the task of segmenting arteries from non-arteries by investigating different definitions arterial truth (i.e., designate a truth pixel as "arterial" if it is an artery and there is no venous overlap).

It is interesting to note from Figure 5.8 and Table 5.7 that for the angiograms downsampled to the mixed frame-rate protocol, a statistically significant improvement in performance is observed. This raises the possibility that steadily decreasing the sampling rate with time may actually help in identifying veins. Since this comparison is being made using Set 1, for future investigations there are two parts to investigating such a possibility. The first part would be to use Feature Set 0 (see Table 5.1) as the input to FCM segmentation of arteries for non-arteries and compare the performance between Datasets A and A_M in a manner

analogous to Subsection 5.3.1:*Effect of Frame-Rate*. Because downsampling may influence the pixel kinetic features, the second part would be to examine the differences in $pAAT$, $peMTT$, and pUR between Dataset A and Dataset A_M for the truth pixels. Such an investigation would explain the effect downsampling to the mixed frame-rate protocol would have on $pAAT$, $peMTT$, and pUR and what frame-rate is most conducive to segmenting arteries from non-arteries.

5.4.2 Patient Classification Using Kinetic Features

Of the 3 vascular categories (FCM-segmented arteries, FCM-segmented parenchymal blush, and all pixels in each ROI), using all pixels in each ROI tended to have the most robust performance for Tasks I and II and fit the exponential model best (Figures 5.10 and 5.11). It is worth noting, however, that for Task I, ABF had the highest AUC amongst features extracted from the FCM-segmented parenchymal blush while $A_{D,Uptke}$ extracted from the FCM-segmented arteries tended to have the best performance for the vascular category. Since $A_{D,Uptke}$ and ABF are surrogates for transit time and in arteries and perfusion in parenchyma, respectively, our results suggest that FCM segmentation for these 2 vascular categories, followed feature extraction, and classification using those features can quantitatively track patient physiology during intervention. The performance for Task II is comparable across features and vascular categories, which agrees with findings in Chapter 4. This indicates that patients with poor PAS are easy to identify.

However, for both Tasks I and II, across the 4 features, and across the 3 vascular categories, the error-bars overlap (see Figure 5.12), belying the small sample size (N=24) of our database. To verify these findings, a larger database is needed.

5.5 Conclusion

We have developed a cascaded FCM-based approach to segmenting arteries from non-arteries and parenchymal blush due to capillaries from major vessels. Kinetic features are extracted from FCM-segmented arterial curves and FCM-segmented capillary curves, and used to classify patients' suitability for reperfusion treatment. The results suggest that pixel-extracted AAT, $eMTT$, and UR are useful for characterizing the delay-and-dispersion effect while A_D,PK, and $A_{D,Uptke}$, and ABF are more suited towards patient classification. It is also suggested that the kinetic-feature extracted from FCM-segmented arterial curves and FCM-segmented blush curves can quantitatively track patient physiology. These results are comaprable to features extracted without any segmentation. However, the results in this chapter need to be verified with a larger database.

CHAPTER 6

DISCUSSION AND CONCLUSION

In this chapter, a discussion of the main contributions of this thesis and the conclusion are summarized. Limitations to this work are discussed and future work to overcome limitations and improve this field are suggested.

We have investigated a computational method to quantitatively estimate the arterial supply due to pial collaterals, or the pial arterial supply (PAS)—imaged using X-ray DSA—in the setting of acute ischemic stroke. Using an angiographic database, this method has been able to reliably contra-indicate reperfusion treatment for patients least to suited to it and, to a more limited degree, identify patients who have a borderline suitability for reperfusion treatment. Segmentation of major vessel branches is an important step to accurately quantifying the extent of PAS and automatically assessing patient candidacy for reperfusion treatment. Kinetic features extracted from one or more of these vessel classes can potentially allow for dynamic monitoring of intra-interventional changes in PAS which in turn can aid the interventionist in changing treatment decisions.

The main contributions of this thesis are as follows:

(1) An FCM-based method for automatically segmenting pial-supplied major vessels from parenchymal blush using X-ray DSA image series was developed. This method showed promising performance in identifying pixel vessels and shown to have robust performance at multiple clinical angiographic frame-rates.

(2) A quantitative, feature-based approach to assessing PAS based on the filling of iodinated contrast in X-ray DSA was developed and evaluated. It was found that the degree of exponential response for the investigated features could serve as an effective clinical technique for contra-indicating reperfusion treatment, thereby sparing patients who are poor candidates for it.

(3) A Fuzzy C-Means based-approach to automatically segment arteries from non-arteries was developed and evaluated. Kinetic features were subsequently extracted from curves

generated from segmented arteries and capillary blush, and their performance in the task of characterizing PAS was evaluated. The results suggested that kinetic curves and features extracted from pixel in X-ray angiograms could segment arteries from non-arteries while features extracted from pixel segmented arterial and capillary curves could provide a real-time quantitative marker for the patient's condition during intervention.

These results support the hypothesis that during acute ischemic stroke, computerized and quantitative angiographic analysis of pial arterial supply can identify patients' suitability for reperfusion treatment. Because timing and dynamic monitoring of the patient is crucial to effective treatment of stroke, this method can potentially serve as a fast "second-check" to an interventional radiologist's treatment decisions. Therefore, better treatments will be administered more quickly, which will salvage more neural tissue and potentially reduce long-term disability. However, for this approach to be ready for clinical use, important limitations must be overcome.

Throughout our study, our database consisted of 24 cases, 13 of which were imaged at a non-uniform frame-rate. Therefore, the investigations in this research must be followed up with a larger database. This database can be generated by gathering data either prospectively or retrospectively. Because stroke patients with visible PAS are uncommon at the University of Chicago Medical Center, acquiring angiographic data through cross-institution collaborations may be fruitful. It must be ensured that angiographic data is acquired, where clinically permissible, at a uniform 6 Fr/s, as this may lead to improved feature accuracy. Furthermore, an important inclusion criterion to the database should be the absence of motion artifacts.

For kinetic features used to classify a patient's suitability for reperfusion treatment, there is difficulty in distinguishing between patients best suited for reperfusion treatment from those who had borderline suitability. This is because 2D spatial projection images lead to overlap with unoccluded, normally perfused branches from other arterial territories and the transverse sinus vein, which makes additional ROI placement infeasible. The use of 4D DSA

(3D plus time) as proposed be *Davis et al, 2014* [14] would remove this overlap. Therefore, an interesting direction to take in future research would be an adaptation of the method discussed in this dissertation to 4D DSA series of acute ischemic stroke.

Since clinical exams are not controlled environments, their ability to verify physiological inferences is limited. Controlled simulation studies can and preclinical canine studies can address such a task. Under these studies, PAS can be directly compared to the infarct volume. Since A_D, $A_{D,Uptke}$, PK, and ABF are relatively straightforward to implement and show promising performance in Chapter 5, they may be compared to their intended surrogates on MRI to track stroke progression.

6.0.1 Conclusion

This research serves as the first step in achieving a fully computerized and quantitative means for personalizing patient management during interventional imaging for acute ischemic stroke. More specifically, this thesis represents a bridge between existing manual, quantitative methods in X-ray DSA imaging of stroke and a fully computerized, unsupervised, quantitative, and objective approach that is clinically reliable and efficient. The techniques presented in this thesis may find application in quantifying imaging of other neurovascular disease as well.

REFERENCES

[1] Firas Al-Ali, Thomas A Tomsick, John J Connors, James M Gebel, John J Elias, Georges Z Markarian, Zein Al-Ali, and Joseph P Broderick. Capillary index score in the interventional management of stroke trials i and ii. *Stroke*, 45(7):1999–2003, 2014.

[2] Gregory W Albers, Vincent N Thijs, Lawrence Wechsler, Stephanie Kemp, Gottfried Schlaug, Elaine Skalabrin, Roland Bammer, Wataru Kakuda, Maarten G Lansberg, Ashfaq Shuaib, et al. Magnetic resonance imaging profiles predict clinical response to early reperfusion: the diffusion and perfusion imaging evaluation for understanding stroke evolution (DEFUSE) study. *Annals of Neurology*, 60(5):508–517, 2006.

[3] Donald Bamber. The area above the ordinal dominance graph and the area below the receiver operating characteristic graph. *Journal of Mathematical Psychology*, 12(4):387–415, 1975.

[4] Oh Young Bang, Jeffrey L Saver, Brian H Buck, Jeffry R Alger, Sidney Starkman, Bruce Ovbiagele, Doojin Kim, Reza Jahan, Gary R Duckwiler, Sa Rah Yoon, et al. Impact of collateral flow on tissue fate in acute ischaemic stroke. *Journal of Neurology, Neurosurgery & Psychiatry*, 79(6):625–629, 2008.

[5] Oh Young Bang, Jeffrey L Saver, Suk Jae Kim, Gyeong-Moon Kim, Chin-Sang Chung, Bruce Ovbiagele, Kwang Ho Lee, and David S Liebeskind. Collateral flow predicts response to endovascular therapy for acute ischemic stroke. *Stroke*, pages STROKEAHA–110, 2011.

[6] Timothy J Carroll, Howard A Rowley, and Victor M Haughton. Automatic Calculation of the Arterial Input Function for Cerebral Perfusion Imaging with MR Imaging. *Radiology*, 227(2):593–600, 2003.

[7] Weijie Chen, Maryellen L Giger, and Ulrich Bick. A Fuzzy C-Means (FCM)-Based Approach For Computerized Segmentation Of Breast Lesions In Dynamic Contrast-Enhanced MR Images. *Academic Radiology*, 13(1):63–72, 2006.

[8] Benayoun M Theyel B Khan S Garg N Rink C Kontzialis M Sen C Christoforidis, G. Angiographically Derived Arterial Arrival Time as a Measure of Leptomeningeal Collateral Formation in Experimental Acute Stroke . Number eP-54. American Society of Neuroradiology, April 2012.

[9] GA Christoforidis, C Karakasis, Y Mohammad, LP Caragine, M Yang, and AP Slivka. Predictors of hemorrhage following intra-arterial thrombolysis for acute ischemic stroke: the role of pial collateral formation. *American Journal of Neuroradiology*, 30(1):165–170, 2009.

[10] GA Christoforidis, P Vakil, SA Ansari, FH Dehkordi, and TJ Carroll. Impact of pial collaterals on infarct growth rate in experimental acute ischemic stroke. *American Journal of Neuroradiology*, 38(2):270–275, 2017.

[11] Gregory A Christoforidis, Yousef Mohammad, Dimitris Kehagias, Bindu Avutu, and Andrew P Slivka. Angiographic assessment of pial collaterals as a prognostic indicator following intra-arterial thrombolysis for acute ischemic stroke. *American Journal of Neuroradiology*, 26(7):1789–1797, 2005.

[12] Gregory A Christoforidis, Cameron Rink, Marinos S Kontzialis, Yousef Mohammad, Regina M Koch, Amir M Abduljalil, Valerie K Bergdall, Sashwati Roy, Savita Khanna, Andrew P Slivka, et al. An endovascular canine middle cerebral artery occlusion model for the study of leptomeningeal collateral recruitment. *Investigative radiology*, 46(1):34, 2011.

[13] Peter Coyle and Pentti T Jokelainen. Dorsal cerebral arterial collaterals of the rat. *The Anatomical Record*, 203(3):397–404, 1982.

[14] B Davis, K Royalty, M Kowarschik, C Rohkohl, E Oberstar, B Aagaard-Kienitz, D Niemann, O Ozkan, C Strother, and C Mistretta. 4d digital subtraction angiography: implementation and demonstration of feasibility. *American Journal of Neuroradiology*, 34(10):1914–1921, 2013.

[15] Carl De Boor, Carl De Boor, Etats-Unis Mathématicien, Carl De Boor, and Carl De Boor. *A Practical Guide to Splines (Revised Edition)*, volume 27. Springer-Verlag New York, 1978.

[16] Prabal Deb, Suash Sharma, and KM Hassan. Pathophysiologic mechanisms of acute ischemic stroke: An overview with emphasis on therapeutic significance beyond thrombolysis. *Pathophysiology*, 17(3):197–218, 2010.

[17] Christian Elliott. How to Cut Your Stroke Risk by More Than 50%, November 2014.

[18] Danilo Franchi, Pasquale Gallo, Luca Marsili, and Giuseppe Placidi. A shape-based segmentation algorithm for x-ray digital subtraction angiography images. *Computer methods and programs in biomedicine*, 94(3):267–278, 2009.

[19] Elias A. Geraldo. *Merck Manual [database online].* Merck Sharp and Dohme Corp, February 2017.

[20] Nicholas P Gruszauskas, Karen Drukker, Maryellen L Giger, Charlene A Sennett, and Lorenzo L Pesce. Performance of breast ultrasound computer-aided diagnosis: dependence on image selection. *Academic radiology*, 15(10):1234–1245, 2008.

[21] Molly A Hatcher and Jessica A Starr. Role of tissue plasminogen activator in acute ischemic stroke. *Annals of Pharmacotherapy*, 45(3):364–371, 2011.

[22] Paul H Heintzen, Hans J Bürsch, Hans-Jürgen Hahne, Rüdiger Brennecke, Wilfried Budach, and Peter Lange. Assessment of Cardiovascular Function by Digital Angiocardiography. *Journal of the American College of Cardiology*, 5(1):150S–157S, 1985.

[23] C Heyn, J Poublanc, A Crawley, D Mandell, JS Han, M Tymianski, JA Fisher, DJ Mikulis, et al. Quantification of cerebrovascular reactivity by blood oxygen level–dependent mr imaging and correlation with conventional angiography in patients with moyamoya disease. *American Journal of Neuroradiology*, 31(5):862–867, 2010.

[24] Jack Jallo, Rainer Saetzler, Christopher Mishke, William F Young, Usha Vasthare, and Ronald F Tuma. A chronic model to simultaneously measure intracranial pressure, cerebral blood flow, and study the pial microvasculature. *Journal of neuroscience methods*, 75(2):155–160, 1997.

[25] Tudor G Jovin, Angel Chamorro, Erik Cobo, María A de Miquel, Carlos A Molina, Alex Rovira, Luis San Román, Joaquín Serena, Sonia Abilleira, Marc Ribó, et al. Thrombectomy within 8 hours after symptom onset in ischemic stroke. *New England Journal of Medicine*, 372(24):2296–2306, 2015.

[26] Chelsea S Kidwell, Reza Jahan, Jeffrey Gornbein, Jeffry R Alger, Val Nenov, Zahra Ajani, Lei Feng, Brett C Meyer, Scott Olson, Lee H Schwamm, et al. A trial of imaging selection and endovascular treatment for ischemic stroke. *New England Journal of Medicine*, 368(10):914–923, 2013.

[27] Masahiko Kumazawa, Hiroki Iida, Masayoshi Uchida, Mami Iida, Motoyasu Takenaka, Naokazu Fukuoka, Tomohiro Michino, and Shuji Dohi. The effects of transient cerebral ischemia on vasopressin-induced vasoconstriction in rabbit cerebral vessels. *Anesthesia & Analgesia*, 106(3):910–915, 2008.

[28] Maarten G Lansberg, Jun Lee, Soren Christensen, Matus Straka, Deidre A De Silva, Michael Mlynash, Bruce C Campbell, Roland Bammer, Jean-Marc Olivot, Patricia Desmond, et al. RAPID automated patient selection for reperfusion therapy. *Stroke*, 42(6):1608–1614, 2011.

[29] Maarten G Lansberg, Matus Straka, Stephanie Kemp, Michael Mlynash, Lawrence R Wechsler, Tudor G Jovin, Michael J Wilder, Helmi L Lutsep, Todd J Czartoski, Richard A Bernstein, et al. MRI profile and response to endovascular reperfusion after stroke (DEFUSE 2): a prospective cohort study. *The Lancet Neurology*, 11(10):860–867, 2012.

[30] Kenneth Levenberg. A method for the solution of certain non-linear problems in least squares. *Quarterly of applied mathematics*, 2(2):164–168, 1944.

[31] Donald Lloyd-Jones, Robert Adams, Mercedes Carnethon, Giovanni De Simone, T Bruce Ferguson, Katherine Flegal, Earl Ford, Karen Furie, Alan Go, Kurt Greenlund, et al. Heart disease and stroke statistics—2009 update. *Circulation*, 119(3):e21–e181, 2009.

[32] Donald W Marquardt. An algorithm for least-squares estimation of nonlinear parameters. *Journal of the society for Industrial and Applied Mathematics*, 11(2):431–441, 1963.

[33] Kenneth O McGraw and Seok P Wong. Forming Inferences About Some Intraclass Correlation Coefficients. *Psychological Methods*, 1(1):30, 1996.

[34] Richard McKinley, Levin Häni, Jan Gralla, Marwan El-Koussy, S Bauer, Marcel Arnold, Urs Fischer, Simon Jung, Kaspar Mattmann, Mauricio Reyes, et al. Fully automated stroke tissue estimation using random forest classifiers (FASTER). *Journal of Cerebral Blood Flow & Metabolism*, page 0271678X16674221, 2016.

[35] F McVerry, DS Liebeskind, and KW Muir. Systematic review of methods for assessing leptomeningeal collateral flow. *American Journal of Neuroradiology*, 33(3):576–582, 2012.

[36] Jessy J Mouannes-Srour. *Improving Quantitative Cerebral Perfusion MR Imaging based on the Bookend Technique*. PhD thesis, Northwestern University, 2012.

[37] Jessy J Mouannes-Srour, Wanyong Shin, Sameer A Ansari, Michael C Hurley, Parmede Vakil, Bernard R Bendok, John L Lee, Colin P Derdeyn, and Timothy J Carroll. Correction for arterial-tissue delay and dispersion in absolute quantitative cerebral perfusion dsc mr imaging. *Magnetic resonance in medicine*, 68(2):495–506, 2012.

[38] Leif Østergaard, Alma Gregory Sorensen, Kenneth K Kwong, Robert M Weisskoff, Carsten Gyldensted, and Bruce R Rosen. High resolution measurement of cerebral blood flow using intravascular tracer bolus passages. Part II: Experimental comparison and preliminary results. *Magnetic Resonance in Medicine*, 36(5):726–736, 1996.

[39] Leif Østergaard, Robert M Weisskoff, David A Chesler, Carsten Gyldensted, and Bruce R Rosen. High Resolution Measurement Of Cerebral Blood Flow Using Intravascular Tracer Bolus Passages. Part I: Mathematical Approach And Statistical Analysis. *Magnetic Resonance in Medicine*, 36(5):715–725, 1996.

[40] Lorenzo L Pesce and Charles E Metz. Reliable and computationally efficient maximum-likelihood estimation of "proper" binormal ROC curves. *Academic Radiology*, 14(7):814–829, 2007.

[41] Arne Potreck, Fatih Seker, Angelika Hoffmann, Johannes Pfaff, Simon Nagel, Martin Bendszus, Sabine Heiland, and Mirko Pham. A novel method to assess pial collateralization from stroke perfusion MRI: subdividing T_{max} into anatomical compartments. *European Radiology*, 27(2):618–626, 2017.

[42] Adnan I Qureshi. New grading system for angiographic evaluation of arterial occlusions and recanalization response to intra-arterial thrombolysis in acute ischemic stroke. *Neurosurgery*, 50(6):1405–1415, 2002.

[43] M Radaideh, C Devine, D Schomer, AJ Kumar, ED Cacayorin, J Song, S Lutzker, and N Leeds. Correlating the basic chronological pathophysiologic neuronal changes in response to ischemia with multisequence mri imaging. volume 2, page 1. American Society of Neuroradiology, 2003.

[44] Christian H Reinsch. Smoothing by spline functions. *Numerische mathematik*, 10(3):177–183, 1967.

[45] Nong Sang, Heng Li, Weixue Peng, and Tianxu Zhang. Knowledge-based adaptive thresholding segmentation of digital subtraction angiography images. *Image and Vision Computing*, 25(8):1263–1270, 2007.

[46] CM Strother, F Bender, Y Deuerling-Zheng, K Royalty, KA Pulfer, J Baumgart, M Zellerhoff, B Aagaard-Kienitz, DB Niemann, and ML Lindstrom. Parametric Color Coding of Digital Subtraction Angiography. *American Journal of Neuroradiology*, 31(5):919–924, 2010.

[47] C Zerna, Z Assis, CD d'Esterre, BK Menon, and M Goyal. Imaging, intervention, and workflow in acute ischemic stroke: the Calgary approach. *American Journal of Neuroradiology*, 37(6):978–984, 2016.

[48] Hua Zhang, Pranay Prabhakar, Robert Sealock, and James E Faber. Wide genetic variation in the native pial collateral circulation is a major determinant of variation in severity of stroke. *Journal of Cerebral Blood Flow & Metabolism*, 30(5):923–934, 2010.